The influence of superhydrophobic surfaces on near-wall turbulence

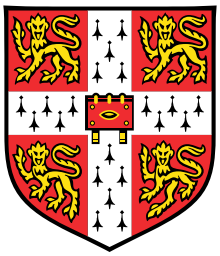

Christopher Terry Fairhall

Department of Engineering
University of Cambridge

This dissertation is submitted for the degree of
Doctor of Philosophy

Clare College September 2018

The hardest thing of all is to find a black cat in a dark room, especially if there is no cat

Unknown

Declaration

I hereby declare that except where specific reference is made to the work of others, the contents of this dissertation are original and have not been submitted in whole or in part for consideration for any other degree or qualification in this, or any other university. This dissertation is my own work and contains nothing which is the outcome of work done in collaboration with others, except as specified in the text and Acknowledgements. This dissertation contains fewer than 65,000 words including appendices, bibliography, footnotes, tables and equations and has fewer than 150 figures.

Christopher T. Fairhall
September 2018

Acknowledgements

I would like to thank my supervisor Dr. Ricardo García-Mayoral for providing me with this opportunity. His support and guidance throughout my time in Cambridge has helped me understand what makes a good researcher, and his knowledge and wisdom in the field has been invaluable. I would also like to thank everyone in the fluids office at Cambridge, past and present, for their fruitful discussions about work and beyond. There are too many people to list but you know who you are. A special mention, however, must go to Nabil, Akshath, Garazi and Joe. I must also thank my family for their continued and unreserved support and encouragement. Finally the financial support from the Engineering and Physical Sciences Research Council has been greatly appreciated.

Abstract

Superhydrophobic surfaces are able to entrap gas pockets in-between surface roughness elements when submerged in water. These entrapped gas pockets give these surfaces the potential to reduce drag due to the overlying flow being able to locally slip over the gas pockets, resulting in a mean slip at the surface. This thesis investigates the different effects that slip and the texturing of the surface have on turbulence over superhydrophobic surfaces. It is shown that, after filtering out the texture-induced flow, the background, overlying turbulence experiences the surface as a homogeneous slip boundary condition. For texture sizes, expressed in wall units, up to $L^+ \lesssim 20$ the only effect of the surface texture on the overlying flow is through this surface slip. The direct effect of slip does not modify the dynamics of the overlying turbulence, which remains canonical and smooth-wall-like. In these cases the flow is governed by the difference between two virtual origins, the virtual origin of the mean flow and the virtual origin experienced by the overlying turbulence. Streamwise slip deepens the virtual origin of the mean flow, while spanwise slip acts to deepen the virtual origin perceived by the overlying turbulence. The drag reduction is then proportional to the difference between the two virtual origins, reminiscent of drag reduction using riblets. The validity of slip-length models to represent textured superhydrophobic surfaces can resultantly be extended up to $L^+ \lesssim 20$. However, for $L^+ \gtrsim 25$ a non-linear interaction with the texture-coherent flow alters the dynamics of the background turbulence, with a reduction in coherence of large streamwise lengthscales. This non-linear interaction causes an increase in Reynolds stress up to $y^+ \lesssim 25$, and decreases the obtained drag reduction compared to that predicted from homogeneous slip-length models.

Nomenclature

Greek symbols

Symbol	Description
Δ	Spatial offset between velocity and shear
Δc_f	Change in skin-friction coefficient
Δt	Timestep
Δp	Pressure difference across the liquid-gas interface
ΔU	Shift of the logarithmic region of the mean velocity profile
Δx	Streamwise grid spacing
Δy	Wall-normal grid spacing
Δz	Spanwise grid spacing
α	Runge-Kutta coefficient of the implicit viscous term
β	Runge-Kutta coefficient of the explicit viscous term
γ	Runge-Kutta coefficient of the advective term
δ	Channel half-height
δ'	Effective channel half-height
ζ	Runge-Kutta coefficient of the advective term
η	Liquid-gas interface deformation height
θ	Contact angle
κ	Von Kármán's constant
λ	Wavelength
λ_j	Wall-normal interpolation coefficient
μ_0	Coefficient of proportionality between $\ell_x^+ - \ell_z^+$ and ΔU^+ for riblets
ν	Kinematic viscosity
ρ	Density
σ	Surface tension
τ_w	Wall shear stress
τ_{uv}	Reynolds stress
ϕ	Change in pressure
ϕ_g	Gas fraction
ϕ_s	Solid fraction
φ	Slip length phase

Roman symbols

Symbol	Description
A	Left-hand side of momentum equation in the fractional step method
B	Smooth-wall logarithmic intercept and wake function
CFL_a	Advective CFL number
CFL_v	Viscous CFL number
D	Discretised divergence operator
DR	Drag reduction
E_{uu}	Streamwise energy
G	Discretised gradient operator
I	Identity matrix
L	Discretised Laplacian operator
L_{xz}	Discretised Laplacian operator in streamwise and spanwise directions
L_y	Discretised Laplacian operator in the wall-normal direction
L	Texture size
N	Discretised non-linear operator
N	Number of grid points
$N_{TX,x}$	Number of grid points in the streamwise direction per texture element
$N_{TX,z}$	Number of grid points in the spanwise direction per texture element
N_x	Number of grid points in the streamwise direction
N_y	Number of grid points in the wall-normal direction
N_z	Number of grid points in the spanwise direction
Re	Bulk Reynolds number
Re_τ	Friction Reynolds number
Re_{tx}	Texture-element Reynolds number
U	Mean velocity
U_s	Slip velocity
a	Coefficient for the wall-normal grid stretching
b	Coefficient for the wall-normal grid stretching
c_f	Skin-friction coefficient
f	An arbitrary function
i	$\sqrt{-1}$
j	Wall-normal grid index
k	Wavenumber
k	Roughness height
k_{mod}	Modified wavenumber

k_x	Streamwise wavenumber
k_z	Spanwise wavenumber
m	An arbitrary integer
p	Kinematic pressure
$\boldsymbol{r}$	Right-hand side of momentum equation in the fractional step method
$\widetilde{\boldsymbol{r}}$	Right-hand side of momentum equation in the modified fractional step method
t	Time
$\boldsymbol{u}$	Velocity vector
$\boldsymbol{u}^*$	Fractional step intermediate velocity vector
u_τ	Friction velocity
u	Streamwise velocity
v	Wall-normal velocity
w	Spanwise velocity
x	Streamwise coordinate
y	Wall-normal coordinate
y_{int}	Wall-normal extent of the refined grid
z	Spanwise coordinate

Superscripts

Symbol	Description
$+$	Wall unit
$\prime$	Fluctuation
n	Timestep index

Subscripts

Symbol	Description
0	Quantity of the reference smooth-wall
δ	Quantity at channel centreline
bulk	Bulk-flow property
k	Runge-Kutta substep index
max	Maximum value
min	Minimum value
T	Turbulent component
SHS	Quantity from superhydrophobic simulations
SC	Quantity from smooth-channel simulations

Other symbols

Symbol	Description
ℓ_T	Virtual origin of the overlying turbulent flow
ℓ_x	Streamwise slip length / virtual origin of the mean flow
ℓ_z	Spanwise slip length
$\ell_{z,eff}$	Effective spanwise slip length
$\widehat{\ell_x}$	Dynamic streamwise slip length
$\widehat{\ell_z}$	Dynamic spanwise slip length
∇	Gradient operator
$\nabla\cdot$	Divergence operator
$\mathcal{O}$	Order of
$\widehat{f}$	Variable in Fourier space
$\overline{f}$	Mean quantity
$\widetilde{f}$	Texture-coherent component
$\widetilde{f}^*$	Directional texture-coherent component

Contents

List of Figures

List of Tables

Chapter 1

Introduction

This chapter introduces the motivation of and wider context around the application of superhydrophobic surfaces for drag reduction. The mechanisms of how these surfaces are able to reduce drag in turbulent flows are discussed and previous research in the area is summarised.

1.1 Background

Two of the driving motives for improvements in transportation are increasing speed and reducing greenhouse gas emissions. The transport sector alone accounted for 26% of the total greenhouse gas emissions within EU-28 countries in 2015 (European Environment Agency, 2017). The drag that a vehicle experiences is a limitation to both the speed and efficiency of the vehicle, as well as its range. One important contribution to the total drag is the skin friction, which results from friction between the fluid and the vehicle surface, and, on an aeroplane, accounts for approximately half of the total drag (Spalart & McLean, 2011). Numerous different techniques to reduce skin-friction drag in turbulent flows have been explored for several decades. These drag reduction techniques can be broadly split into two different categories, active methods and passive methods. Active methods require an energy input to achieve drag reduction, with some examples being oscillating walls (Jung *et al.*, 1992), surface suction/blowing (Choi *et al.*, 1994), or the addition of polymers into the flow (Virk, 1975). Passive forms of drag reduction require no additional energy to work, and typically take the form of surface modifications, for example, riblets (Walsh, 1983), which are streamwise aligned surface grooves, permeable media (Hahn *et al.*, 2002), or, in aquatic flows, superhydrophobic surfaces (Rothstein, 2010). In this thesis the drag reduction potential of the latter is explored.

1.2 Superhydrophobic surfaces

Research into engineering applications of superhydrophobic surfaces is inspired by examples found in nature. One of the classic naturally occurring examples of a superhydrophobic surface is the lotus leaf, which sometimes lends its name to the 'lotus leaf effect' to describe superhydrophobicty. This 'lotus leaf effect' can be illustrated by considering isolated droplets of water on a surface. On a conventional smooth surface, a droplet of water will typically spread out across the surface. The angle that the droplet makes with the surface, the contact angle, θ, for a conventional smooth surface is usually small, less than 90°, as shown in figure 1.1. On a rough surface, the droplet will typically fill the gaps in-between roughness elements. The surface roughness is wetted. This is known as the Wenzel state, and is depicted in figure 1.1. Superhydrophobic surfaces combine surface roughness with chemical hydrophobicity. This combination can allow droplets of water to sit on top of the roughness crests, with a cushion of gas in-between the roughness elements. This is known as the Cassie, or Cassie-Baxter, state and is also shown in figure 1.1. This property of superhydropho-

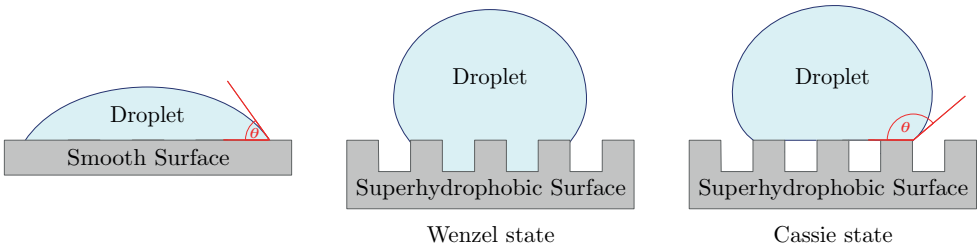

Figure 1.1 – Droplets of water on a smooth surface, a superhydrophobic surface in the Wenzel state and a superhydrophobic surface in the Cassie state.

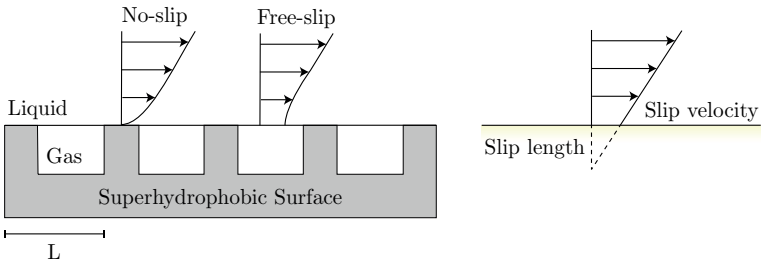

Figure 1.2 – Schematic of flow over a submerged superhydrophobic surface showing the regions of no slip and free slip over the roughness elements and entrapped gas pockets, respectively, and the mean slip length the surface produces.

bic surfaces has many useful applications for droplet flows. For example, droplets on superhydrophobic surfaces tend to roll off the surface rather than slide, as the centre of mass of the droplet is higher above the surface (Mahadevan & Pomeau, 1999). As a result, droplets are more effective at picking up dirt from the surface, which gives these surfaces good self-cleaning properties.

For superhydrophobic surfaces that are fully submerged in water, gas pockets can become entrapped in-between the roughness elements (Rothstein, 2010). An overlying flow is, therefore, free to slip over the entrapped gas pockets, as shown in figure 1.2. This local slip results in a mean slip velocity at the effective surface formed by the roughness crests and gas pockets. It is through this mean surface slip that superhydrophobic surfaces have the potential to reduce skin-friction drag.

1.3 Wall-bounded turbulence

Before the mechanisms that allow these surfaces to reduce drag in turbulent flows can be discussed, the physics of the near-wall region of wall-bounded turbulent flows need to be understood. Turbulent flows are often labelled as ‘chaotic’ or sometimes

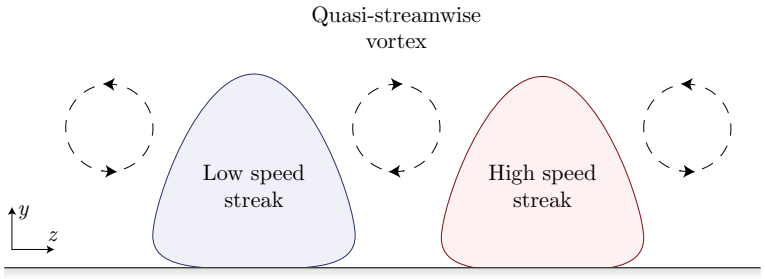

Figure 1.3 – Schematic of the near-wall cycle depicting the high and low speed streaks and their accompanying quasi-streamwise vortices.

'random'. While the former is undeniable, there is structure within the seeming randomness of near-wall turbulent flows. Indeed, the near-wall flow has been shown to be organised with the existence of coherent turbulent structures. Near-wall streaks were one of the first forms of organisation identified (Kline *et al.*, 1967). These streaks consist of spanwise alternating regions of high and low speed flow. The streaks are flanked by a series of quasi-streamwise vortices (Smith & Metzler, 1983) along their length. Together, these streaks and vortices form a self-sustaining process (Jiménez, 1994; Hamilton *et al.*, 1995), the 'near-wall cycle', depicted schematically in figure 1.3. The vortices generate the streaks by bringing higher momentum fluid towards the surface to form the high speed streaks and remove momentum from the wall to form low speed streaks. The vortices themselves are formed by an instability of the streaks (Jiménez & Pinelli, 1999). The near-wall cycle can exist independently of the presence of the outer flow (Jiménez & Pinelli, 1999), but is locally modulated by the outer region (Hutchins & Marusic, 2007).

In the near-wall region, the flow is characterised by its density, viscosity and the shear at the surface, $\tau_w = \rho\nu\partial U/\partial y|_w$, where ρ is the fluid density, ν is the fluid kinematic viscosity, and $\partial U/\partial y|_w$ is the wall-normal gradient of the mean velocity at the surface. From this, a characteristic velocity, the friction velocity $u_\tau = \sqrt{\tau_w/\rho}$ can be defined. Quantities characterised using the density, viscosity and friction velocity are known as 'wall units' or 'viscous units'. When expressed in these wall units many aspects of the near-wall dynamics are self-similar. For example, the near-wall streaks have a spanwise spacing of approximately $\lambda_z^+ \approx 100$ (Kim *et al.*, 1971) and a streamwise length of $\lambda_x^+ \approx 1000$ (Kreplin & Eckelmann, 1979). The quasi-streamwise vortices are separated in the spanwise direction by $\lambda_z^+ \approx 100$ and have a typical radius $\lambda_r^+ \approx 15$ (Blackwelder & Eckelmann, 1979). In the streamwise direction they remain in the near-wall region for in for approximately $\lambda_x^+ \approx 200$ with several vortices associated to a single streak (Jeong *et al.*, 1997).

Many of the aforementioned drag reduction techniques for turbulent flows in section 1.1 aim to achieve a reduction in drag by disrupting or modifying the near-wall cycle. This would reduce mixing that brings higher momentum flow towards the surface and, in turn, reduce the skin-friction drag. As discussed in the next section, superhydrophobic surfaces fall into this category.

1.4 Drag reduction through surface slip

In section 1.2, the concept that superhydrophobic surfaces are able to produce a surface slip was introduced. This slip velocity can also be characterised through the concept of a slip length. By considering the mean velocity at the surface, a slip length is introduced through a Navier slip condition (Navier, 1823), defined by

$$U_s = \ell_x \frac{\partial U}{\partial y}\Big|_s, \tag{1.1}$$

where the slip velocity, U_s, is the mean velocity at the surface, $\partial U/\partial y|_s$ is the wall-normal velocity gradient of the mean flow at the surface and ℓ_x is the mean slip length. This slip length defines the virtual origin experienced by the mean flow, i.e., it is the distance below the surface where the mean flow would experience a non-slipping wall. The concept of a slip length is equivalent of the protrusion heights introduced by Bechert & Bartenwerfer (1989) to quantify the drag reduction performance of riblets. For a given surface, the value of the slip length is dependent on the surface texture geometry and size. Analytical solutions for the slip lengths of idealised superhydrophobic surfaces have been derived for, among others, textures of streamwise and spanwise aligned ridges in the viscous Stokes regime (Philip, 1972; Lauga & Stone, 2003). Scaling laws have also been obtained for textures consisting of regular arrays of isolated posts (Ybert *et al.*, 2007) and randomly distributed free-slip patches (Sbragaglia & Prosperetti, 2007).

Using superhydrophobic surfaces in laminar flows, the obtained drag reduction depends only on the value of the slip length in the streamwise (x) direction, ℓ_x. Streamwise slip acts to shift the mean velocity profile by the slip velocity, as depicted in figure 1.4, which is a drag reducing effect. In turbulent flows, additional to the streamwise effect, the spanwise (z) slip length, ℓ_z, also influences the surface drag (Min & Kim, 2004). This is analogous to the drag reduction mechanism of riblets, where drag reduction was shown to be proportional to the difference between the streamwise and spanwise slip lengths (Luchini *et al.*, 1991; Luchini, 1996), or protrusion heights in riblet terminology. The effect of spanwise slip has been attributed to allowing quasi-

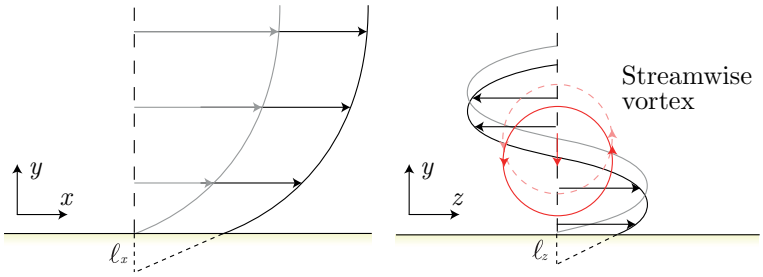

Figure 1.4 – Schematic showing the effect of streamwise and spanwise slip. Streamwise slip shifts the mean velocity profile, while spanwise slip allows quasi-streamwise vortices to move closer to the surface.

streamwise vortices to move closer to the surface (Min & Kim, 2004; Luchini, 2015), which is also depicted schematically in figure 1.4, and acts to increase drag.

For small surface manipulations in turbulent flows, the classical theory of wall turbulence states that the only influence of the surface on the outer flow is the location at which the outer flow perceives the wall. With drag reducing surfaces, the logarithmic region of the mean velocity profile is shifted upwards. Conversely, drag increasing surfaces cause a downward shift, with a shortening of the buffer layer (Min & Kim, 2004). The Kármán constant, κ, and wake function, however, remain unmodified (Clauser, 1956). It follows that the free-stream velocity, U_δ^+, of a surface with small-sized manipulations can be given by

$$U_\delta^+ = \sqrt{\frac{2}{c_f}} = \frac{1}{\kappa} \log \delta^+ + B + \Delta U^+, \tag{1.2}$$

where c_f is the skin friction coefficient, ΔU^+ is the velocity difference in the logarithmic region of the mean velocity profile compared to a smooth wall, δ^+ is the flow thickness, and B includes the smooth-wall logarithmic intercept and wake function. When considering a boundary layer, δ is the boundary layer thickness. For a channel δ is the channel half-height, with U_δ^+ the channel centreline velocity. The channel centreline is chosen rather than the bulk velocity to obtain a friction coefficient that closer resembles a boundary layer (García-Mayoral, 2011). From equation (1.2), a relation between ΔU^+ and the drag reduction can be obtained. Relative to a flow over a smooth wall at the same Re_τ, the resulting drag reduction is

$$DR = -\frac{\Delta c_f}{c_{f_0}} = 1 - \frac{1}{\left(1 + \Delta U^+ / U_{\delta_0}^+\right)^2}, \tag{1.3}$$

where c_{f_0} and $U_{\delta_0}^+$ are the skin friction coefficient and free-stream velocity for the

reference smooth wall, respectively. If Re_τ differs between the two surfaces, an additional logarithmic correction to equation (1.3) is required to account for the different $\delta^+ = \mathrm{Re}_\tau$ at which U_δ^+ is measured (Gatti & Quadrio, 2016), but this is the same difference that occurs between smooth walls at different Re_τ. It should be noted that while the drag reduction is related to ΔU^+, the drag reduction obtained for a given ΔU^+ is Reynolds-number dependent (Spalart & McLean, 2011). At higher Reynolds numbers, the obtained drag reduction is reduced due to the larger $U_{\delta_0}^+$.

For riblets of small size, it was shown that ΔU^+ varies linearly with the difference between the streamwise and spanwise slip lengths (Jiménez, 1994; Luchini, 1996). That is,

$$\Delta U^+ = \mu_0 \, (\ell_x^+ - \ell_z^+), \tag{1.4}$$

where μ_0 is a coefficient of order unity (Jiménez, 1994; Luchini, 1996; Bechert *et al.*, 1997). For superhydrophobic surfaces, this relationship for ΔU^+ holds when the spanwise slip length is small. However, as the spanwise slip length increases, its effect on ΔU^+ saturates (Fukagata *et al.*, 2006). A parametric study was carried out by Busse & Sandham (2012), which mapped the obtained drag reduction for a range of streamwise and spanwise slip lengths. It was suggested in Fairhall & García-Mayoral (2018) that their results can be interpreted as the spanwise effect being governed by an 'effective' spanwise slip length, $\ell_{z,eff}^+$, given by their parameter,

$$\ell_{z,eff}^+ = \frac{\ell_z^+}{1 + \ell_z^+/4}. \tag{1.5}$$

When the spanwise slip length is small, $\ell_z^+ \lesssim 1$, then $\ell_{z,eff}^+ \approx \ell_z^+$, recovering the linear relationship observed with riblets. For large values of spanwise slip, however, $\ell_{z,eff}^+$ tends to a value of 4. Due to this saturation of the spanwise effect, the shift of the logarithmic region is better represented by

$$\Delta U^+ \approx \ell_x^+ - \ell_{z,eff}^+, \tag{1.6}$$

where the coefficient μ_0 is equal to 1 (Luchini, 1996, 2015). As shown in Fairhall & García-Mayoral (2018), figure 1.5 confirms this relation by portraying results from Busse & Sandham (2012) in the form ΔU^+ vs. the parameter $\ell_x^+ - \ell_{z,eff}^+$, where the data is rescaled by the friction velocity for each case. The only discrepancy is for large values of streamwise slip at $\mathrm{Re}_{\tau_0} \approx 180$, where Re_{τ_0} is the friction Reynolds number of the smooth wall reference case. However, these simulations were conducted with a constant mass flow rate, and, at this low Reynolds number, relaminarisation was reported due to the large streamwise slip. Under laminar conditions, ℓ_z^+ no longer plays

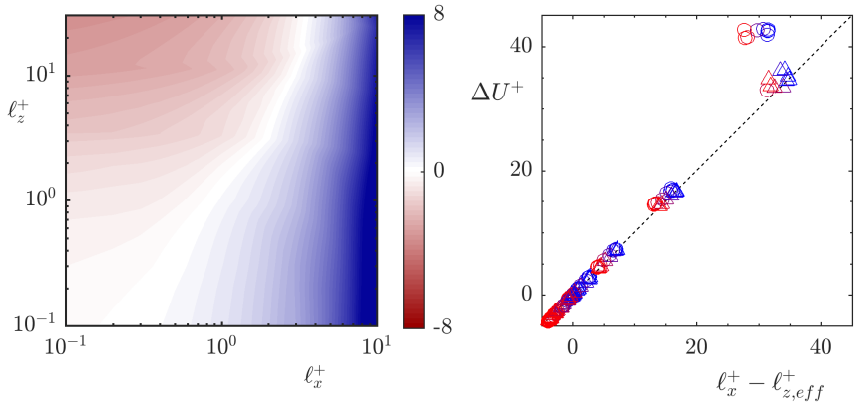

Figure 1.5 – Data taken from Busse & Sandham (2012) showing (left) the variation of ΔU^+ with streamwise and spanwise slip lengths and (right) the linear relationship between the difference of ℓ_x^+ and $\ell_{z,eff}^+$ with ΔU^+. ∘, $\mathrm{Re}_{\tau_0} \approx 180$; △, $\mathrm{Re}_{\tau_0} \approx 360$, coloured from blue to red for increasing spanwise slip. The data has been rescaled by the friction velocity of each individual case.

an adverse effect, which would explain the discrepancy in ΔU^+. Relaminarisation would not occur at larger Re_τ, and the results for $\mathrm{Re}_{\tau_0} \approx 360$ fall on the line $\Delta U^+ \approx \ell_x^+ - \ell_{z,eff}^+$.

Preliminary analysis in Gómez-de-Segura *et al.* (2018) suggests that the cause of the saturation effect of ℓ_z^+ results from the impermeability imposed at the surface in these slipping simulations, an effect not present with riblets. The imposed impermeability acts to limit the shift of quasi-streamwise vortices towards the surface. Therefore, to maximise drag reduction for any surface modification, the streamwise slip length should be maximised, and the spanwise slip length and the wall-normal permeability minimised. With real superhydrophobic surfaces, the liquid-gas interface of the gas pockets is able to deform in response to the overlying flow. This has the effect of relaxing the impermeability condition of the wall-normal velocity fluctuations. Seo *et al.* (2018) included coupling of the gas pocket deformation with the overlying turbulent flow in their numerical simulations. They found that, compared to simulations where the gas pockets were considered rigid, for texture sizes up to $L^+ \lesssim 30$, the mean velocity profile and turbulent fluctuations appear to remain essentially unmodified when the liquid-gas interface is free to deform, with the interface deformation small. The similarity between the mean velocity profiles and the velocity fluctuations of deformable and undeformable surfaces reported in their work suggests that the shift of turbulence closer to the surface, due to spanwise slip, is not further increased by this relaxation of the impermeability of wall-normal velocity fluctuations, at least for

texture sizes $L^+ \lesssim 30$.

While equation 1.6 allows a prediction of ΔU^+ to be obtained, it assumes that the slip lengths are known *a priori*. It was previously discussed that scaling laws for the slip lengths have been obtained in the viscous Stokes-flow limit (Philip, 1972; Lauga & Stone, 2003; Ybert *et al.*, 2007; Sbragaglia & Prosperetti, 2007). Using the slip lengths obtained in this limit assumes that in the near-wall region viscous effects dominate and advection is negligible. If the size of the texture is small, this is a reasonable assumption. In turbulent flows it has been shown that for small texture sizes, $L^+ \lesssim 10$, these viscous slip lengths are appropriate to model the surface (Seo & Mani, 2016). However, as the texture size increases, advection begins to become important. Consequently, the slip lengths deviate from these viscous predictions, with the measured slip length reduced compared to the viscous prediction. Seo & Mani (2016) attributed this deviation to the development of boundary layers over the roughness elements. They proposed a physical model, for sufficiently large texture sizes, $L^+ \sim 100$, where the slip length scales with the cube root of the texture size, that is,

$$\ell_x^+ \sim \frac{(L^+)^{1/3}}{\sqrt{\phi_s}}, \tag{1.7}$$

where ϕ_s is the solid fraction, which is the ratio of post area to total surface area.

The surface texture arrangement also affects the obtained slip lengths. Seo & Mani (2018) showed that in DNS simulations of surfaces with randomly distributed texture elements, the obtained slip length is reduced by approximately 30% compared to regularised textures. This is in agreement with Stokes-flow predictions in the small texture size limit (Sbragaglia & Prosperetti, 2007). They attributed this to the blockage effect of the randomly distributed texture. While regular textures have channels on the surfaces that allow the flow to pass undisturbed, with a random texture the flow will at some location be impeded by a texture element.

Modelling the effect of the surface through a slip length also typically assumes that the value of the slip length is constant. However, measurements of the slip length in experimental studies have shown that the value of the slip length is shear dependent (Churaev *et al.*, 1984). Choi *et al.* (2003) observed in their experiments a slip length that increases with the shear rate at the surface. The numerical simulations of Jung *et al.* (2016), who coupled the slip of the overlying flow with the lubricating fluid, also observed that the homogeneous slip length model is only valid in the averaged sense, with instantaneous variations in the local slip length observed. Khosh Aghdam & Ricco (2016) investigated the application of shear-dependent slip lengths in their

numerical simulations. They showed that while the near-wall turbulent fluctuations are modified by the shear-dependency of the slip length, surfaces with the same average slip length produced the same drag reduction.

The value of the slip length is also dependent on the static curvature of the gas pockets. A disparity between the pressure in the lubricating fluid and the overlying flow can cause the gas pockets to protrude into, or out of, the surface. Several studies investigating the effect of the gas pocket protrusion have shown that the maximum slip length is achieved for surfaces where the interface is close to being flat, with the slip length reduced by protrusion into or out of the surface (Steinberger *et al.*, 2007; Hyväluoma & Harting, 2008; Davis & Lauga, 2009; Teo & Khoo, 2010; Wang *et al.*, 2014). These studies also show that, for sufficiently large protrusion angles, the slip length becomes negative, making the surface drag increasing. However, in the turbulent simulations of Seo *et al.* (2018) the interface deformation they observed was small and did not appear to significantly affect the overlying turbulence. The slip length is also affected by constraints on the lubricating fluid (Busse *et al.*, 2013; Jung *et al.*, 2016). If the lubricating fluid is modelled as being free to enter and leave the domain with a non-zero mass flux, as, for example, would occur in a pressure-driven flow, then the slip length is larger than where the lubricating fluid is entrapped and forced to recirculate. Schönecker *et al.* (2014) showed that the value of the slip length is dependent on the depth of the gas pockets. If the gas pockets are too shallow, the slip length can be significantly reduced.

The inherent assumption to the discussions in this section has been that textured superhydrophobic surfaces can be modelled through the concept of slip lengths. The applicability of this assumption was assessed by Seo & Mani (2016). They compared the results from simulations where the texture geometry was resolved to ones where equivalent homogeneous slip lengths were applied, which were obtained *a posteriori* from their textured simulations. To assess the validity of the slip length model, they measured the instantaneous slip lengths over individual texture elements and compared these values to the measured slip length of the mean flow. They found that for small textures, in their case $L^+ \lesssim 10$, the instantaneous slip length experienced by individual texture elements was close to the measured slip length of the mean flow, with the mean velocity profiles of both simulations matching. For larger textures, however, the velocity and shear over individual texture elements appeared to lose correlation, resulting in large variations in the instantaneous value of the slip length. A large disagreement was also present between the obtained mean velocity profiles, and therefore ΔU^+, from the two surface representations when correlation was lost. They concluded that the applicability of slip-length models is limited to texture sizes smaller

than $L^+ \lesssim 10$. For larger texture sizes, ΔU^+ and the obtained drag reduction cannot be predicted from these slip-length models. The applicability of the slip length-model to represent textured surfaces will be further investigated in chapter 4 of this thesis.

1.5 The failure mechanism of superhydrophobic surfaces

Equation (1.6) showed that to maximise drag reduction the streamwise slip length should be maximised. Increasing the texture size is one way to increase the slip length (Philip, 1972; Ybert *et al.*, 2007). However, increasing the texture size eventually leads to the loss of the gas pockets from the surface. The surface then becomes a rough surface, potentially increasing the drag. One possible cause for the gas pockets being lost from the surface is due to pressure fluctuations deforming the gas pockets, which eventually overcome the surface tension keeping them entrapped. In addition to the pressure fluctuations from the overlying turbulence, Seo *et al.* (2015) reported texture-coherent pressure fluctuations caused by stagnation of the slipping flow at the texture elements. These pressure fluctuations increase with texture size and for sufficient texture size dominate the fluctuations due to the overlying turbulence. It was later reported in Seo & Mani (2018) that randomly distributed texture elements result in larger deformation compared to regularised textures. It should be noted, however, that perfectly aligned streamwise ridges produce no texture-coherent deformation as there is no stagnation effect, and therefore, no texture-coherent pressure distribution. Seo *et al.* (2018) later found that, for $L^+ \gtrsim 30$, an additional upstream-travelling capillary wave of the gas-liquid interface can develop for sufficiently large Weber numbers, which is a measure of the fluids inertia relative to the surface tension, whose onset significantly increases the pressure fluctuations. An alternative mechanism that can result in the loss of the gas pockets from the surface is the shear driven failure mechanism (Wexler *et al.*, 2015*b*) in which the lubricating fluid is depleted due to shear with the overlying flow. This failure mechanism is more prevalent with liquid infused surfaces, where a liquid is used as the lubricating fluid rather than air (Wong *et al.*, 2011; Lafuma & Quere, 2011). With these surfaces, there is a smaller disparity in viscosity between the lubricating fluid and the overlying fluid, and, consequently, a larger interfacial shear compared to superhydrophobic surfaces. The shear driven failure mechanism can, however, be countered by the addition of physical or chemical barriers along the surface to impede the lubricating fluid (Wexler *et al.*, 2015*a*).

1.6 Experimental studies of superhydrophobic surfaces

1.6.1 Laminar flows

Many of the early studies investigating superhydrophobic surfaces for drag reduction applications were experimental. Among the first to demonstrate the ability of superhydrophobic surfaces to reduce drag was Watanabe *et al.* (1999). They conducted experiments in a hydrophobic pipe with unstructured surface grooves that entrapped air pockets. They measured a reduction in wall friction in the laminar regime, which also persisted into the turbulent regime, measuring a shift of the velocity profile due to surface slip.

In the laminar regime, the focus of many early experimental studies of superhydrophobic surfaces was to design surfaces to maximise the surface slip. Several studies showed that drag reduction increases with increasing spacing between texture elements (Ou *et al.*, 2004; Ou & Rothstein, 2005; Lee *et al.*, 2008), or with increasing gas fraction (Lee *et al.*, 2008), which is the ratio of the area of the gas pockets to the total surface area. Structured surfaces of streamwise-aligned grooves were shown to be the most effective at reducing drag compared to textures of regular arrays of posts (Ou *et al.*, 2004), spanwise aligned ridges (Choi *et al.*, 2006) and unstructured surfaces (Choi & Kim, 2006; Cottin-Bizonne *et al.*, 2005; Balasubramanian *et al.*, 2004), in agreement with the predictions in the viscous regime (Philip, 1972; Lauga & Stone, 2003; Ybert *et al.*, 2007; Sbragaglia & Prosperetti, 2007).

Many authors also commented on the suitability of superhydrophobic surfaces for high fluid pressure applications (Truesdell *et al.*, 2006), with concerns over the stability of the liquid-gas interface. Choi *et al.* (2006) commented that smaller-sized textures were more applicable for higher liquid pressure applications as they can retain the gas pockets for larger interfacial pressures.

1.6.2 Turbulent flows

While the study of Watanabe *et al.* (1999) obtained drag reductions in both the laminar and turbulent regimes, other authors observed a loss of the drag reducing effect after the flow transitioned to turbulence (Henoch *et al.*, 2006; Zhao *et al.*, 2007), potentially a consequence of the gas pockets being lost from the surface. With a focus on drag reduction in the turbulent regime, Daniello *et al.* (2009) showed that, for their streamwise-aligned grooves, with $L^+ \lesssim 8$, increasing the texture size increased the drag reduction, as with the laminar regime. Similarly, increasing the gas fraction was also shown to increase drag reduction (Aljallis *et al.*, 2013; Park *et al.*, 2014).

Woolford *et al.* (2009) showed that with $L^+ \lesssim 2.4$, streamwise-aligned grooves were able to reduce drag, while spanwise aligned grooves increased drag.

Unstructured surfaces with a typical roughness height $k^+ \lesssim 5$ have also been shown to be capable of reducing drag in the turbulent regime (Gogte *et al.*, 2005; Park *et al.*, 2014; Bidkar *et al.*, 2014; Srinivasan *et al.*, 2015; Zhang *et al.*, 2015; Tian *et al.*, 2015; Ling *et al.*, 2016; Hokmabad & Ghaemi, 2016; Gose *et al.*, 2018). Random unstructured surfaces, generated, for example, by spray coatings, are perhaps more desirable for practical applications due to their easier manufacturing process (Bidkar *et al.*, 2014). However, Ling *et al.* (2016) showed that unstructured surfaces were less effective at reducing drag in the turbulent regime than streamwise aligned grooves, which is in agreement with the viscous slip length theory discussed in section 1.4, and has also been demonstrated in numerical simulations (Seo & Mani, 2018).

Several authors have commented on the retention of the gas pockets in the turbulent regime. Aljallis *et al.* (2013) observed that at high enough Reynolds numbers, the gas pockets were lost from the surface, with the roughness of the surface then increasing the drag. Degradation of the drag reduction performance, but not complete elimination, during experiments was observed by Balasubramanian *et al.* (2004). They reported that after drying the surface, the maximum drag reduction performance was regained, suggesting a partial loss of the gas pockets from the surface during their tests. Similarly, Govardhan *et al.* (2009) reported complete elimination of the drag reducing behaviour over long enough experimental runs. Rosenberg *et al.* (2016) investigated the drag reduction performance of both superhydrophobic surfaces and liquid-infused surfaces. The smaller viscosity disparity with liquid-infused surfaces, and therefore the larger interfacial shear, theoretically reduces their effectiveness at reducing drag compared to superhydrophobic surfaces. However, liquid-infused surfaces are less susceptible to pressure effects. The results of Rosenberg *et al.* (2016), who considered streamwise-aligned grooves with $L^+ \lesssim 8$, showed that one liquid-infused surface was more effective at reducing drag than a superhydrophobic surface. They theorised this as being due to loss of the gas pockets on the superhydrophobic surface. Some authors have also proposed that protrusion of roughness elements into the flow introduces additional drag and roughness-like effects (Bidkar *et al.*, 2014; Ling *et al.*, 2016; Gose *et al.*, 2018). Ling *et al.* (2016) investigated the effect of increasing the roughness protrusion, for the same texture, by increasing the overlying fluid pressure in their experiments. Their results showed an increase in drag with increasing fluid pressure. To counter the loss of the gas pockets, several methods have been proposed aiming to replenish them in application. Some methods proposed involve using air injection at a single location (Du *et al.*, 2017) or throughout a porous superhydrophobic surface

(Ling *et al.*, 2016), or, alternatively, using electrolysis (Lee & Kim, 2011).

1.7 Numerical simulations of superhydrophobic surfaces

Representing the full physics of a superhydrophobic surface is a complex problem in numerical simulations, requiring simplifications to be made to allow the problem to be tackled. In many early DNS studies, the surface was modelled using texture-averaged slip-length boundary conditions to predict the attainable drag reduction (Min & Kim, 2004; Busse & Sandham, 2012) or to investigate the effect of slip on transition (Min & Kim, 2005). Slip-length models are attractive in computational simulations because additional spatial resolution is not required to resolve the flow around the texture elements. Predicting the performance of surfaces using slip lengths assumes that the size of the surface texture is small compared to the scales in the overlying turbulent flow (Bechert & Bartenwerfer, 1989). In this theoretical 'vanishingly-small' limit, the overlying turbulent structures only experience the surface through the averaged effect of the texture, i.e., its slip lengths. They do not perceive individual texture elements. However, as the texture size becomes of the order of turbulent structures in the overlying flow, the assumption of vanishingly-small texture size becomes inappropriate (Seo & Mani, 2016). Consequently, the majority of recent simulations of superhydrophobic surfaces explicitly resolve the surface texture (Martell *et al.*, 2009; Park *et al.*, 2013; Jelly *et al.*, 2014; Türk *et al.*, 2014; Rastegari & Akhavan, 2015; Seo *et al.*, 2015).

Many of the texture-resolving simulations model the gas pockets as a free-slip boundary condition. The use of a free-slip boundary condition neglects all dynamics of the flow within the gas pockets. Davies *et al.* (2006) and Maynes *et al.* (2007) investigated the effect of coupling the lubricating fluid with the overlying flow in laminar simulations. They considered textures of streamwise-aligned grooves and showed that the obtained slip-length is over-predicted when the gas pockets are modelled as a free-slip interface, with a larger error for larger texture sizes. Schönecker *et al.* (2014) showed that while the free-slip condition over-predicts the slip length, it can give a reasonable prediction, provided that the gas pockets are sufficiently deep.

Martell *et al.* (2009) were among the first to represent the surface texture in their simulations. They modelled surface textures of regular arrays of isolated square posts and streamwise aligned ridges. The boundary conditions were applied using alternating regions of no slip and free slip, with the gas pockets considered flat and rigid. They observed that the turbulence over superhydrophobic surfaces is not fundamentally changed by the presence of the surface. Comparing different surface textures they showed that increasing the texture size produced a higher drag reduction. They

also showed that, for the same size, textures of posts were more effective at reducing drag than streamwise-aligned ridges due to the larger slip velocity they produce. Martell *et al.* (2010) later showed that their results were essentially independent of the friction Reynolds number, when scaled in wall units.

The simulations of Park *et al.* (2013) considered streamwise aligned grooves but only applied slip on the streamwise velocity, with no slip on the spanwise velocity. Their results show an increase in drag reduction with increasing gas fraction and show a collapse of drag reduction with the streamwise slip length, when scaled in wall units, across several Reynolds numbers. This supports equation (1.6) in the case where the spanwise slip length is zero.

Türk *et al.* (2014), Jelly *et al.* (2014) and Lee *et al.* (2015) investigating streamwise-aligned grooves, showed that secondary flows can develop for sufficiently large texture, due to the alternating free-slip and no-slip nature of the boundary conditions. These secondary flows increase the friction over the no-slip regions, which reduces the obtained drag reduction. Protrusion of the roughness elements in the flow has also been shown to increase the surface drag in numerical simulations, agreeing with experimental observations (Ling *et al.*, 2016). Busse *et al.* (2013) included this effect in their numerical simulations and showed that the drag-reducing effect of slip can be eliminated by additional drag resulting from the exposed roughness elements.

For textured surfaces, Türk *et al.* (2014), Jelly *et al.* (2014), Seo *et al.* (2015) and Rastegari & Akhavan (2015) observed that for texture sizes with $L^+ \gtrsim 25$, the velocity fluctuations show distinctly modified profiles compared to smooth wall profiles, suggesting a change in the turbulent dynamics occurring for sufficient texture size.

1.8 Scaling of turbulent channel flows

As introduced in section 1.3, many aspects of turbulence in the near-wall region are self-similar when scaled in their wall units, based on the fluid viscosity, density and friction velocity. However, if care is not taken when defining these variables, or how the problem is set-up, in particular when considering low Reynolds number flows, then different conclusions can arise.

For example, several studies in the literature conduct simulations using a constant mass flow rate, a choice that in principle does not affect the overlying turbulence compared to other methods (Quadrio *et al.*, 2016). In drag-reducing simulations, if the mass flow rate is chosen to be the same as a smooth-wall reference case, the driving pressure gradient is reduced. As a consequence, the wall shear stress, and, by definition, the friction velocity is also reduced, since, from a simple balance, $u_\tau =$

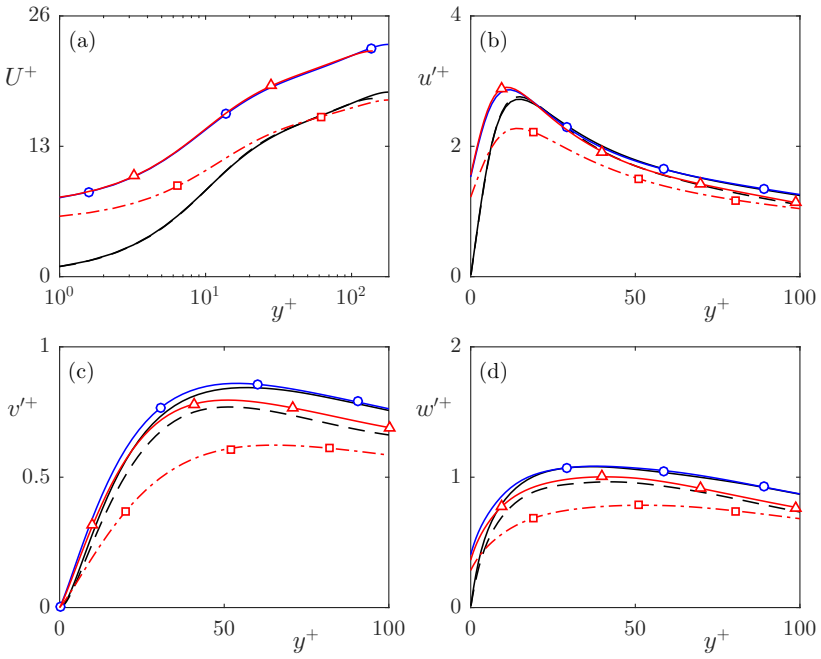

Figure 1.6 – The influence of normalisation of data on results. (a) mean velocity profiles; (b) streamwise rms velocity fluctuations; (c) wall-normal rms velocity fluctuations (d) spanwise rms velocity fluctuations. ——, smooth wall at $\mathrm{Re}_\tau \approx 180$; – –, smooth wall at $\mathrm{Re}_\tau \approx 140$; —○—, slipping channel with constant pressure gradient; –□-, slipping channel with constant flow rate scaled by u_{τ_0}; —△—, slipping channel with constant flow rate scaled by u_τ.

$\sqrt{-dp/dx\ \delta/\rho}$. However, several works in the literature considering drag-reducing cases choose to analyse their results by scaling by the friction velocity of the reference smooth wall, which is larger than the actual friction velocity of the case. This choice of normalisation can mask the underlying physics.

The importance of characterising the flow in the appropriate manner is highlighted in figure 1.6. This figure shows results from simulations taken from later in this thesis where a streamwise slip length of $\ell_x^+ = 6.9$ and a spanwise slip length of $\ell_z^+ = 4.3$ were applied. The simulations were run at a friction Reynolds number $Re_{\tau_0} \approx 180$ where a 0 subscript denotes scaling by the friction velocity of the smooth-wall reference case. One simulation was run with a constant pressure gradient, and hence constant Re_τ, and another with a constant mass flow rate, the same as the reference smooth wall, which results in a smaller Re_τ. The simulation run with a constant mass flow rate is shown normalised by the actual friction velocity, u_τ, and with the friction velocity of the smooth-wall reference case, u_{τ_0}. There are several things of note in this figure. Firstly, the results for the simulation run with a constant mass flow rate,

normalised by the smooth-wall friction velocity, u_{τ_0}, show an apparent damping of turbulence intensity, with a significant reduction in the peak magnitude of the rms fluctuations. The mean velocity profile also shows an apparent change in the Von Kármán constant, κ. Both of these effects, however, are solely a consequence of the normalisation, as the actual friction velocity is smaller than the smooth-wall friction velocity used. Normalising by the actual friction velocity shows a collapse to the mean velocity profile and streamwise velocity fluctuations of the constant pressure gradient simulation. Since the height above the surface, y^+, in wall units, depends on the friction velocity, the observed change in Kármán's constant, κ, is a direct consequence of the inappropriate u_τ. Due to the logarithmic nature of the axis, this results in an apparent stretching of the profile. Note that if the wrong origin for the mean velocity profile is chosen, then this can also appear to modify κ, as a linear shift of an inclined line on a logarithmic axis changes its gradient (García-Mayoral *et al.*, 2018), a subtlety that will be relevant later in this thesis.

While the streamwise fluctuations with a constant mass flow rate, normalised with the actual friction velocity, match the constant pressure gradient fluctuations, the wall-normal and spanwise velocity fluctuations are still reduced. This is due to the low Reynolds number of these simulations. The constant mass flow rate simulations started with $Re_{\tau_0} \approx 180$. However, imposing a constant mass flow compared to the smooth-wall reference case, the slipping simulation has dropped to $Re_\tau \approx 140$. At this lower Reynolds number, the fluctuations of a smooth wall exhibit lower peaks, and the fluctuations show a better agreement to the smooth wall profiles at $Re_\tau \approx 140$. Care must, therefore, be taken when analysing slipping simulations at low Reynolds numbers when running a constant mass flow rate, as modified turbulent dynamics due to the reduction in Reynolds number can be introduced.

The results of Min & Kim (2004) and Busse & Sandham (2012), which model the surface through homogeneous slip lengths, show both a shift of the peaks of the rms fluctuations and a change in their magnitudes. It is possible, however, that the latter may be explained by the scaling used. Both these simulations were run with a constant mass flow rate and present their results normalised by the friction velocity of the smooth wall reference case, u_{τ_0}. As the simulations produce either a drag reduction or a drag increase, the friction velocity for each individual case changes. While the turbulent fluctuations are reduced in intensity in 'outer' units, rescaling by the friction velocity of each individual case may show a closer agreement with the smooth channel fluctuations at that Reynolds number. Simulations in a channel with superhydrophobic boundary conditions applied to only one wall have also displayed a shift and weakening of turbulent fluctuations near the superhydrophobic

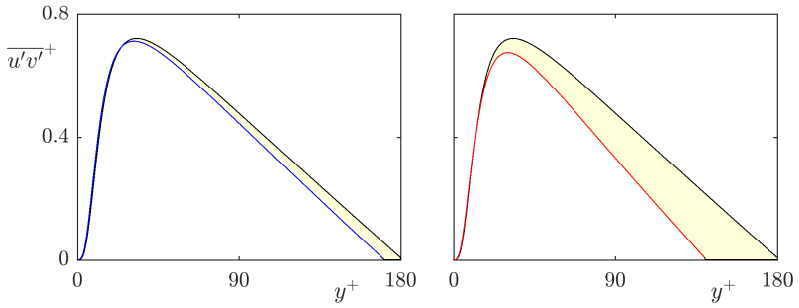

Figure 1.7 – The influence of Re_τ on the Reynolds stress, $\overline{u'v'}^+$, profile at low Reynolds numbers. ——, smooth wall at $\mathrm{Re}_\tau \approx 180$; ——, smooth wall at $\mathrm{Re}_\tau \approx 170$; ——, smooth wall at $\mathrm{Re}_\tau \approx 140$. The shaded areas show the difference in the Reynolds stress integral.

surface (Martell *et al.*, 2009). However, in this unsymmetrical set-up, there is no single clearly defined friction velocity to normalise the results by, being smaller at the superhydrophobic surface and larger at the smooth wall. This makes it difficult to assess what effects the superhydrophobic surface has on the overlying turbulence, particularly to physics further away from the surface. Several numerical studies (Min & Kim, 2004; Park *et al.*, 2013; Jelly *et al.*, 2014; Lee *et al.*, 2015) also observed that close to a superhydrophobic surface, near-wall vortices appear damped compared to those over a smooth wall. However, these studies analyse instantaneous vorticity not scaled using the actual wall units of the surface. While the vorticity may be reduced in 'outer units', studies where the friction velocity of the case is used for the scaling show that the vorticity appears similar to that over a smooth wall (Martell *et al.*, 2010; Türk *et al.*, 2014).

A change of friction Reynolds number, or equivalently the channel half-height δ^+, also affects the Reynolds stress, $\overline{u'v'}^+$, profile, as shown in figure 1.7, affecting the total Reynolds stress integral and ΔU^+ (Gatti & Quadrio, 2016). If the Reynolds stress integral is used to determine ΔU^+, as it will later in this thesis in chapter 6, if δ^+ differs between the two surfaces then a correction due to the Reynolds stress profiles crossing zero at their different respective δ^+ is required. If the friction Reynolds number is reduced too much, the peak Reynolds stress is also reduced, as also shown in figure 1.7. Chapter 5 of this thesis will show that the effect of slip also modifies the 'effective' channel height, δ'^+. To provide the fairest comparison between results in numerical simulations, simulations should be run at the same δ'^+.

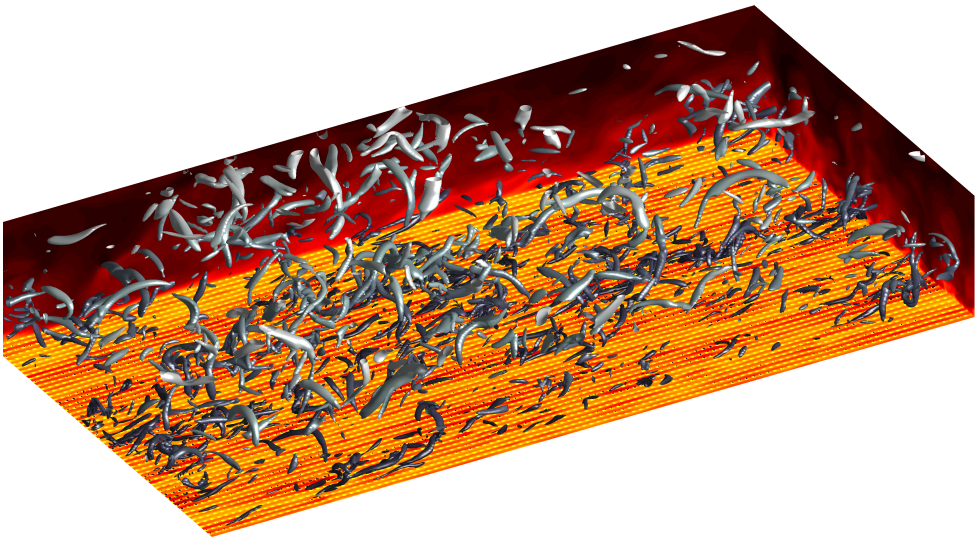

Figure 1.8 – Contours of streamwise velocity and realisations of vortical structures, represented using the Q-criterion, of turbulent flow over a superhydrophobic surface.

1.9 Thesis objectives and organisation

This thesis expands upon the existing literature investigating how superhydrophobic surfaces can reduce drag in turbulent flows. Direct numerical simulations (DNS), as for example shown in figure 1.8, across a range of texture sizes are conducted to analyse the influence the surface has on the overlying turbulence dynamics. The thesis is split into seven chapters. Chapter 1 summarises previous research into the use of superhydrophobic surfaces to reduce drag, discusses the drag reduction mechanism for such surfaces, and its equivalence to the drag reduction mechanism of riblet surfaces. Chapter 2 then details the numerical method that will be used in this thesis to simulate turbulent flows over superhydrophobic surfaces. Chapters 3–6 present the results of the thesis to answer the main objectives, which can be summarised as follows. Chapter 3 investigates how the value of the slip lengths and the susceptibility of the gas pockets to deformation are affected by the surface texture pattern and arrangement, and to what extent these can be predicted by viscous and laminar simulations. Next, the applicability of using slip-length models to represent textured superhydrophobic surfaces is reassessed in chapter 4. To discriminate between the slip-length experienced by the background turbulent flow and lengthscales of the order of the texture size a Fourier approach will be used. Chapter 5 will then investigate the effect that applying homogeneous slip-length boundary conditions has on the overlying turbulence, before the cause for the reduction in the measured value of ΔU^+ obtained from

texture-resolved simulations compared to that predicted from slip-length models is analysed in chapter 6. Finally, the findings from this thesis are summarised in Chapter 7 and an outlook on future work that would further add to the understanding of superhydrophobic surfaces in drag reducing applications is given.

Chapter 2

Numerical Method

This chapter outlines the numerical methods used in this thesis. To better understand the effects that superhydrophobic surfaces have on the overlying turbulent flow, a Direct Numerical Simulation (DNS) channel flow code is developed from the code of García-Mayoral (2011), which was originally designed to simulate turbulent flows over riblet surfaces. Validation of the numerical method is then presented and the simulations run in this thesis are outlined.

The flow within the channel is governed by the three-dimensional, incompressible Navier-Stokes equations,

$$\nabla \cdot \boldsymbol{u} = 0, \tag{2.1}$$

$$\frac{\partial \boldsymbol{u}}{\partial t} + \boldsymbol{u} \cdot \nabla \boldsymbol{u} = -\nabla p + \frac{1}{\mathrm{Re}} \nabla^2 \boldsymbol{u}, \tag{2.2}$$

where $\boldsymbol{u}$ is the velocity vector with components u, v, w in the streamwise, x, wall-normal, y, and spanwise, z, directions, respectively, p is the kinematic pressure, which is the pressure divided by the fluid density, and Re is the bulk Reynolds number, defined as

$$\mathrm{Re} = \frac{u_{\mathrm{bulk}} \delta}{\nu}, \tag{2.3}$$

with u_{bulk} the bulk velocity, δ the channel half-height and ν the fluid kinematic viscosity.

2.1 Time integration

The Navier-Stokes equations are advanced in time using a fractional step method (Kim & Moin, 1985). Fundamentally, this is a time-splitting method which involves first solving for an 'intermediate' velocity, for which continuity is not enforced, that is then corrected using the pressure.

Numerically, equations (2.1) and (2.2) can be discretised by way of simple example, for time-step n, as follows

$$\boldsymbol{u}^{n+1} - \frac{\Delta t}{2\ \mathrm{Re}} \mathrm{L}\boldsymbol{u}^{n+1} = \boldsymbol{u}^{n} - \Delta t \mathrm{G} p^{n+1} + \Delta t \left(-\mathrm{N}\boldsymbol{u}^{n} + \frac{1}{2\ \mathrm{Re}} \mathrm{L}\boldsymbol{u}^{n} \right), \tag{2.4}$$

$$\mathrm{D}\boldsymbol{u}^{n+1} = 0, \tag{2.5}$$

where D, L, G and N represent the discretised divergence, Laplacian, gradient and non-linear operators, respectively. In this example, the viscous term is solved using the semi-implicit Crank-Nicholson method, and the advective term is solved using an explicit Euler method. There are four equations to be solved for the next time-step, $n+1$, with four unknown variables, the velocity vector, $\boldsymbol{u}$, and the pressure, p. This set of discretised equations can be written as a system of equations (Perot, 1993) of the form

$$\begin{pmatrix} \mathrm{A} & \Delta t \mathrm{G} \\ \mathrm{D} & 0 \end{pmatrix} \begin{pmatrix} \boldsymbol{u}^{n+1} \\ p^{n+1} \end{pmatrix} = \begin{pmatrix} \boldsymbol{r} \\ 0 \end{pmatrix}, \tag{2.6}$$

where $\mathrm{A} = \left[\mathrm{I} - \frac{\Delta t}{2\mathrm{Re}}\mathrm{L}\right]$ forms the left-hand side when solving for the velocities and $\boldsymbol{r} = \boldsymbol{u}^n + \Delta t\left(-\mathrm{N}\boldsymbol{u}^n + \frac{1}{2\ \mathrm{Re}}\mathrm{L}\boldsymbol{u}^n\right)$ represents the explicit terms, and forms the right-hand side when solving for the velocities. The fractional step method can be thought of as taking an LU-decomposition of this system (Perot, 1993), resulting in the following set of equations

$$\begin{pmatrix} \mathrm{A} & 0 \\ \mathrm{D} & -\Delta t\mathrm{D}\mathrm{A}^{-1}\mathrm{G} \end{pmatrix} \begin{pmatrix} \boldsymbol{u}^* \\ p^{n+1} \end{pmatrix} = \begin{pmatrix} \boldsymbol{r} \\ 0 \end{pmatrix}, \tag{2.7}$$

$$\begin{pmatrix} \mathrm{I} & \Delta t\mathrm{A}^{-1}\mathrm{G} \\ 0 & \mathrm{I} \end{pmatrix} \begin{pmatrix} \boldsymbol{u}^{n+1} \\ p^{n+1} \end{pmatrix} = \begin{pmatrix} \boldsymbol{u}^* \\ p^{n+1} \end{pmatrix}, \tag{2.8}$$

where $\boldsymbol{u}^*$ are the intermediate velocities. These equations can be solved but are computationally expensive due to the requirement of the inverse of the A matrix at every iteration. To reduce computational cost a first-order approximation of A^{-1} is typically taken. As $\mathrm{A} = \mathrm{I} + \mathcal{O}(\Delta t)$, $\mathrm{A}^{-1} = \mathrm{I} + \mathcal{O}(\Delta t)$ is approximated as $\mathrm{A}^{-1} = \mathrm{I}$. Consequently, the error of the method here is first-order in time.

As discussed by Simens (2008), a modification to the method can, however, be made to achieve second-order accuracy in time for the velocities. This is achieved by solving for the change in pressure, ϕ, rather than directly for the pressure. By using $p^{n+1} = p^n + \phi^{n+1} + \mathcal{O}((\Delta t)^2)$, with $\phi^{n+1} \sim \mathcal{O}(\Delta t)$ and p^n known explicitly, equation (2.4) can accordingly be rewritten for ϕ as

$$\boldsymbol{u}^{n+1} - \frac{\Delta t}{2\ \mathrm{Re}}\mathrm{L}\boldsymbol{u}^{n+1} = \boldsymbol{u}^n - \Delta t\mathrm{G}p^n - \Delta t\mathrm{G}\phi^{n+1} + \Delta t\left(-\mathrm{N}\boldsymbol{u}^n + \frac{1}{2\ \mathrm{Re}}\mathrm{L}\boldsymbol{u}^n\right), \tag{2.9}$$

with equations (2.7–2.8) becoming

$$\begin{pmatrix} \mathrm{A} & 0 \\ \mathrm{D} & -\Delta t\mathrm{D}\mathrm{A}^{-1}\mathrm{G} \end{pmatrix} \begin{pmatrix} \boldsymbol{u}^* \\ \phi^{n+1} \end{pmatrix} = \begin{pmatrix} \widetilde{\boldsymbol{r}} \\ 0 \end{pmatrix}, \tag{2.10}$$

$$\begin{pmatrix} \mathrm{I} & \Delta t\mathrm{A}^{-1}\mathrm{G} \\ 0 & \mathrm{I} \end{pmatrix} \begin{pmatrix} \boldsymbol{u}^{n+1} \\ \phi^{n+1} \end{pmatrix} = \begin{pmatrix} \boldsymbol{u}^* \\ \phi^{n+1} \end{pmatrix}, \tag{2.11}$$

where $\widetilde{\boldsymbol{r}} = \boldsymbol{u}^n + \Delta t\left(-\mathrm{N}\boldsymbol{u}^n - \mathrm{G}p^n + \frac{1}{2\ \mathrm{Re}}\mathrm{L}\boldsymbol{u}^n\right)$. Again, A^{-1} can be approximated as I for efficiency, but since $\phi \sim \mathcal{O}(\Delta t)$ the overall error is now $\mathcal{O}((\Delta t)^2)$ for the three velocities. The pressure is first-order accurate, but is calculated at each time-step from the velocities, meaning that this error does not carry forward.

The code used in this thesis follows the above fractional step method combined with a three-step Runge-Kutta scheme, with the substep denoted by the subscript k.

Similar to the above example, a semi-implicit scheme is used for the viscous terms, with a two-step explicit scheme used for the advective terms. This leads to

$$\left[\mathrm{I}-\Delta t\frac{\beta_k}{\mathrm{Re}}\mathrm{L}\right]\boldsymbol{u}_k^n=\boldsymbol{u}_{k-1}^n+\Delta t\left[\frac{\alpha_k}{\mathrm{Re}}\mathrm{L}(\boldsymbol{u}_{k-1}^n)-\gamma_k\mathrm{N}(\boldsymbol{u}_{k-1}^n)\right.\\\left.-\zeta_k\mathrm{N}(\boldsymbol{u}_{k-2}^n)-(\alpha_k+\beta_k)\mathrm{G}(p_k^n)\right], \tag{2.12}$$

$$\mathrm{DG}(\phi_k^n)=\frac{1}{(\alpha_k+\beta_k)\Delta t}\mathrm{D}(\boldsymbol{u}_k^n), \tag{2.13}$$

$$\boldsymbol{u}_{k+1}^n=\boldsymbol{u}_k^n-(\alpha_k+\beta_k)\Delta t\mathrm{G}\phi_k^n, \tag{2.14}$$

$$p_{k+1}^n=p_k^n+\phi_k^n, \tag{2.15}$$

for $k=1,2,3$. The result of the third Runge-Kutta substep denotes the variables for the next $(n+1)$ time-step. The Runge-Kutta coefficients used, shown in table 2.1, are the same as Le & Moin (1991), which gives third-order accuracy for the advective terms and second-order accuracy for the viscous terms. The timestep is set with the advective CFL number $\mathrm{CFL_a}\leqslant 0.7$ and the viscous CFL number $\mathrm{CFL_v}\leqslant 2.5$, so that for the spatial discretisations outlined in section 2.2,

$$\Delta t=\min\left\{\mathrm{CFL_a}\left[\frac{\Delta x}{\pi|u|},\frac{\Delta y}{|v|},\frac{\Delta z}{\pi|w|}\right],\mathrm{Re}\ \mathrm{CFL_v}\left[\frac{\Delta x^2}{\pi^2},\frac{\Delta y_{min}^2}{4},\frac{\Delta z^2}{\pi^2}\right]\right\}. \tag{2.16}$$

$k=1$	$k=2$	$k=3$
$\zeta_1=0$	$\zeta_2=-17/60$	$\zeta_3=-5/12$
$\gamma_1=8/15$	$\gamma_2=5/12$	$\gamma_3=3/4$
$\alpha_1=\beta_1=4/15$	$\alpha_2=\beta_2=1/15$	$\alpha_3=\beta_3=1/6$

Table 2.1 – Runge-Kutta coefficients used in the numerical scheme from Le & Moin (1991).

2.2 Spatial Discretisation

The channel is periodic in the streamwise and spanwise directions with superhydrophobic boundary conditions applied to both channel walls. The streamwise and spanwise periodicity of the channel allows variables in these directions to be transformed via a

discrete Fast Fourier Transform (FFT) and solved in Fourier space. This has multiple benefits which will be detailed throughout this chapter. The wall-normal direction is discretised using second-order centred finite differences on a staggered grid.

For the DNS of a smooth channel, the constraint on the spatial resolution is that necessary to adequately capture the turbulent scales in the flow. For a turbulent channel, with a spectral discretisation, in the wall-parallel directions this corresponds to $\Delta x^+ \lesssim 8$ and $\Delta z^+ \lesssim 4$ (Jiménez & Moin, 1991). When considering small surface manipulations, such as a superhydrophobic surface, the requirement to satisfactorily capture the coherent flow around the texture elements creates an additional constraint on the grid resolution. The required resolution to capture the texture-induced flow can be several times finer than that required to capture the turbulent scales, but it is only required close to the surface, as the texture-induced flow decays exponentially away from the surface. For example, with riblets these finer scales extend between 1 to 2 times the riblet height above the riblets (García-Mayoral & Jiménez, 2011), whereas with roughness this can be as far as 5 times the roughness height above the roughness (Flack *et al.*, 2007). With the superhydrophobic surface considered here, the surface is flat, and the texture has no defined height. The texture induced flow, therefore, likely decays as a function of the texture spacing, similar to that observed for deep spanwise-aligned roughness (MacDonald *et al.*, 2018). Due to the decay of the texture-induced flow, a refined resolution is only needed close to the channel walls. If this additional resolution is applied throughout the channel, there is a large additional, but unnecessary, computational cost of over-resolving the rest of the channel. For this reason, the code was originally designed as a 'multiblock' code which allows a refined resolution near the surfaces, whilst maintaining typical DNS resolution in the channel centre (García-Mayoral & Jiménez, 2011). This multiblock takes the form of additional Fourier modes near the surfaces, to capture the texture-induced flow. The additional modes require a boundary condition at the interface between the fine and coarse regions. The signal in these additional modes decays away from the wall, and these additional modes are set to zero at the interface with the coarser, central block. It is verified *a posteriori* that the position of the interface is sufficiently distanced from the wall, so that these additional modes are not artificially damped, as discussed in section 2.5. Further details of the multiblock grid are given in García-Mayoral (2011).

The spectral discretisation in the wall-parallel directions means that derivatives in these directions have 'spectral resolution'. Discretisations using finite differences, by contrast, result in the introduction of truncation error. These errors can be seen by calculating the modified wavenumbers the schemes produce (Ferziger & Peric, 2002). For example, for a second-order central difference discretisation, approximating the

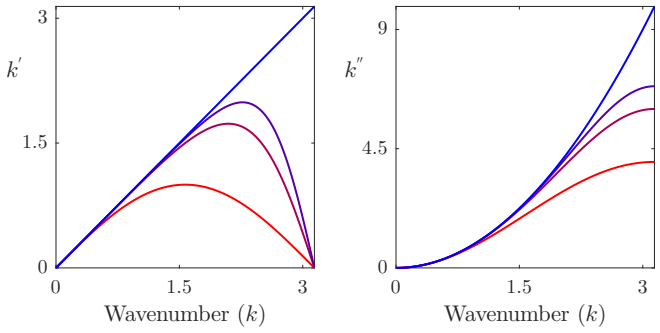

Figure 2.1 – Schematic showing the modified wavenumbers of several numerical discretisations. ——, spectral scheme; ——, 2nd order centred differences; ——, 4th order Pade scheme; ——, 6th order Pade scheme.

first derivative of the function $f = e^{ikx}$ gives

$$\frac{\mathrm{d}f}{\mathrm{d}x} = \frac{e^{ik(x+\Delta x)} - e^{ik(x-\Delta x)}}{2\Delta x} = i\frac{\sin(k\Delta x)}{\Delta x}e^{ikx} = ik_{\mathrm{mod}}f, \tag{2.17}$$

where $k_{\mathrm{mod}} = \frac{\sin(k\Delta x)}{\Delta x}$ is the modified wavenumber of this scheme. A similar analysis can be carried out for the second derivative, as well as for compact finite differences (Lele, 1992), to give the modified wavenumbers for a selection of schemes, as shown in figure 2.1. The difference to the exact wavenumber gives an indication of the error of the scheme, with higher order schemes matching the exact wavenumbers for a larger range of wavenumbers. Figure 2.1 shows that second-order finite differences only give good resolution up to the first $\sim 30\%$ of wavenumbers, damping the higher wavenumbers, which means a higher resolution is required to achieve adequate accuracy compared with higher-order schemes.

Solving the wall-parallel directions in Fourier space not only allows a 'spectral resolution' to be achieved in these directions, reducing the necessary grid resolution, but it also reduces the computational cost associated with solving the implicit parts of the code. This is due to derivatives in Fourier space being mode-independent, i.e., the derivative of $\widehat{f'}(k) = ik\widehat{f}(k)$ (where $\widehat{f}$ is the Fourier transform of f for wavenumber k) is only dependent on its value and wavenumber. This means that the derivative matrices in the spectral directions form purely diagonal matrices. It is only solving in the wall-normal direction that introduces off-diagonal elements from the coefficients of the numerical differentiation scheme. With a second-order finite difference discretisation, these are only on the first off-diagonals, which means that the system of equations can be reduced to a tridiagonal set of equations. These are considerably cheaper to solve than the very large, but sparse, matrices that are present in purely finite-difference codes and can be solved using the Thomas algorithm at a numerical cost of order N

(Thomas, 1949), where N is the number of grid points.

2.2.1 Wall-normal discretisation

To adequately represent the wall-normal gradients close to the wall, which requires a finer resolution than in the channel centre, a grid stretching is applied in this direction. The stretching takes the form of a fifth-order polynomial, the same as used in García-Mayoral (2011),

$$y(j) = a(j - \frac{N_y}{2}) + b(j - \frac{N_y}{2})^5, \tag{2.18}$$

with N_y the number of grid points in the wall-normal direction, j the grid index (from 1 to N_y) and a and b coefficients adjusted to give the desired grid resolution near the walls and in the channel centre. The grid resolution is set so that $\Delta y^+_{\text{min}} \simeq 0.3$ at the channel walls and $\Delta y^+_{\text{max}} \simeq 3$ in the channel centre.

In a discretised grid, it is usually convenient to store all variables, in this case, the three velocity components and pressure, at the same grid points. This is a so-called 'collocated' grid and is shown in figure 2.2(a). When using second-order centred finite differences this, however, causes problems when solving the pressure. This is due to the second derivatives at each point depending solely on the values of neighbouring points, separated by two grid points. There is, therefore, no direct communication between neighbouring points, which can lead to two disconnected pressure fields, with two solutions co-existing across alternating grid points. This is known as the 'checker-board' problem (Ferziger & Peric, 2002). There are several methods for avoiding this problem. In the original code of García-Mayoral (2011) this problem was alleviated by weakly enforcing incompressibility (Nordström *et al.*, 2007). However, this method can hamper the stability of the code. Therefore, the code was modified so that instead a staggered grid was used in the wall-normal direction, as shown in figure 2.2(b), which is a common solution to this problem (Ferziger & Peric, 2002). With a staggered grid, the velocity grid points are offset from the pressure grid points by half a grid spacing. This means that, when calculating gradient and divergence stencils for the pressure, the values of directly connected neighbouring grid points are used. Only the wall-normal velocity grid points are staggered with the streamwise and spanwise directions collocated as these are discretised spectrally.

The staggered grid is defined so that the wall-normal velocities are located on the surface. This means that the streamwise and spanwise velocities, as well as the pressure, are not defined at the surface. This choice necessitates the inclusion of additional 'ghost' points (see figure 2.2b) above/below the surface to be able to apply

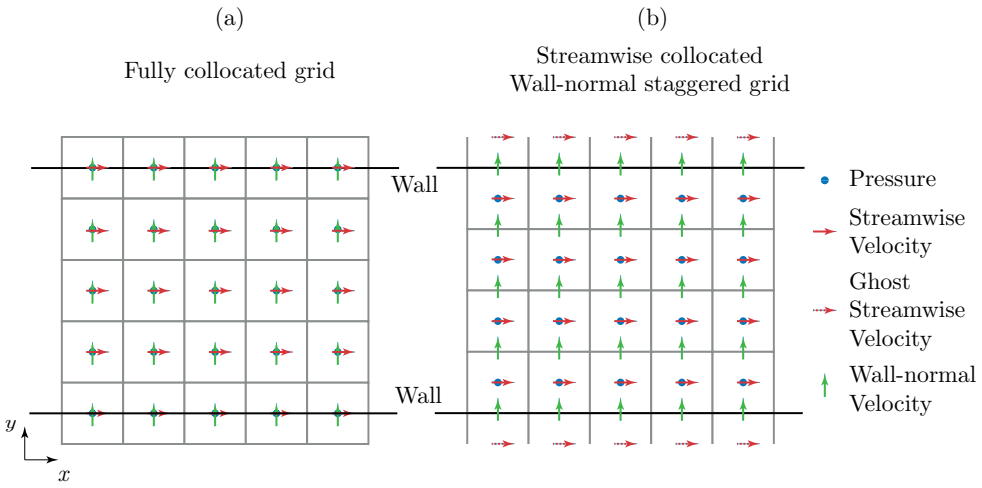

Figure 2.2 – Schematic of (a) fully collocated grid and (b) streamwise collocated, spanwise staggered grid showing the location of the 'ghost' points.

the desired surface boundary conditions on the streamwise and spanwise velocities. No physical boundary conditions need to be set on the pressure, but a numerical boundary condition is required to fix the pressure value of one point in the channel, due to only gradients of pressure being solved for in the governing equations, which leaves the actual value of the pressure free.

2.3 Treatment of non-linear terms

2.3.1 Calculation of the advective terms

A complication arises from solving in Fourier space when calculating the non-linear advective terms. These terms contain products of velocities which result in a convolution in Fourier space. Solving the convolution directly is numerically expensive to calculate (of order N^2). Instead, the velocities are transformed via an inverse fast Fourier transform, whose cost is of order $N \log_2 N$ (Cooley & Tukey, 1965), with the product computed in physical space, before transforming back to Fourier space. Doing this is computationally cheaper than solving the convolution in Fourier space.

Due to the use of a staggered grid, velocities are offset from each other and require interpolation between grids to calculate the advective products at the required grid points. For this, a linear interpolation is used, i.e.,

$$f_j = \lambda_j f_{j-\frac{1}{2}} + (1-\lambda_j) f_{j+\frac{1}{2}}, \tag{2.19}$$

where,

$$\lambda_j = \frac{y_{j+\frac{1}{2}} - y_j}{y_{j+\frac{1}{2}} - y_{j-\frac{1}{2}}}. \tag{2.20}$$

This can be shown to maintain second-order accuracy by taking the Taylor expansion of f_j and $f_{j+\frac{1}{2}}$ about $y_{j-\frac{1}{2}}$ and eliminating the first derivatives (Ferziger & Peric, 2002).

2.3.2 Dealising

When calculating the product of two variables, such as the advective term, in discrete Fourier space, a problem known as aliasing can arise. The convolution of two discrete functions, $\widehat{f}$, both of size N modes, as shown in figure 2.3(a), results in a function of size $2N$ discrete modes, figure 2.3(b). However, if the size of the function used to represent the convolution is of size N, then the additional modes cannot be correctly represented. This additional high frequency information is disguised in, and contaminates, the N modes of the function, as shown in figure 2.3(c). This contamination of the solution is known as aliasing. Aliasing occurs because the values for a mode k at discrete grid points are the same as the values for the mode $k + mN$, where N is the number of grid points and m is an integer. These modes are indistinguishable. This is depicted in figure 2.4, which shows that on a discretised grid with 4 grid points, with possible wavenumbers -2 to 1, the values at grid points for modes 1 and the unrealisable mode -3 are the same.

The convolution when solving the advective term adds additional modes that cannot be represented by the resolution. These would, therefore, contaminate the lower wavenumbers present. To avoid aliasing the '2/3' rule is used, where the function $\widehat{f}$ is padded with $N/2$ additional zero-valued modes (Canuto *et al.*, 2006), figure 2.3(d). This means that when the convolution, of size $3N$, is represented in size $3N/2$, interference only occurs in the additional N to $3N/2$ modes, figure 2.3(e). The additional modes are then subsequently dropped. With a smooth, well-resolved flow field, the values of modes N to $3N/2$ are small and they can be dropped without implications. However, near the superhydrophobic surface dropping these modes can be problematic if there is large texture-coherent flow. The discontinuous nature of the boundary conditions for superhydrophobic surfaces (as will be discussed in section 2.5) introduces high wavenumber information. If the texture-coherent flow is small then the convolution results in little information in these higher wavenumbers. However, if there is large texture-coherent flow then the modes dropped can have a non-negligible value. By removing these modes a Gibbs phenomenon can, therefore, be introduced.

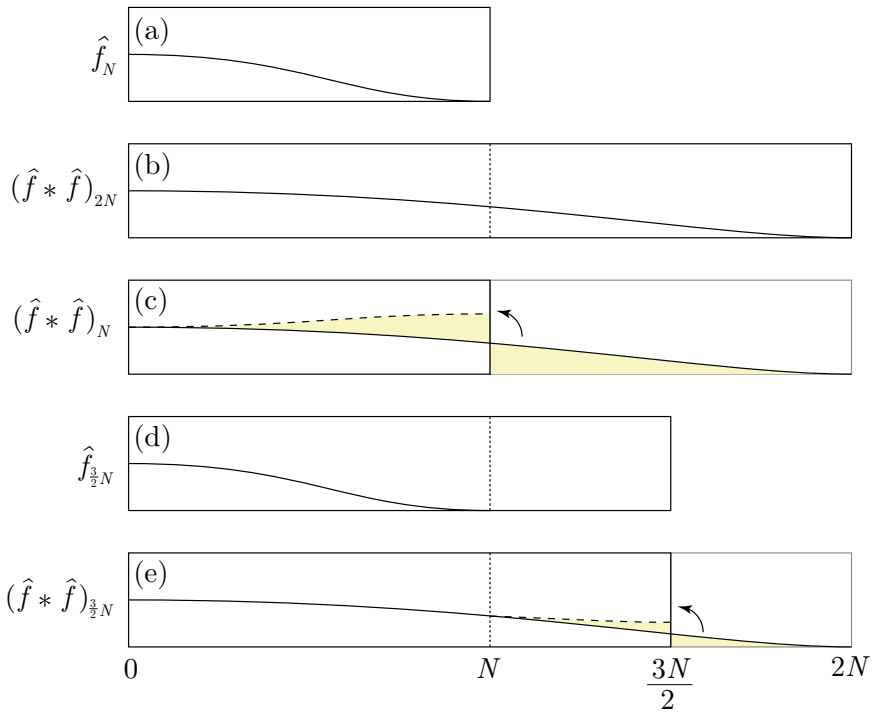

Figure 2.3 – Schematic showing the cause and method of avoiding aliasing. (a) A Fourier space function $\widehat{f}$ of size N; (b) The convolution $(\widehat{f} * \widehat{f})$ in size $2N$; (c) The convolution $(\widehat{f} * \widehat{f})$ in size N, including aliasing; (d) The function $\widehat{f}$ with padding; (e) The convolution of the padded $(\widehat{f} * \widehat{f})$ in size $3N/2$.

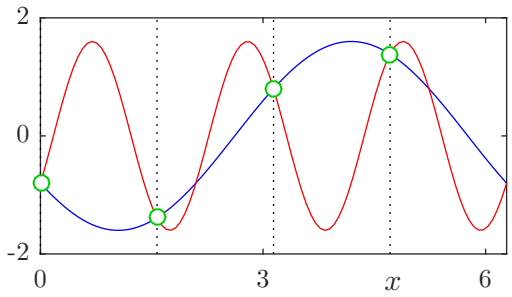

Figure 2.4 – Schematic showing the aliasing phenomenon where higher wavenumbers are disguised as lower wavenumbers. ——, mode 1; ——, unrealisable mode -3; ○, values at discretised grid points.

This Gibbs phenomenon is only present for large texture spacings, which have large texture-coherent flow. As the aim of this thesis is to focus predominantly on smaller sized textures, where this effect should be small when a sufficient grid resolution is used, this should not affect the results presented here.

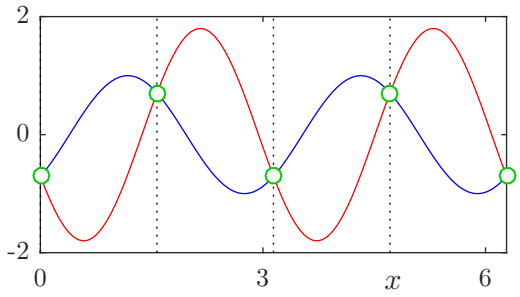

Figure 2.5 – Schematic showing the non-uniqueness of the highest wavenumber mode.

2.3.3 The domain in physical and Fourier space

Calculating the advective term in physical space requires the flow fields to be stored in both physical and Fourier space. A schematic showing how the data is stored, and how the Fourier transforms are taken, is shown in figure 2.6. In physical space, the grid consists of three 'blocks'. There are two refined blocks at the bottom and top of the channel and a coarser, centre block (figure 2.6a). Transforming from physical to Fourier space consists of taking Fourier transforms in the streamwise (figure 2.6b) and spanwise (figure 2.6c) directions. In Fourier space, each mode is described by two pieces of information, a magnitude and phase. This can be equivalently expressed using the complex Fourier coefficients of the mode.

Within the code, a Fourier transform is first taken in the streamwise direction of the purely real physical-space field. With N_x points in physical space, the transform results in N_x pieces of information (figure 2.6d): the 0^{th} mode (the mean), which, when expressed using the Fourier coefficients, has no imaginary part and therefore takes one piece of information. The coefficients of the paired modes 1 to $N_x/2-1$ and -1 to $-(N_x/2-1)$ are complex conjugates and so each take two pieces of information between them, leaving one final piece of information which is the real part of mode $N_x/2$. This mode cannot be fully resolved as its wavelength matches the wavelength of the grid. It is not possible to determine the magnitude and phase of the mode as there is no unique solution. For example, figure 2.5 shows two different solutions, with different phases and magnitudes, that give the same values at the discrete grid points for the last mode.

As there are more points in finer bands than the coarse band, these bands contain more modes. The Fourier transform, of a now complex field, is then taken in the spanwise direction. Again, information is conserved so that N_z physical space points gives N_z modes, from $-N_z/2$ to $N_z/2-1$, which are stored as depicted in figure 2.6(e). As with the streamwise discretisation, the mode $N_z/2$ is incomplete.

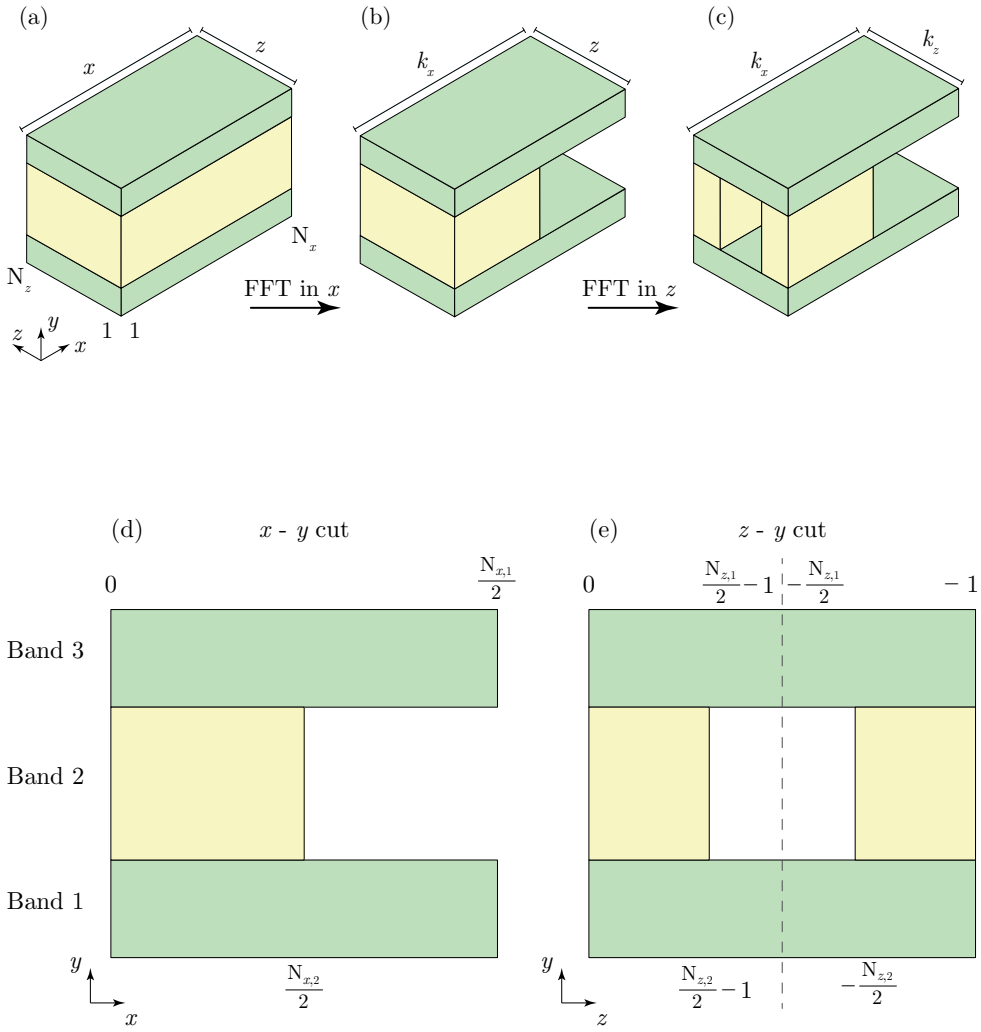

Figure 2.6 – Schematic showing how the data is stored in physical and Fourier space. (a) physical space representation, (b) data structure after the streamwise Fourier transform, (c) Fourier space representation, (d) x - y cut of the Fourier space representation, (e) z - y cut of the Fourier space representation. N denotes the number of grid points for the streamwise (subscript x) and spanwise (subscript z) directions. The subscript 1 denotes the resolution in the refined regions close to the surfaces and the subscript 2 the resolution in the central block.

2.4 Simulation setup

For all simulations, the channel is of size $2\pi\delta \times \pi\delta \times 2\delta$ in the streamwise, spanwise and wall-normal directions, respectively, where δ is the channel half-height. Most simulations in this thesis, unless otherwise stated, are carried out at a friction Reynolds number $\mathrm{Re}_{\tau_\delta} \approx 180$, where

$$\mathrm{Re}_{\tau_\delta} = \frac{u_\tau \delta}{\nu}. \tag{2.21}$$

This is a moderately low Re_τ and, consequently, there are weak low Reynolds number effects (Spalart, 1988; Moser *et al.*, 1999). It has been shown that for superhydrophobic surfaces, the underlying physics are, however, still essentially the same as at larger Reynolds numbers when scaled in wall units (Martell *et al.*, 2009; Busse & Sandham, 2012; Park *et al.*, 2013; Seo *et al.*, 2015). Nevertheless, the effect of increasing Re_τ will be investigated in section 2.7.

The flow is driven by a mean streamwise pressure gradient. Historically, there are several different methods of applying this pressure gradient. The two most prevalent options are either to vary the pressure gradient to ensure a constant mass flow rate through the channel, or to set the pressure gradient to be constant. The former fixes the bulk Reynolds number while the latter fixes the friction Reynolds number, leaving the other free. This choice generally does not have a significant effect on the simulation results (Quadrio *et al.*, 2016). In this thesis, it was chosen to maintain a constant Re_τ and therefore a constant pressure gradient was applied. Note, however, that a constant Re_τ could still have been achieved with a constant mass flow rate by adjusting the fluid viscosity.

2.5 Texture resolving simulations

The main set of simulations in this thesis resolve the surface texture geometry, which is modelled using alternating regions of free-slip and no-slip boundary conditions. The gas pockets are considered rigid, which results in an impermeability condition at the surface. As discussed in section 1.7, the use of a free-slip boundary condition neglects all dynamics of the flow within the gas pockets. While the slip length is over-predicted, Schönecker *et al.* (2014) showed that it can give a reasonable prediction provided that the gas pockets are sufficiently deep. Seo *et al.* (2018) showed that for texture sizes reported in experimental studies, $L^+ \lesssim \mathcal{O}(10)$ (Daniello *et al.*, 2009; Woolford *et al.*, 2009; Bidkar *et al.*, 2014; Rosenberg *et al.*, 2016; Ling *et al.*, 2016; Gose *et al.*, 2018), the interface deformation and the effect of the capillary wave they observed should be small. Their results also showed that for textures of this size, the turbulent velocity fluctuations appeared essentially unmodified by the inclusion of interface deformation.

The surface texture considered in the simulations consists of a regular array of square posts in a collocated arrangement, as shown in figure 2.7, with a solid fraction, ϕ_s, which is the ratio of post area to total surface area, of 1/9. The texture spacings considered range from $L^+ \approx 6$ to 47 and are outlined in table 2.2.

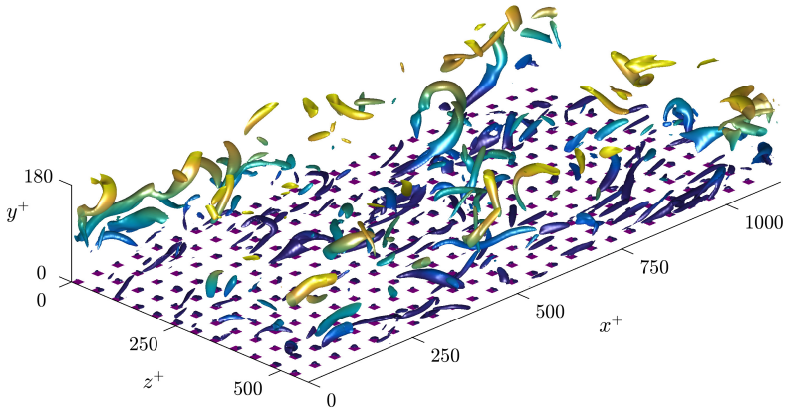

Figure 2.7 – Instantaneous realisation of vortical structures, represented using the Q-criterion, showing the surface texture for the case with $L^+ \approx 47$.

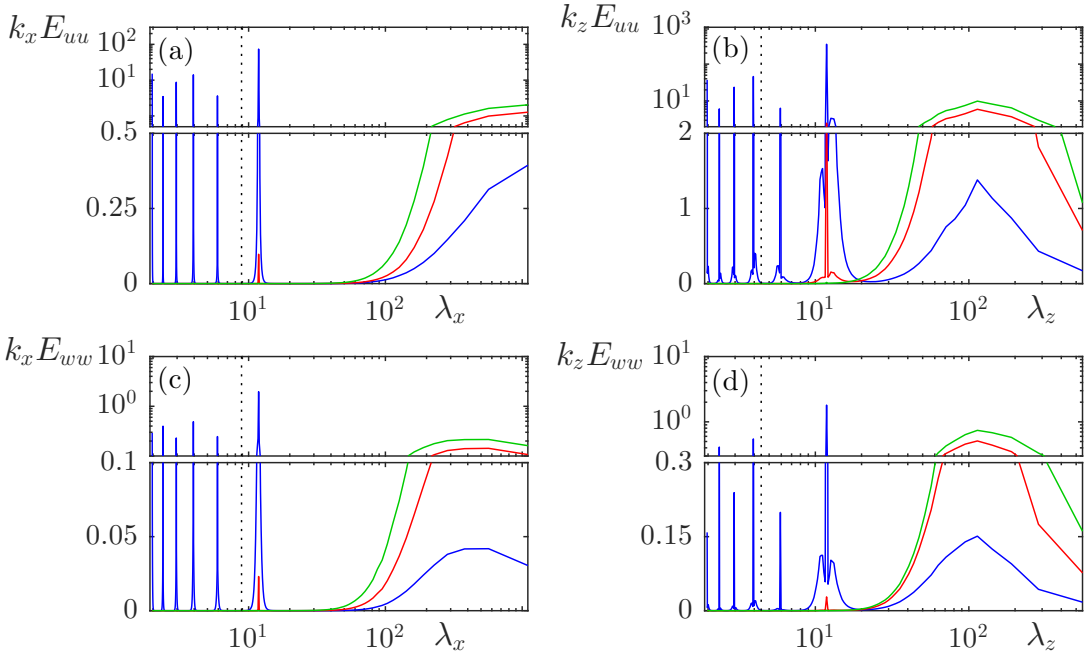

Figure 2.8 – One-dimensional energy spectra for the case with $L^+ \approx 12$ showing the decay of the texture-induced flow. ——, $y^+ = 0$; ——, $y^+ = 4$; ——, $y^+ = 8$. The dotted line denotes the cut-off between the central and refined blocks.

Case	L^+	$\mathrm{Re}_{\tau_\delta}$	$N_{x,w}$	$N_{z,w}$	N_y	$N_{TX,x}$	$N_{TX,z}$	y^+_{int}	$\widehat{\ell_x^+}$	$\widehat{\ell_z^+}$	ΔU^+
6	5.9	180	4608	2304	153	24	24	11.4	2.7	2.4	–
12	11.8	180	2304	1152	153	24	24	14.7	4.4	3.4	–
18	17.8	180	1576	768	153	24	24	22.2	5.8	3.9	3.5
24	23.7	180	1152	576	153	24	24	22.2	6.9	4.4	4.0
35	35.6	180	768	384	153	24	24	30.7	8.6	5.0	4.6
47	47.4	180	576	288	153	24	24	40.0	10.1	6.4	5.4
12c	11.8	180	1152	576	153	12	12	14.7	3.8	2.9	2.1
24c	23.7	180	576	288	153	12	12	22.2	6.0	3.8	3.5
24r	23.7	180	1728	864	153	36	36	22.2	7.2	4.5	4.2
24r2	23.7	180	2304	1152	153	48	48	22.2	7.4	4.6	–
24Re	23.6	405	2592	1296	335	24	24	21.0	6.7	4.3	4.4
35Re	35.4	405	1728	864	335	24	24	28.9	8.4	5.1	5.4

Table 2.2 – Parameters for the textured simulations. L^+ is the texture size in wall units with $\mathrm{Re}_{\tau_\delta}$ the friction Reynolds number. $N_{x,w}$ and $N_{z,w}$ are the number of grid points in the streamwise and spanwise directions in the refined blocks near the channel walls, with N_{TX_x} and N_{TX_z} the number of grid points per texture element, and N_y is the number of grid points in the wall-normal direction. y^+_{int} is the height of the refined block above the superhydrophobic surface. $\widehat{\ell_x^+}$ and $\widehat{\ell_z^+}$ are the measured dynamic slip lengths, and ΔU^+ is the measured shift of the logarithmic region of the mean velocity profile.

The height of the grid-refined multiblock interface is set so as to not artificially damp the texture-coherent flow. For the smaller textures this is set at a height at least one texture wavelength above the surface, where the resolution becomes that of a canonical smooth wall. One dimensional spectra of the streamwise and spanwise velocities for the case $L^+ \approx 12$ are shown in figure 2.8, at heights $y^+ = 0$, 4 and 8. They show that by $y^+ = 4$, a third of the texture spacing above the surface, the energy in the additional modes is negligible, and by a height $y^+ = 8$, the only energy visible is consistent with lengthscales of the overlying turbulence. This supports that the height of the multiblock interface is sufficiently distanced from the surface.

2.5.1 Implementation of the boundary conditions

The superhydrophobic boundary conditions are applied when solving the implicit part of the viscous term, that is

$$\left[\mathrm{I} - \Delta t \frac{\beta_k}{\mathrm{Re}} \mathrm{L}\right] \boldsymbol{u} = \mathrm{RHS}. \tag{2.22}$$

The left-hand side is tridiagonal so this matrix equation can be solved using a special form of Gaussian elimination, the Thomas algorithm (Thomas, 1949). The algorithm involves an LU decomposition followed by forward and backward substitutions. In the numerical code this is implemented by starting at the bottom wall of the channel and sweeping up to the top wall, before sweeping back down from the top to the bottom. In the upward sweep for each point in y, only the local point and the point below are required in the algorithm, and in the downward sweep the local point and the point above are required.

For a smooth walled channel, the implicit part of the viscous term can be solved entirely in Fourier space, with the boundary conditions at the walls of the channel and multiblock interfaces both applied in Fourier space, where each Fourier mode is set to zero. However, implementation of the superhydrophobic boundary conditions requires variables at the surface to be in physical space. While they could, in theory, be applied in Fourier space, this would require solving a convolution which would be computationally expensive. While the surface has physical-space boundary conditions, the boundary conditions at the multiblock interfaces still need to be applied in Fourier space, as here it is only the additional Fourier modes that have boundary conditions. The nature of the Thomas algorithm, however, allows solving of the implicit viscous term in both physical and Fourier space at different heights in the channel, by applying Fourier transforms during the algorithm. To allow this mixed Fourier/physical space solving, following Kim & Moin (1985), the streamwise and spanwise directions and the wall-normal direction of the implicit viscous term are split and solved separately,

$$\left[\mathrm{I} - \Delta t \frac{\beta_k}{\mathrm{Re}} \mathrm{L}\right] \boldsymbol{u} \approx \left[\mathrm{I} - \Delta t \frac{\beta_k}{\mathrm{Re}} \mathrm{L}_{xz}\right] \left[\mathrm{I} - \Delta t \frac{\beta_k}{\mathrm{Re}} \mathrm{L}_{y}\right] \boldsymbol{u}, \tag{2.23}$$

where L_{xz} includes the streamwise and spanwise components of the Laplacian, and L_y the wall-normal component. This maintains the second-order accuracy of the method (Kim & Moin, 1985). The streamwise and spanwise Laplacian is inverted first in Fourier space, which is a purely diagonal matrix, and forms part of the right-hand side when solving in the wall-normal direction. This can be written as,

$$\left[\mathrm{I} - \Delta t \frac{\beta_k}{\mathrm{Re}} \mathrm{L}_{y}\right] \boldsymbol{u} = \left[\mathrm{I} - \Delta t \frac{\beta_k}{\mathrm{Re}} \mathrm{L}_{xz}\right]^{-1} \mathrm{RHS}, \tag{2.24}$$

which is the tridiagonal set of equations to be solved. The left-hand side is now independent of the streamwise and spanwise directions, i.e., each point in x and

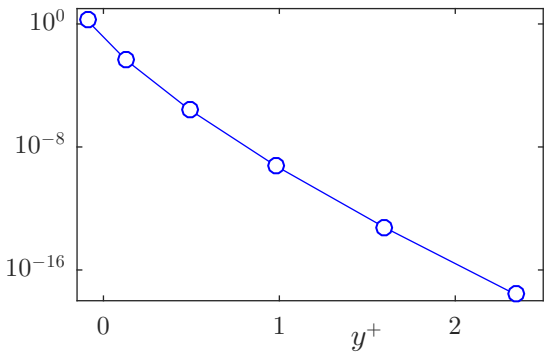

Figure 2.9 – Difference between the diagonal elements of the wall-normal Laplacian matrix between regions of no-slip and free-slip.

z is independent from other points. To apply the boundary conditions, the wall-parallel planes near the surface are transformed to physical space. Due to there being two boundary conditions, no-slip and free-slip, there are two different, but independent, $\left[I - \Delta t \frac{\beta_k}{\mathrm{Re}} \mathrm{L}_y\right]$ matrices. The difference between boundary conditions occurs only across the first two rows in the matrix, with the remainder of the matrix unchanged. However, after taking the LU decomposition, this difference gets smeared into the matrix. This smearing exponentially decays into the matrix and is dependent only on the y-grid, specifically the second derivative stencil. The two matrices, therefore, tend to the same operation sufficiently far from the surface. For the grid used here, the absolute difference between the diagonal elements of the two matrices is smaller than machine round-off error ($\sim 10^{-16}$) by the 6th point from the surface, as shown in figure 2.9, with a similar result for the off-diagonals. Above this point the operator is the same in physical or Fourier space. In the numerical code, the Fourier transform is, therefore, taken just above this point, after solving for it, so that the next point can be solved in Fourier space. This allows the boundary conditions at the surfaces to be applied in physical space, while the boundary conditions at the band interfaces are still applied in Fourier space.

This process is depicted schematically in figure 2.10. First the wall-parallel planes near the surfaces are transformed to physical space. The upward sweep is then solved up to the bottom FFT interface plane, number (1) in figure 2.10. This plane is then transformed to Fourier space so that the upward sweep can be solved up to the bottom band interface plane, number (2) in figure 2.10, where the Fourier boundary conditions are applied. The modes in the coarse block are then solved up to the top FFT interface plane, number (3) in figure 2.10. The boundary conditions at the top band interface plane are then applied in Fourier space so that the modes in the refined block can be

solved up to the top FFT interface, number (4) in figure 2.10. The top FFT interface plane is then transformed to physical space so that the upward sweep can be solved up to the top wall, number (5) in figure 2.10, with the boundary conditions applied in physical space. The process is then repeated on the downward sweep.

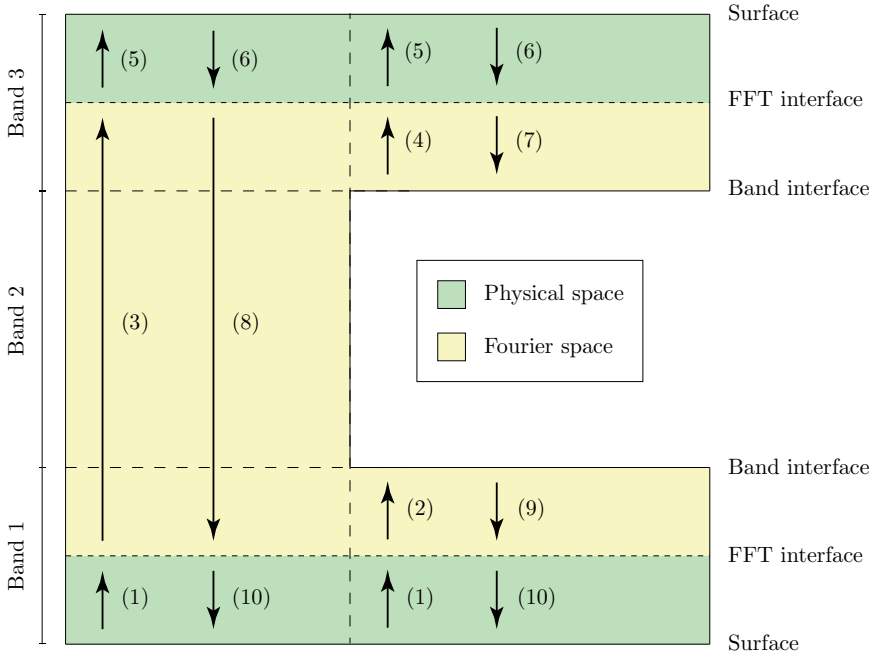

Figure 2.10 – Schematic showing how the wall-normal part of the implicit viscous term is solved using the Thomas algorithm. The arrows represent the direction of solving and the numbers the order of solving.

2.6 Validation

2.6.1 Validation of smooth channel

To verify that modifications made to the code had been implemented correctly, the code was first validated for a smooth channel. Figure 2.11 shows the mean velocity profile and turbulent velocity fluctuations for a smooth channel at $\mathrm{Re}_\tau \approx 180$ compared to the results of (Kim *et al.*, 1987). The simulation was run with a constant mass flow rate to match the original case, with the same domain size and grid resolution. The results show a very good level of agreement.

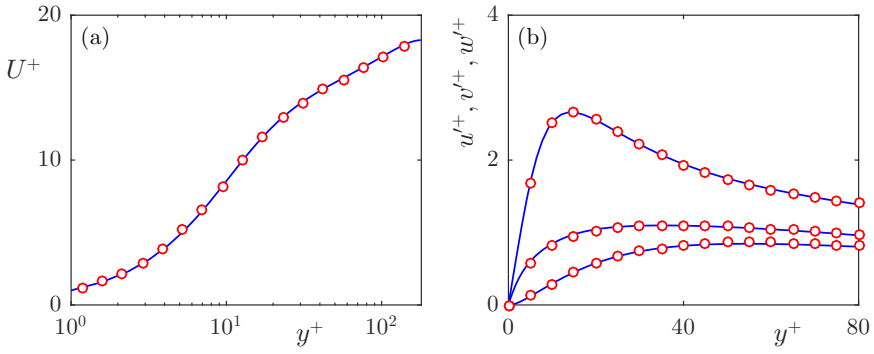

Figure 2.11 – Validation of the numerical method for a smooth channel. (a) mean velocity profile; (b) rms velocity fluctuations. ——, present numerical method; ○, smooth channel results of Kim *et al.* (1987).

2.6.2 Validation of the textured superhydrophobic boundary conditions

The implementation of the textured superhydrophobic boundary conditions was validated against the case with $L^+ \approx 39$ from Seo *et al.* (2015), as shown in figure 2.12. A good agreement can be seen between the turbulent velocity fluctuations. However, the value of the mean slip length and the downward shift of the mean velocity profile, shown in figure 2.12(a), show slight disagreement. Further analysis varying the number of grid points used to represent texture elements showed that the value of the slip lengths is dependent on the grid resolution. To assess this grid dependency on the simulations in this thesis, the case with $L^+ \approx 24$ was run with 12, 24, 36 and 48 points per texture element. Turbulent statistics for the simulation with 48 grid points per texture are not shown as, due to the cost of these simulations, they were not run long enough to achieve statistical convergence for the overlying turbulence. However, the texture-coherent statistics have a much shorter time-scale, so they could be obtained at a more moderate cost. The turbulent statistics for the resolutions with 12, 24 and 36 points per texture element are shown in figure 2.13, show a good agreement, suggesting that the overlying turbulence is not affected by this grid resolution. This is further supported by the respective premultiplied energy spectra, shown in figure 2.14, which indicate negligible change to the distribution of turbulent energy with varying grid resolution. Additionally, the rms of the ensemble-averaged texture-coherent flow with 12 points per texture element is within 4% of the value with 48 points per texture element, as shown in figure 2.13(c), suggesting only a weak influence of the resolution on the texture-induced flow.

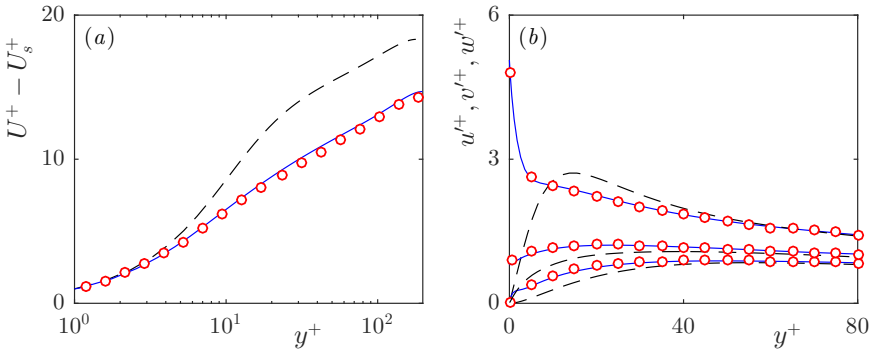

Figure 2.12 – Validation of the implementation of the slip/no-slip boundary conditions vs. the case with $L^+ \approx 39$ from Seo *et al.* (2015). (a) mean velocity profiles, with slip velocity (U_s) subtracted; (b) rms velocity fluctuations. – –, smooth wall; ——, present results; ○, results from Seo *et al.* (2015).

2.6.3 Grid dependency of the slip lengths

To further investigate the grid dependency of the value of the slip lengths, viscous Stokes-flow simulations for varying grid resolutions were conducted. The Stokes flow code uses the same fractional step scheme as the DNS code, but with no Runge-Kutta scheme and the viscous term is solved using a fully implicit method, i.e.,

$$\left[\mathrm{I} - \frac{\Delta t}{\mathrm{Re}}\mathrm{L}\right] \boldsymbol{u}^* = \boldsymbol{u}^n + \Delta t \mathrm{G}(p^n), \tag{2.25}$$

$$\mathrm{DG}(\phi^n) = \frac{1}{\Delta t}\mathrm{D}(\boldsymbol{u}^*), \tag{2.26}$$

$$\boldsymbol{u}^{n+1} = \boldsymbol{u}^* - \Delta t \mathrm{G}\phi^n, \tag{2.27}$$

$$p^{n+1} = p^n + \phi^n. \tag{2.28}$$

In the simulations, a single texture element is represented with the domain size $L \times L \times 4L$ in the streamwise, spanwise and wall-normal directions. The flow is driven by a homogeneous shear at the top of the domain. Simulations are conducted varying the number of grid points with two different wall-parallel spatial discretisations, a collocated, spectral discretisation and a staggered, finite difference discretisation. The percentage differences in measured slip lengths for the two schemes, compared to the result of the staggered finite difference discretisation with 72 points, is shown in figure 2.15. Both discretisations converge to the same value of the slip length with increasing grid resolution. The spectral discretisation, however, converges at a slower rate. For

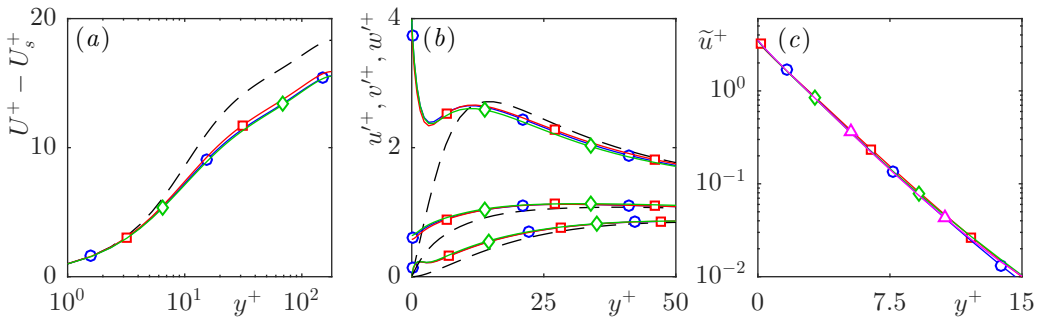

Figure 2.13 – Difference between (a) mean velocity profiles, with the slip velocity (U_s) subtracted; (b) rms velocity fluctuations; (c) wall-normal decay of streamwise coherent flow for the DNS grid resolution dependency test with $L^+ \approx 24$. – –, Smooth wall; –□–, 12 points per texture; –○–, 24 points per texture; –◇–, 36 points per texture; –△–, 48 points per texture.

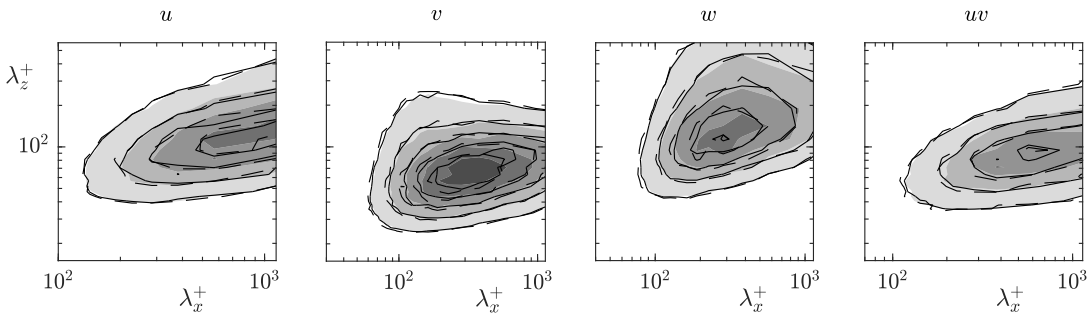

Figure 2.14 – Comparison of the spectral energy densities with increasing grid resolution for the three velocity components and Reynolds stress, $\overline{u'v'}^+$, at a height $y^+ = 15$ with $L^+ \approx 24$. Filled contour, 12 points per texture; ——, 24 points per texture; – –, 36 points per texture.

the spectral discretisation using 24 grid points per texture element, the difference of the obtained slip length is 14%. Using 12 points per texture, the difference is 27%. The error from DNSs with the same resolutions is portrayed superimposed in the figure, by assuming that the error for 48 points per texture is the same to set a common scale. The similar trend between the Stokes flow and DNS convergence implies that the grid-resolution error of the slip lengths in the DNSs are consistent with those of the Stokes-flow simulations. This suggests that the slip lengths obtained from DNS can be corrected by the Stokes-flow error to offset this resolution dependency.

The obtained streamwise slip lengths from the DNSs, together with the Stokes-flow slip lengths in the viscous limit, $L^+ \lesssim 1$, and results from Seo & Mani (2016) are shown in figure 2.16. By assuming that the discretisation error of the DNSs is

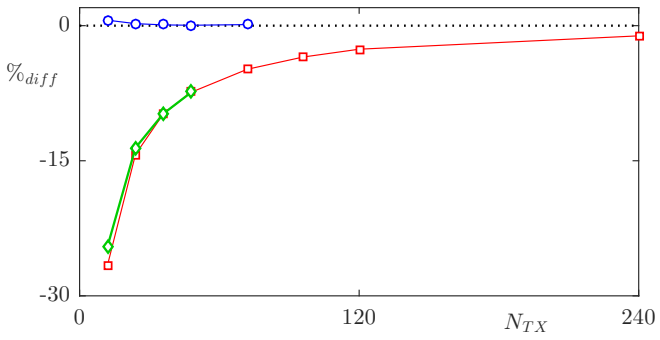

Figure 2.15 – Percentage difference between the measured slip lengths for viscous Stokes-flow simulations with varying number of streamwise/spanwise grid points per texture element (N_{TX}), to the slip length obtained from a finite difference discretisation with 72 grid points per texture element. –○–, Finite difference discretisation; –□–, spectral discretisation; –◇–, percentage difference of the slip lengths from the DNSs assuming that the error with 48 grid points per texture element matches the Stokes-flow error.

the same as the discretisation error of the viscous Stokes-flow simulations with the same spectral discretisation, estimates of the grid-converged DNS slip lengths are obtained. For different grid resolutions, the estimated grid-converged slip lengths for the same texture size have similar values and are close to the obtained slip lengths of Seo & Mani (2016). This further indicates that the discretisation error of the DNSs is consistent with the discretisation error of the Stokes-flow simulations. Due to this grid-resolution dependency, and to allow a fair comparison of the slip-length statistics between texture sizes, while turbulent statistics for the case with $L^+ \approx 12$ are obtained with 12 points per texture element, this simulation was further run with 24 points per texture element to obtain the texture-coherent statistics. All statistics presented for the slip lengths in the results and subsequent analysis are obtained from the simulation with 24 points per texture. To obtain the texture-coherent slip lengths and statistics for $L^+ \approx 6$, an additional simulation was conducted using the obtained slip length from laminar simulations as initial conditions.

This grid-resolution dependency of the spectral code means that the slip lengths in this work are slightly under-predicted compared to previous work in the literature where finite-difference discretisations were used. However, the actual values of the slip lengths are not the focus of the present work, and the turbulent statistics, on the other hand, appear to agree well.

It is possible that this grid-resolution dependency results from the different way that texture elements are represented between the two discretisations. The spectral

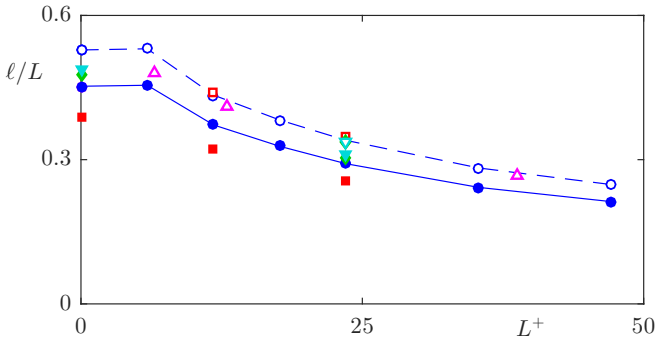

Figure 2.16 – Variation of the streamwise slip length measured from the DNSs with the texture size, and the corrected slip lengths taking into account the grid resolution dependency. ■, 12 points per texture; —●—, 24 points per texture; ♦, 36 points per texture; ▼, 48 points per texture. The results at $L^+ = 0$ are obtained from the viscous Stokes-flow simulations. The solid symbols represent the actual slip lengths obtained from the simulations. The hollow symbols show the estimated grid-converged slip lengths obtained by assuming that the discretisation error is the same in the Stokes-flow simulations and the DNSs. △, results from Seo & Mani (2016).

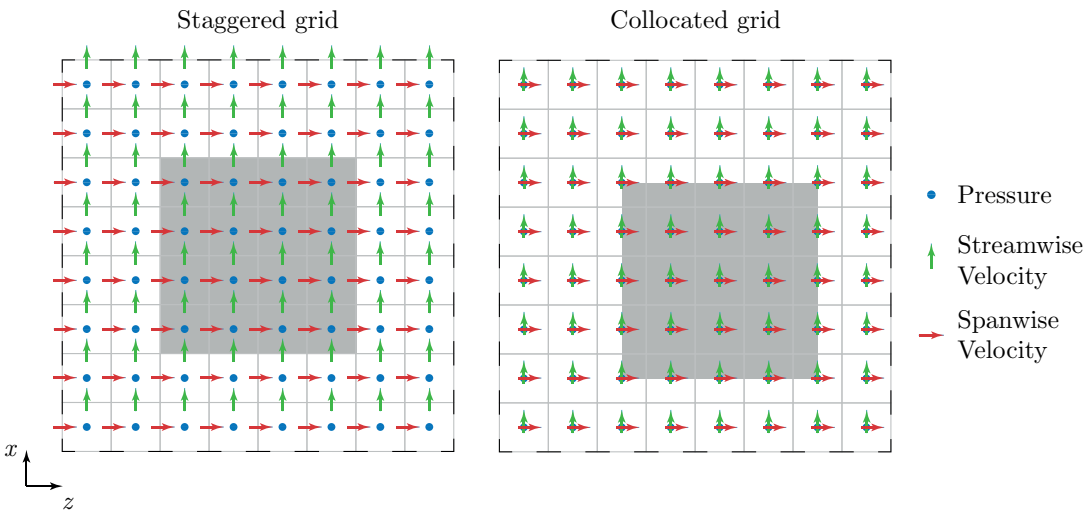

Figure 2.17 – Schematic of discretisations that are staggered and collocated in the streamwise and spanwise directions. (a) staggered grid; (b) collocated grid.

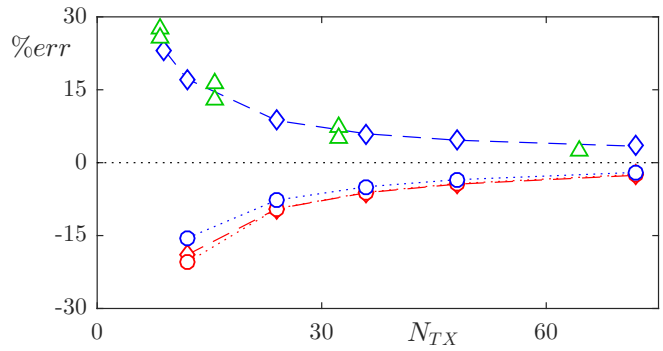

Figure 2.18 – Percentage difference of the measured slip length to the analytic solution for streamwise and spanwise aligned ridges with increasing grid resolution and different discretisations. –◇–, streamwise ridge (finite difference); –◇–, streamwise ridge (Fourier); ···○···, spanwise ridge (finite difference); ···○···, spanwise ridge (Fourier); △, estimated error of streamwise ridge from Türk *et al.* (2014) (DNS finite difference).

discretisation is collocated in the streamwise and spanwise directions while the finite difference discretisation is fully staggered. Both are shown schematically in figure 2.17 including the definition of a post. In this illustrative example, the post has a solid fraction of $\phi_s = 1/4$, with the texture represented using 8 points. Compared to a collocated discretisation, the staggered discretisation has one fewer grid point to define a post for the streamwise velocity in the spanwise direction, and one fewer grid point to define a post for the spanwise velocity in the streamwise direction.

The discrepancy in the post definition is better illustrated by considering streamwise- and spanwise-aligned ridges. The difference to the analytical solutions (Philip, 1972; Lauga & Stone, 2003) for streamwise- and spanwise-aligned ridges is shown in figure 2.18 for both discretisations. With a staggered discretisation, the slip length for the streamwise-aligned ridge is over-predicted. An over-prediction of the slip length for streamwise-aligned ridges, dependent on the spanwise resolution, was also observed in the DNSs of Türk *et al.* (2014). Their slip-length errors are also included in figure 2.18, and are consistent with the grid dependency observed here.

With a staggered discretisation, while the slip length of the streamwise-aligned ridge is over-predicted, conversely, the slip length of the spanwise-aligned ridge is under-predicted. For the collocated discretisation, however, the slip length is under-predicted in both cases. It should be noted that for these ridge textures, only the streamwise velocity is non-zero at the surface so the grid-resolution dependency is only a function of the streamwise velocity discretisation. Comparing the streamwise velocity discretisations, one fewer grid point defines a streamwise-aligned ridge for a

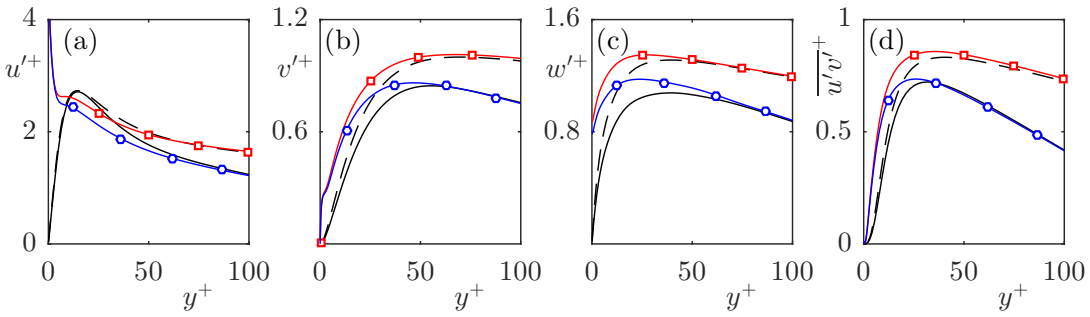

Figure 2.19 – Comparison of the velocity fluctuations and Reynolds stress, $\overline{u'v'}^+$, for the case with $L^+ \approx 35$ at $\mathrm{Re}_\tau \approx 180$ and $\mathrm{Re}_\tau \approx 405$. ——, smooth wall at $\mathrm{Re}_\tau \approx 180$; – –, smooth wall at $\mathrm{Re}_\tau \approx 405$; –○–, case $L^+ \approx 35$ at $\mathrm{Re}_\tau \approx 180$; –□–, case $L^+ \approx 35$ at $\mathrm{Re}_\tau \approx 405$.

staggered grid than a collocated grid, and the error between the two discretisations is nearly symmetric around 0%, as shown in figure 2.18. For a spanwise-aligned ridge the streamwise velocity discretisations use the same number of points, and the errors are consistent. It is possible that with a staggered discretisation of a post, the streamwise/spanwise error nearly cancels, while the error with a collocated discretisation compounds.

2.7 Effect of Reynolds number

To investigate any dependence of the results on the Reynolds number, additional simulations of the cases with $L^+ \approx 24$ and $L^+ \approx 35$ were conducted at $\mathrm{Re}_\tau \approx 405$. At this higher Reynolds number, the rms velocity fluctuations over a smooth wall are larger in magnitude than at $\mathrm{Re}_\tau \approx 180$ (Spalart, 1988; Moser *et al.*, 1999). Therefore, the relative changes to the fluctuations, caused by the presence of the texture, are compared to their corresponding smooth wall. The rms velocity fluctuations and Reynolds stress, $\overline{u'v'}^+$, for the case with $L^+ \approx 35$, shown in figure 2.19, show modifications to the flow in the near-wall region compared to the smooth-wall profiles, which are qualitatively consistent at both Reynolds numbers. Beyond a height $y^+ \approx 50$–75 the fluctuations then collapse to the respective smooth-wall profiles, consistent with the results of Seo *et al.* (2015). These results suggest that the effect of the texture is restricted to the near-wall region and scales in wall units, as conventionally agreed (Martell *et al.*, 2010; Park *et al.*, 2013; Seo *et al.*, 2015).

To compare the dynamics in the overlying flow, premultiplied energy spectra of the three velocities and Reynolds stress, $\overline{u'v'}^+$, for both Reynolds numbers, at a height

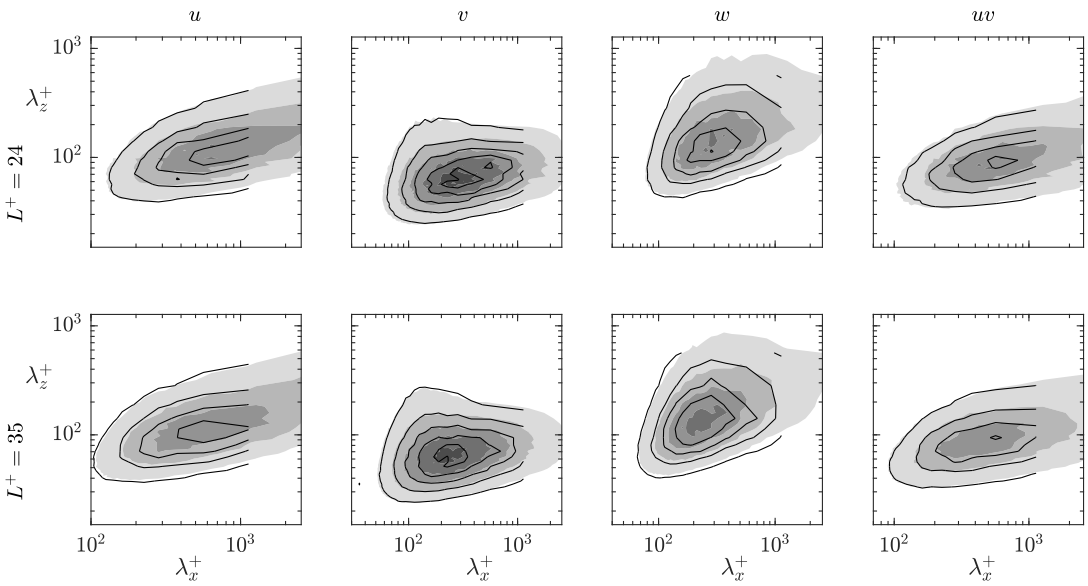

Figure 2.20 – Comparison of the spectral energy densities at $\mathrm{Re}_\tau \approx 180$ and $\mathrm{Re}_\tau \approx 405$ of the three velocities and Reynolds stress, $\overline{u'v'}^+$, for the cases with $L^+ \approx 24$ and $L^+ \approx 35$ at $y^+ = 15$. Filled contour, $\mathrm{Re}_\tau \approx 405$; ——, $\mathrm{Re}_\tau \approx 180$.

$y^+ = 15$ above the surface, are shown in figure 2.20 for the cases with $L^+ \approx 24$ and $L^+ \approx 35$. The spectra are normalised by the respective rms fluctuation at this height for each Reynolds number. The results suggest that the modifications in turbulent dynamics in the overlying flow are essentially independent of the Reynolds number, if the texture is the same in wall units. Therefore, results at the lower Re_τ are relevant to applications at higher Re_τ.

Chapter 3

The influence of surface texture pattern

This chapter investigates how changing the surface texture pattern modifies the slip lengths the surface produces, and the susceptibility of the entrapped gas pockets to deformation. For reduced computational cost, viscous Stokes-flow and laminar simulations are conducted to measure the slip lengths and the pressure fields, from which the gas pocket deformation is approximated. The applicability of these reduced-order models to predict the performance of fully turbulent flows is also investigated.

Parts of this chapter were presented at the 2015 European Drag Reduction and Flow Control Meeting (Fairhall & García-Mayoral, 2015).

3.1 Numerical details

The numerical method for the viscous Stokes flow and laminar simulations follows the same fundamental numerics as outlined in chapter 2. The case-specific simulation set-ups and numerical details are outlined in this section.

3.1.1 Stokes-flow simulation details

The viscous Stokes-flow simulations are shear-driven in a half-channel with one texture element represented. For accuracy and efficiency, most results use a Fourier discretisation with $256 \times 256 \times 64$ grid points in the streamwise, spanwise and wall-normal directions, respectively, with a grid of size $L \times L \times 2.5L$. According to the grid resolution analysis from figure 2.15, the error in the slip length with a Fourier discretisation with 256 grid points per texture element compared to a finite difference discretisation with 48 grid points per texture element is 1.2%. To allow a consistent comparison, results of the Stokes-flow simulations that are compared to the laminar and DNS results are obtained from simulations with 24 grid points per texture element.

3.1.2 Laminar flow simulation details

The numerical code for the laminar simulations is the same as that used for the DNSs in a reduced domain. As with the Stokes-flow simulations, a shear-driven half-channel is simulated with one texture element represented using $24 \times 24 \times 77$ grid points in the streamwise, spanwise and wall-normal directions, respectively, matching the resolution of the DNSs. To allow direct comparison with the DNSs these simulations are run with the same ν, L, and $\partial U/\partial y$ as the corresponding DNSs.

3.2 Influence of texture pattern on the slip length

Firstly the influence of the texture pattern on the mean slip length is explored. The scaling laws for the variation of the slip length with gas fraction are shown in figure 3.1 for textures of streamwise-aligned ridges (Philip, 1972) and isolated posts (Ybert *et al.*, 2007). Textures of spanwise-aligned ridges are not considered as they produce slip lengths half the value of streamwise-aligned ridges in the viscous regime (Lauga & Stone, 2003), making them less attractive for drag reduction applications. For gas fractions $\phi_g = 1 - \phi_s \lesssim 0.9$, the scaling laws indicate that streamwise-aligned ridges produce larger slip lengths for the same gas fraction, while for $\phi_g \gtrsim 0.9$, textures of isolated posts produce larger slip lengths.

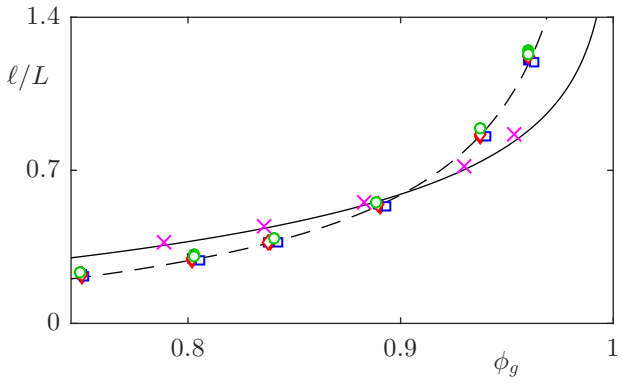

Figure 3.1 – Variation of the slip length with texture size and arrangement in the Stokes-flow limit. ■, square posts in a collocated arrangement; ♦, diamond posts in a collocated arrangement; ●, circular posts in a collocated arrangement; □, square posts in a staggered arrangement; ◇, diamond posts in a staggered arrangement; ○, circular posts in a staggered arrangement; ×, streamwise-aligned ridges; ——, analytical solution for streamwise-aligned ridges (Philip, 1972); – –, scaling law for isolated posts (Ybert *et al.*, 2007).

To investigate the effect that the post shape and arrangement has on the value of the slip length, in this section textures of three different post shapes, square, diamond and circular, in two different arrangements, collocated and staggered, are compared with textures of streamwise-aligned ridges. The resulting slip lengths that these surfaces produce are also shown in figure 3.1. For all textures of isolated posts, the obtained slip lengths follow the scaling law of Ybert *et al.* (2007). In the viscous limit, for the surface textures considered, the post shape and arrangement has negligible effect on the slip length, at least for the large gas fractions considered.

As discussed in section 1.4, if the size of the texture is small then the slip lengths obtained in the viscous limit are appropriate to model the surface by, even in turbulent flows. However, beyond $L^+ \gtrsim 10$, the measured slip length has been shown to be reduced compared to the viscous prediction (Seo & Mani, 2016). While Seo & Mani (2016) proposed a physical model for sufficiently large texture sizes, $L^+ \sim 100$, where $\ell_x^+ \sim (L^+)^{1/3}/\sqrt{\phi_s}$, a physical model for the variation of the slip length in-between the Stokes regime and the model proposed by Seo & Mani (2016) is still missing.

To investigate whether this initial deviation from the viscous prediction is a result of advective effects, the slip lengths from laminar simulations are now considered. The textures considered are square and diamond posts in collocated and staggered arrangements with a solid fraction $\phi_s = 1/9$. The resulting variation of the slip lengths with texture size are shown in figure 3.2 and are compared to the obtained

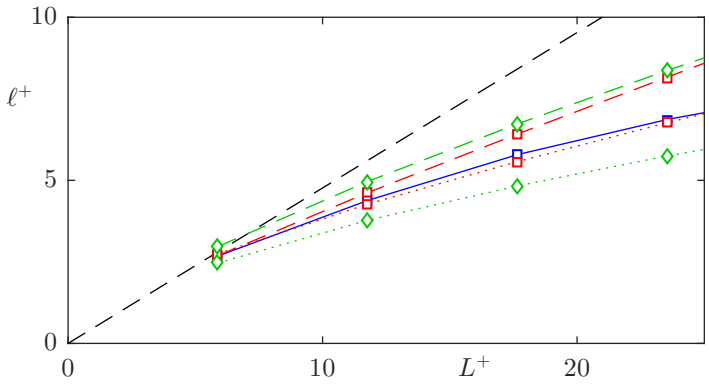

Figure 3.2 – Variation of the slip length with texture size. – –, square posts in a collocated arrangement (viscous); –□–, square posts in a collocated arrangement (DNS); – □ –, square posts in a collocated arrangement (laminar); ···□···, square posts in a staggered arrangement (laminar); – ◇ –, diamond posts in a collocated arrangement (laminar); ···◇···, diamond posts in a staggered arrangement (laminar).

slip lengths from the DNS results, which have a texture of collocated square posts. The laminar simulations capture the initial deviation of the DNS slip lengths from the viscous prediction, which suggests that this initial deviation is due to advective effects. However, these laminar simulations still fail to predict the slip length beyond $L^+ \gtrsim 20$, where the slip length tends to the relation proposed by Seo & Mani (2016). These results also show that collocated arrangements outperform staggered arrangements when advective effects become important. This could be a result of the blockage effect of the staggered arrangements, which is more significant for the staggered diamond shaped posts. This blockage effect is also present in random surface textures, and has been attributed to their reduced slip lengths compared to regular textures (Seo & Mani, 2018).

3.3 Influence of texture pattern on gas pocket deformation

Next, the effect of the surface texture on the susceptibility of the gas pockets to deformation is investigated. The texturing of the surface causes deceleration and acceleration of flow around texture elements, which generates a texture-coherent pressure field. This pressure field results in a static deformation of the gas pockets (Seo *et al.*, 2015) and is strongly influenced by the post shape. Using the pressure fields at the surface, the texture-coherent deformation in the viscous regime is now estimated

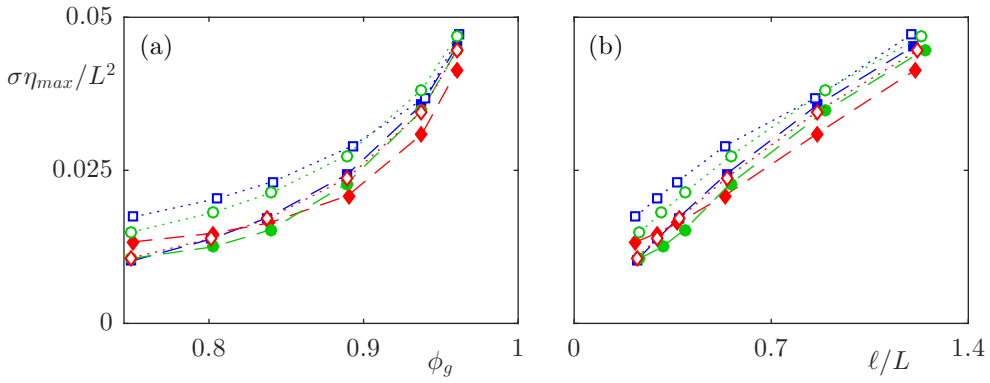

Figure 3.3 – Normalised maximum gas pocket deformation of the Stokes-flow simulations using the pressure obtained from the flow fields against (a) gas fraction and (b) the measured slip length. –■–, square posts in a collocated arrangement; –♦–, diamond posts in a collocated arrangement; –●–, circular posts in a collocated arrangement; ···□···, square posts in a staggered arrangement; ···◇···, diamond posts in a staggered arrangement; ···○···, circular posts in a staggered arrangement.

using the Young-Laplace equation,

$$\nabla^2\eta \approx \frac{\Delta p}{\sigma}, \tag{3.1}$$

where η is the gas pocket deformation measured from the surface plane, Δp is the pressure difference across the liquid-gas interface and σ is the surface tension. The pressure in the gas pockets is assumed to be homogeneous and is adjusted to ensure conservation of mass within the gas pockets (Seo *et al.*, 2015). It should be noted that streamwise-aligned ridges generate no pressure variations due to the streamwise homogeneity of the surface.

The maximum deformation for each surface texture in the viscous limit is shown in figure 3.3. These results show that square and circular staggered arrangements generate larger coherent deformation than collocated arrangements. The evidence suggests that the larger streamwise spacing between adjacent posts provides both a lower resistance to deformation and a larger slip velocity between posts, which generates a larger stagnation pressure. Diamond-shaped posts result in smaller deformations, perhaps due to the smaller streamwise separation between adjacent posts and their ability to direct the flow around the posts, which reduces the stagnation pressure.

Figure 3.4 shows that the trends in the laminar regime are broadly similar to those in the viscous regime. Diamond-shaped posts have smaller deformations than square posts, and collocated arrangements outperform staggered arrangements. In the laminar regime, diamond posts, therefore, not only appear to produce slightly

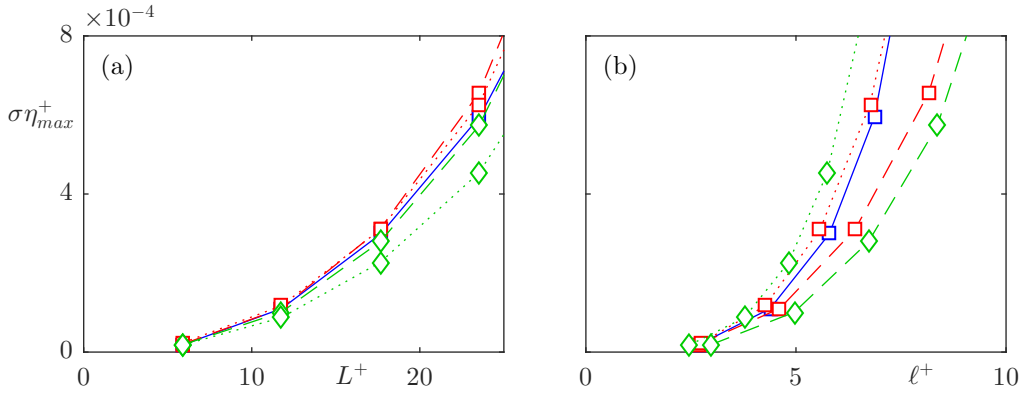

Figure 3.4 – Variation of maximum gas pocket deformation using the pressure obtained from the flow fields with (a) texture size and (b) the measured slip length. –□–, square posts in a collocated arrangement (DNS); – □ –, square posts in a collocated arrangement (laminar); ···□···, square posts in a staggered arrangement (laminar); – ◇ –, diamond posts in a collocated arrangement (laminar); ···◇···, diamond posts in a staggered arrangement (laminar).

larger slip lengths than square posts, as shown in figure 3.2, but also smaller static deformations. The laminar simulations are also able to accurately predict the static deformations obtained from the DNSs up to $L^+ \lesssim 20$. For $L^+ \gtrsim 20$, the laminar simulations produce larger slip compared to the DNS results, and therefore a larger stagnation pressure. This larger stagnation pressure results in a larger deformation of the gas pockets, explaining the discrepancy for $L^+ \gtrsim 20$. Nevertheless, the ability of laminar simulations to predict not only the slip-lengths but also the texture-coherent deformations of fully turbulent simulations up to $L^+ \lesssim 20$ is an improvement on the viscous predictions limited to $L^+ \lesssim 10$.

Chapter 4

The suitability of slip-length models for textured surfaces

This chapter focuses on the applicability of modelling textured surfaces using homogeneous slip lengths. A spectral approach is used to analyse the slip length experienced by different lengthscales in the overlying flow. This chapter will show that the perceived slip length, obtained straight from the velocity fields, is contaminated by the texture-induced flow resulting from the texture. However, once the texture-induced flow is filtered from the velocity fields it will be shown that the overlying turbulence experiences the surface as a homogeneous slip length boundary condition. The discrepancy of ΔU^+ between texture-resolved and homogeneous slip simulations, therefore, cannot be attributed to the overlying flow not perceiving the surface as producing a homogeneous slip effect, which will be investigated in chapter 6.

Parts of this chapter have been published in Fairhall & García-Mayoral (2018) and are submitted for publication in Fairhall et al. *(2019). The results were also presented at the 2017 European Drag Reduction and Flow Control Meeting (Fairhall & García-Mayoral, 2017*a*) and 2017 American Physical Society Division of Fluid Dynamics Meeting (Fairhall & García-Mayoral, 2017*b*).*

4.1 Correlation between surface velocity and shear

As discussed in section 1.7, previous works analysing the drag reduction performance of superhydrophobic surfaces have modelled the surface using homogeneous slip lengths (Min & Kim, 2004; Busse & Sandham, 2012). The concept of a homogeneous slip-length model assumes that the size of the texture is much smaller than the size of the turbulent eddies in the overlying flow (Bechert & Bartenwerfer, 1989). Seo & Mani (2016) investigated the applicability of homogeneous slip length models for textured surfaces and showed that as the surface texture becomes of the order of the near-wall turbulent scales, that is $L^+ \sim \mathcal{O}(10)$, the velocity and shear appear to lose correlation. This loss of correlation between the velocity and shear invalidates the concept of a homogeneous slip-length model, as the slip length is the ratio of the two, i.e. $\ell = u_s/\partial u/\partial y|_s$. The work of Seo & Mani (2016) considered the slip length experienced by individual texture elements. They assessed the correlation of the texture-averaged velocity and texture-averaged shear ($\partial u/\partial y$) at the surface. While this method showed that, at the texture scale, correlation appears to be lost, it does not show whether lengthscales much larger than the texture size still experience the averaged effect of the texture, i.e., a slip length.

To allow discrimination between lengthscales, in this thesis, the slip length is analysed using a spectral approach. In a spectral framework, for each Fourier mode, the slip length is characterised by both a magnitude and a phase, with the phase having streamwise and spanwise components. The phase of the slip length, φ, represents the phase lag between the velocity and shear at the surface. For a given wavelength, λ, the phase is $\varphi = 2\pi\Delta/\lambda$, where Δ is the spatial offset between the velocity and shear. For a homogeneous slip-length model to be valid, the measured slip length should have a magnitude that is constant in time and across all wavelengths, with the velocity and shear in phase. In the following discussion, two slip lengths will be referred to, the mean slip length and the dynamic slip length. The mean slip length, $\overline{\ell}_x^+$, is the time-average of the slip length experienced by the streamwise zero mode, i.e., it is the slip length experienced by the mean velocity. The dynamic slip length, $\widehat{\ell}^+$, is the time-averaged slip length experienced by the velocity fluctuations (Seo & Mani, 2016). The dynamic slip length is obtained from a linear fit of the instantaneous velocity and shear fluctuations.

The correlation between velocity and shear observed for small texture sizes (Seo & Mani, 2016) is demonstrated in figure 4.1, which shows both the slip length magnitudes and phases for the case with $L^+ \approx 12$. Only a small scatter is present in the observed slip length magnitude and phases. The wavelengths shown are $\lambda_x^+ \approx 113$ – 1131 and

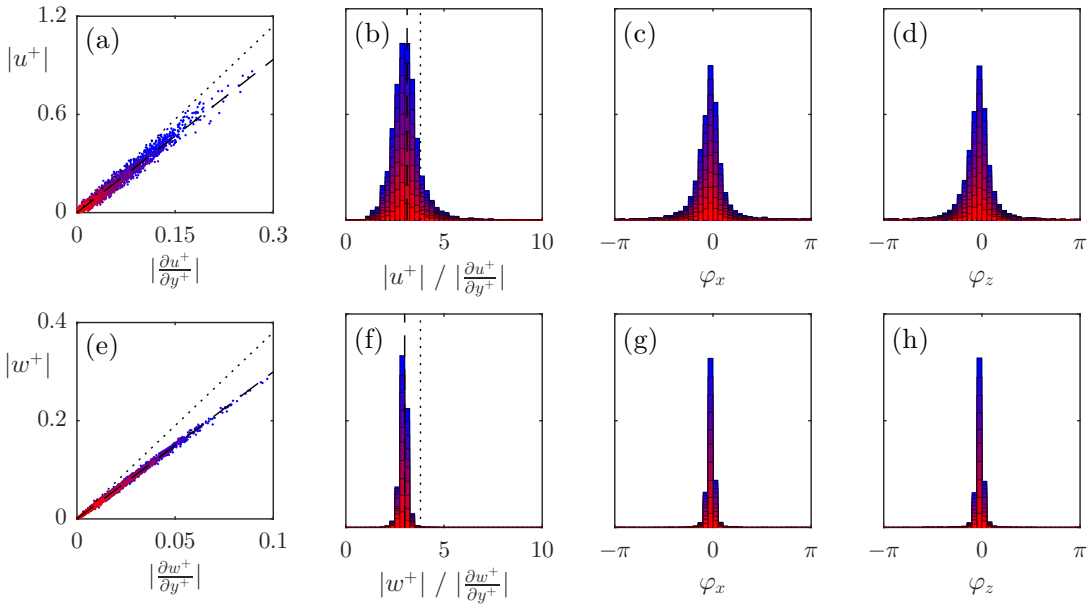

Figure 4.1 – Instantaneous streamwise (top) and spanwise (bottom) slip lengths of wavelengths $\lambda_x^+ \approx 113 - 1131$ and $\lambda_z^+ \approx 113 - 565$ (coloured from red to blue for increasing streamwise wavelength) for the case with $L^+ \approx 12$ obtained from the full velocity fields. (a,e) instantaneous correlation of velocity and shear magnitudes; (b,f) probability density histogram of the slip length; streamwise (c,g) and spanwise (d,h) phase difference between velocity and shear. In (a,b,e,f) the dashed line indicates the fitted dynamic slip length, obtained from a linear regression of the data points, and the dotted line indicates the mean slip length.

$\lambda_z^+ \approx 113$ – 565. These are lengthscales relevant to the near-wall turbulent dynamics, being of the order of the near-wall vortices and streaks, and are lengthscales larger than the texture wavelength. For this case, the dynamic slip lengths are $\widehat{\ell}_x^+ = 3.3$ and $\widehat{\ell}_z^+ = 3.0$. In comparison, the mean streamwise slip length is $\overline{\ell}_x^+ = 3.8$. The fluctuations of this size, therefore, appear to experience a slightly smaller slip length than the mean flow. This is consistent with the results of Seo & Mani (2016) for small textures. However, the lengthscales relevant to the near-wall turbulent dynamics experience no significant variation in the slip lengths.

As the texture size is increased to $L^+ \approx 24$, which is of the order of the diameter of near-wall vortices (Blackwelder & Eckelmann, 1979), there is still a strong correlation between the spanwise velocity and shear, as shown in figure 4.2. However, the correlation becomes significantly weaker in the streamwise direction, even for lengthscales an order of magnitude larger than the texture size. These lengthscales, therefore, no longer appear to experience just the averaged effect of the texture. For this case,

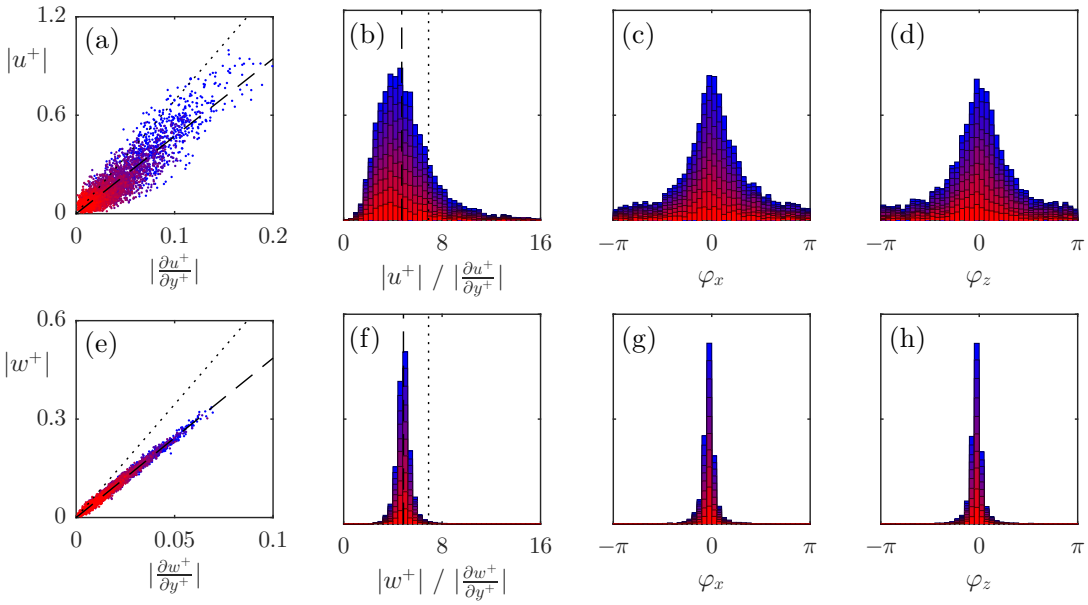

Figure 4.2 – Instantaneous streamwise (top) and spanwise (bottom) slip lengths of wavelengths $\lambda_x^+ \approx 113 - 1131$ and $\lambda_z^+ \approx 113 - 565$ (coloured from red to blue for increasing streamwise wavelength) for the case with $L^+ \approx 24$ obtained from the full velocity fields. (a,e) instantaneous correlation of velocity and shear magnitudes; (b,f) probability density histogram of the slip length; streamwise (c,g) and spanwise (d,h) phase difference between velocity and shear. In (a,b,e,f) the dashed line indicates the fitted dynamic slip length, obtained from a linear regression of the data points, and the dotted line indicates the mean slip length.

the time-averaged dynamic slip lengths are $\widehat{\ell}_x^+ = 5.2$ and $\widehat{\ell}_z^+ = 4.8$, with the mean streamwise slip length $\overline{\ell}_x^+ = 6.9$. The fluctuations, therefore, appear to experience significantly smaller slip lengths than the mean flow. The streamwise dynamic slip length is, however, beginning to lose physical significance due to the large fluctuations in its instantaneous value. As the texture size is further increased to $L^+ \approx 47$, shown in figure 4.3, the correlation between velocity and shear becomes still weaker. The fitted dynamic slip lengths for this case are also significantly reduced compared to the mean slip length, being $\widehat{\ell}_x^+ = 6.1$ and $\widehat{\ell}_z^+ = 4.1$ with $\overline{\ell}_x^+ = 10$. While the dynamic slip lengths have lost physical significance due to their fluctuations, should they experience only small oscillations around a mean value, at a timescale faster than the overlying turbulent structures perceive, then it could still be reasonable to model the surface by the time-averaged value. To assess this, time histories of the instantaneous slip lengths for different lengthscales are shown in figure 4.4. These show that for the largest texture, $L^+ \approx 47$, the fluctuations are large compared to the mean, and their

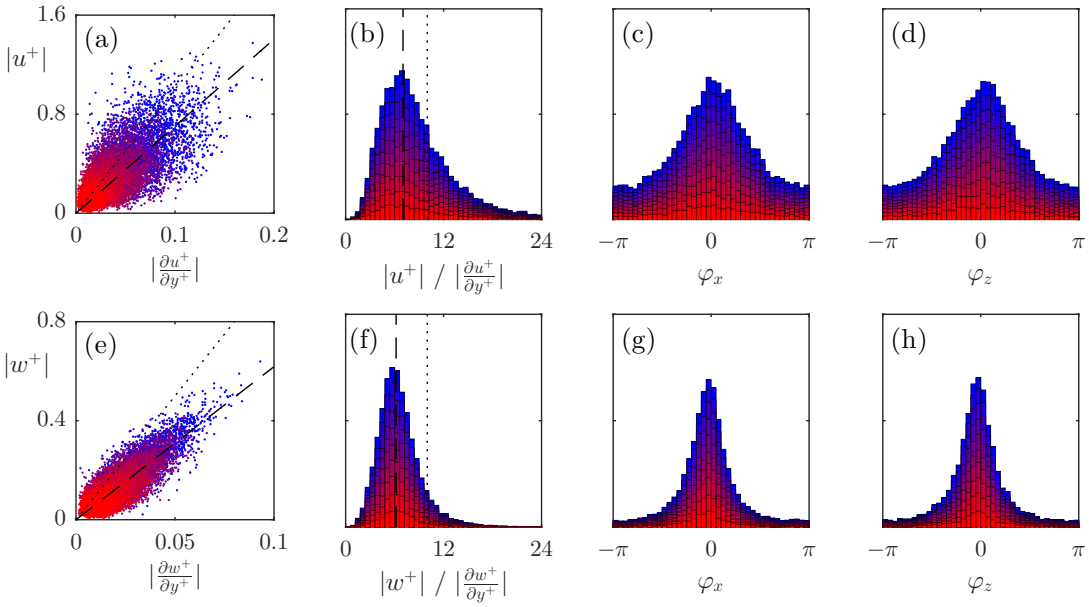

Figure 4.3 – Instantaneous streamwise (top) and spanwise (bottom) slip lengths of wavelengths $\lambda_x^+ \approx 113 - 1131$ and $\lambda_z^+ \approx 113 - 565$ (coloured from red to blue for increasing streamwise wavelength) for the case with $L^+ \approx 47$ obtained from the full velocity fields. (a,e) instantaneous correlation of velocity and shear magnitudes; (b,f) probability density histogram of the slip length; streamwise (c,g) and spanwise (d,h) phase difference between velocity and shear. In (a,b,e,f) the dashed line indicates the fitted dynamic slip length, obtained from a linear regression of the data points, and the dotted line indicates the mean slip length.

timescale is comparable to that of near-wall eddies, typically $0.1\ \delta/u_\tau$ at $\mathrm{Re}_\tau \simeq 180$. A time-averaged dynamic slip-length model, therefore, appears to not be an appropriate model to represent the surface.

The correlations in figures 4.1 to 4.3 only portray a subset of wavelengths in the overlying flow. To assess the correlation over the full range, figure 4.5 extends this analysis to time-averaged spectral maps of the dynamic slip lengths. For reference, the spectral energy densities for the corresponding velocities at a height $y^+ = 15$ above the surface are overlayed, to indicate the energetically-relevant lengthscales in the overlying flow. The spectral maps show that lengthscales of the order of the texture size appear to experience significantly reduced slip-lengths, while lengthscales much larger than the texture size appear to experience, on average, a slip length different to the value of the mean slip length. However, the instantaneous correlations in figure 4.4 showed that the concept of a time-averaged slip length loses validity beyond $L^+ \gtrsim 24$.

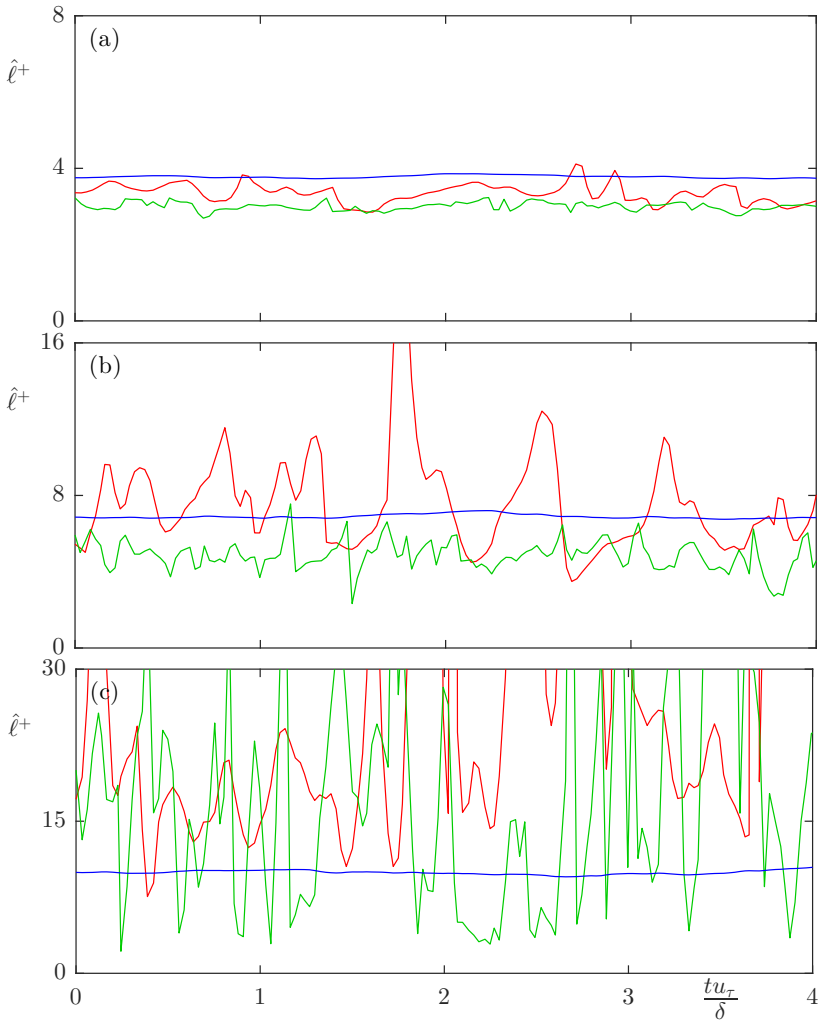

Figure 4.4 – Time history of instantaneous slip lengths for the cases with (a) $L^+ \approx 12$; (b) $L^+ \approx 24$; (c) $L^+ \approx 47$. ——, streamwise slip length of the mean flow; ——, streamwise slip length for $\lambda_x^+ \approx 1131$ and $\lambda_z^+ \approx 94$; ——, spanwise slip length for $\lambda_x^+ \approx 188$ and $\lambda_z^+ \approx 94$.

4.2 Contamination of the perceived slip length by the texture-induced flow

To investigate the source of this apparent loss of correlation, profiles in y of the spectral, time-averaged streamwise energy, $\widehat{E}_{uu}^+$, are investigated. Figure 4.6 shows these profiles for the cases with $L^+ \approx 12$, 24 and 47, and for a smooth-wall case for reference. Since the energy magnitude for each wavelength is not relevant for this investigation, only with the shape of the profiles, the results are normalised with their value at a reference height of $y^+ = 15$. The lengthscales shown correspond to $\lambda_x^+ \approx$

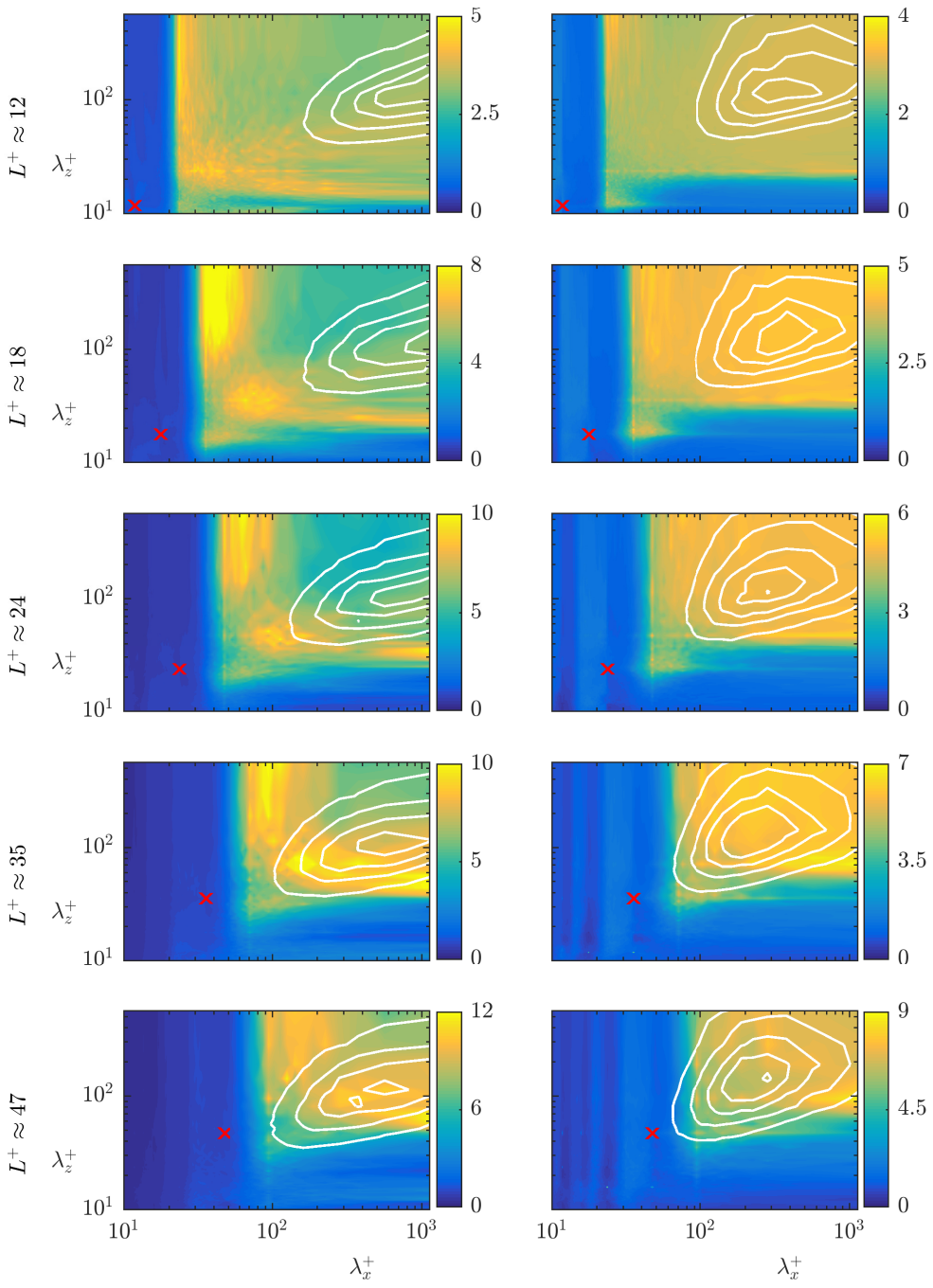

Figure 4.5 – Spectral maps of the time-averaged slip lengths obtained from the full velocity fields (filled contour) for the streamwise (left) and spanwise (right) directions, for the cases with $L^+ \approx 12$ to 47 shown from top to bottom. Spectral energy density of the corresponding velocity at a height of $y^+ = 15$ (lined contour). The red cross indicates the wavelength of the texture.

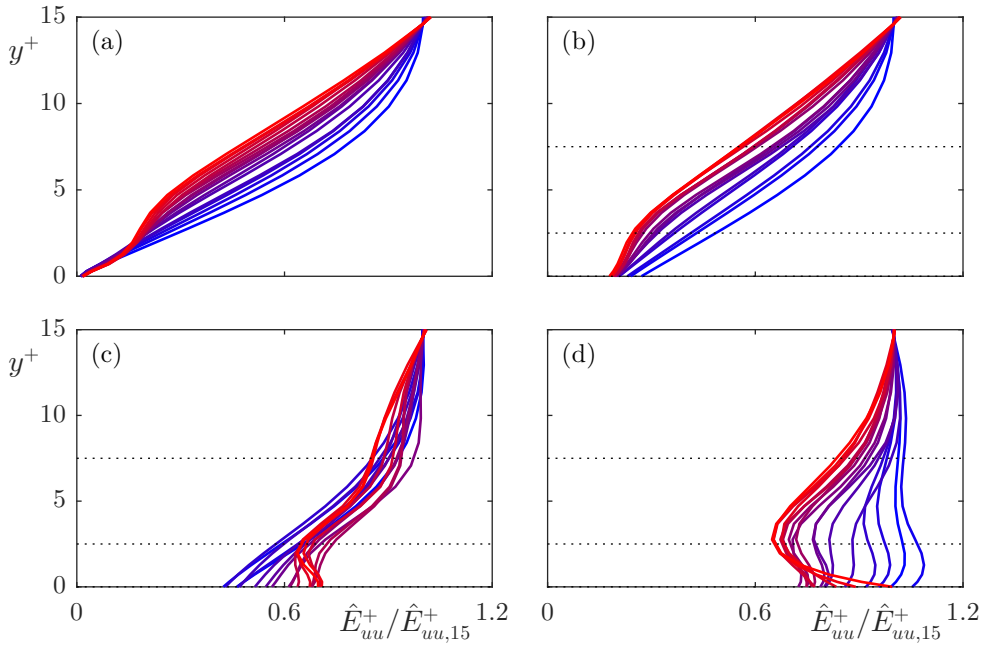

Figure 4.6 – Wavelength-dependent profiles of the streamwise energy spectrum from the full velocity signal, $\widehat{E}^+_{uu}$, normalised by their value at $y^+ = 15$, for wavelengths $\lambda^+_x \approx 60 - 377$ and $\lambda^+_z \approx 94$ coloured from red to blue for increasing streamwise wavelength. (a) smooth wall; (b) case with $L^+ \approx 12$; (c) case with $L^+ \approx 24$; (d) case with $L^+ \approx 47$. The dotted lines indicate reference heights of $y^+ = 2.5$ and 7.5.

60 to 377 and $\lambda^+_z \approx 94$, coloured from red to blue. As with figures 4.1 to 4.3, these are lengthscales larger than the texture wavelengths. The extrapolation of these profiles to their virtual origins gives the apparent slip length experienced by each wavelength.

For the case with $L^+ \approx 12$, the predominant effect of the surface on these energy profiles is a shift due to the slip at the surface, with the shape of the profiles essentially otherwise unmodified compared with the smooth wall profiles. This indicates that the predominant effect of the surface, for this texture size, is the direct effect of the surface slip. For the cases with $L^+ \approx 24$ and 47, however, there is a clear secondary effect near the surface, an additional energy that decays with height above the surface. This additional energy is consistent with the energy produced by the coherent flow induced directly by the texture (Türk *et al.*, 2014; Jelly *et al.*, 2014; Seo *et al.*, 2015). The triple decomposition (Reynolds & Hussain, 1972), is commonly used to assess the strength of the texture-coherent fluctuations. This decomposition splits the velocity fields into a time-averaged component, a texture-coherent component and the turbulent, background fluctuations,

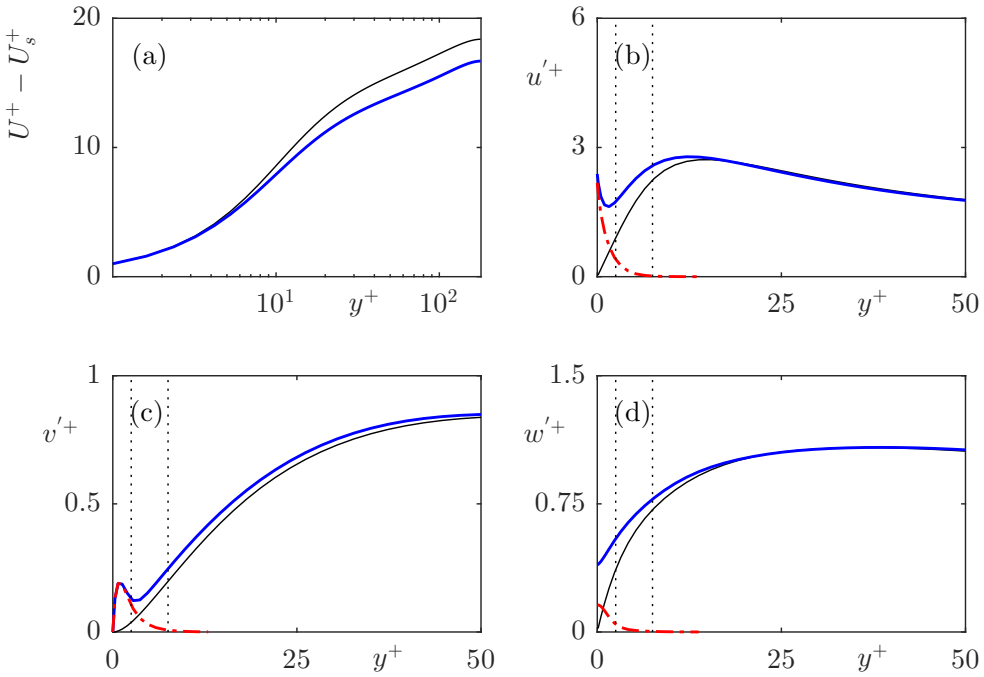

Figure 4.7 – Turbulent statistics for the case with $L^+ \approx 12$. (a) Mean velocity profile with the slip velocity subtracted (b–d) rms velocity fluctuations. ——, smooth wall; ——, full velocity fluctuation; · –, texture-induced coherent fluctuation obtained from the triple decomposition. The dotted lines indicate reference heights of $y^+ = 2.5$ and 7.5.

$$u(x,y,z,t) = U(y) + u'(x,y,z,t) = U(y) + \widetilde{u}(\widetilde{x},y,\widetilde{z}) + u_T(x,y,z,t), \tag{4.1}$$

where $U(y)$ is the mean velocity at a given height and $u'(x,y,z,t)$ is the total fluctuation. By considering the periodicity of the texture, u' is further decomposed into the texture-induced coherent fluctuations, $\widetilde{u}(\widetilde{x},y,\widetilde{z})$, where $\widetilde{x}$ and $\widetilde{z}$ refer to the local coordinates within the texture period, and the remaining velocity fluctuation $u_T(x,y,z,t)$. The velocity $\widetilde{u}(\widetilde{x},y,\widetilde{z})$ directly results from the presence of the texture, which is periodic over texture elements. This triple decomposition has previously been used to assess the strength of the texture-induced flow over superhydrophobic surfaces (Türk *et al.*, 2014; Jelly *et al.*, 2014; Seo *et al.*, 2015).

The rms profiles of the texture-induced coherent contribution, $\widetilde{u}$, for the cases with $L^+ \approx 12$, 24 and 47 are shown in figures 4.7 to 4.9, respectively, together with the total rms fluctuation u'. While the rms of the coherent contribution shows the magnitude and decay rate of the texture-induced flow, it does not show how the texture-induced flow is distributed amongst lengthscales. For this, the pre-multiplied energy spectra of

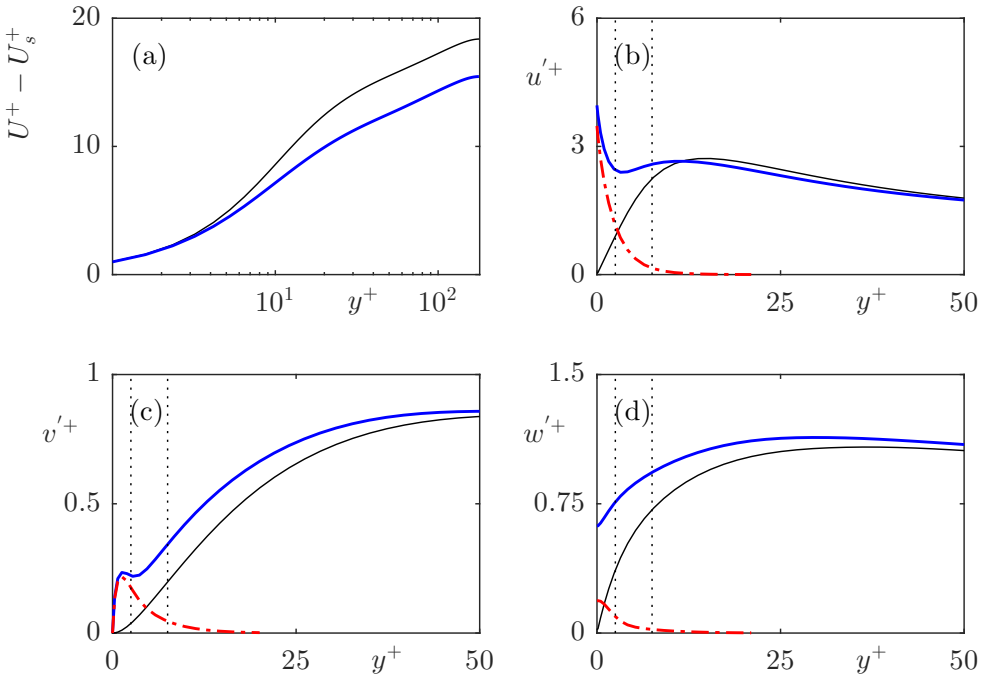

Figure 4.8 – Turbulent statistics for the case with $L^+ \approx 24$. (a) Mean velocity profile with the slip velocity subtracted (b–d) rms velocity fluctuations. ——, smooth wall; ——, full velocity fluctuation; · –, texture-induced coherent fluctuation obtained from the triple decomposition. The dotted lines indicate reference heights of $y^+ = 2.5$ and 7.5.

the velocities are analysed. The streamwise and spanwise pre-multiplied energy spectra at heights $y^+ = 0$, 2.5 and 7.5 for the cases with $L^+ \approx 12$, 24 and 47 are shown in figures 4.10 and 4.11, respectively. The equivalent pre-multiplied energy spectra for a smooth wall, which has been shifted in the wall-normal direction by the mean streamwise slip length, are overlayed for comparison. These energy spectra show energy at lengthscales consistent with smooth wall-like turbulence, and energy at lengthscales of the texture size, directly induced by the presence of the texture. In addition the interaction of the texture-induced flow with the overlying turbulent flow results in texture-induced energy propagating to the lengthscales of the overlying turbulence. The texture-coherent flow is modulated in intensity by the background turbulent flow, a phenomenon that has also be observed in rough surfaces (Abderrahaman-Elena & García-Mayoral, 2016). It is worth noting that the triple decomposition cannot filter this texture-induced flow from u_T, as it is only able to filter the wavelength of the texture size and its sub-harmonics. From this energy spectra, it is clear that the texture-induced flow propagates across the full range of turbulent lengthscales. The spectra for texture sizes beyond $L^+ \approx 24$ show this interaction directly affecting the

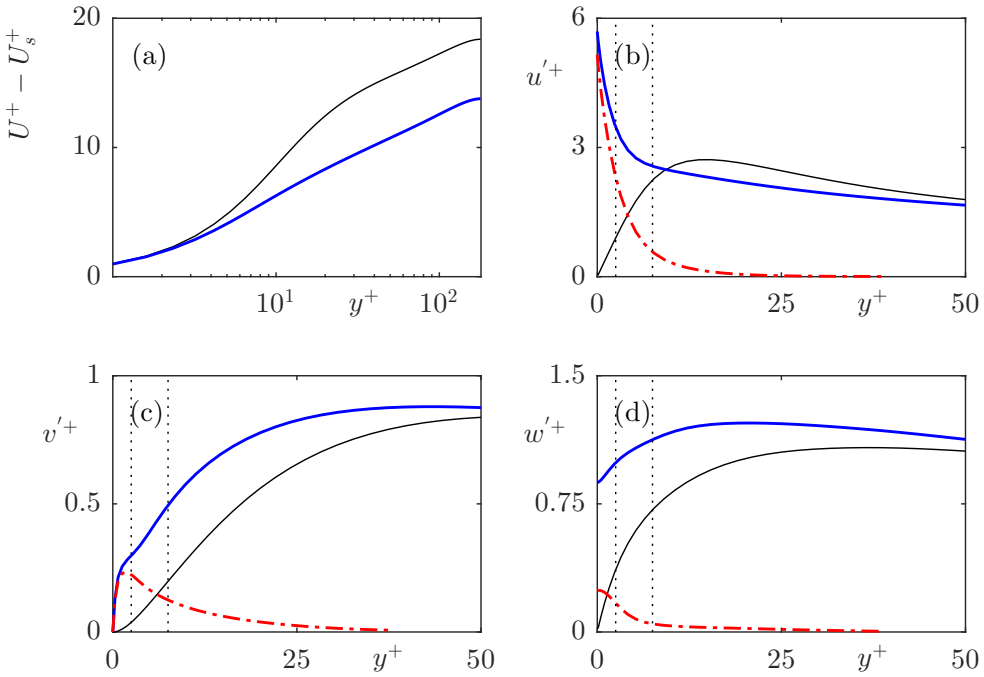

Figure 4.9 – Turbulent statistics for the case with $L^+ \approx 47$. (a) Mean velocity profile with the slip velocity subtracted (b–d) rms velocity fluctuations. ——, smooth wall; ——, full velocity fluctuation; · –, texture-induced coherent fluctuation obtained from the triple decomposition. The dotted lines indicate reference heights of $y^+ = 2.5$ and 7.5.

turbulent lengthscales.

The magnitude of scattered energy that individual lengthscales experience depends on the texture lengthscale, but more importantly on the magnitude of the texture-induced energy. For example, for the case with $L^+ \approx 24$, the spanwise velocity and shear showed correlation, but the streamwise velocity and shear did not. The rms fluctuations and energy spectra for this case show a significantly stronger energy of the texture-induced flow for the streamwise velocity compared to the spanwise velocity. The energy spectra also show that the texture-induced flow of the spanwise velocity has essentially decayed by $y^+ = 2.5$. However, there is still texture-induced energy in the streamwise velocity at this height, which decays by a height $y^+ = 7.5$. The weaker spanwise texture-induced flow scatters to the turbulent lengthscales to a lesser extent, explaining why the spanwise slip length was better correlated for this case than the streamwise slip length.

From a Fourier perspective, the texture-induced flow can scatter to the full wavenumber space through the boundary conditions. The surface texture consists of alternating regions of no-slip and free-slip, described by the wavelength of the texture size and

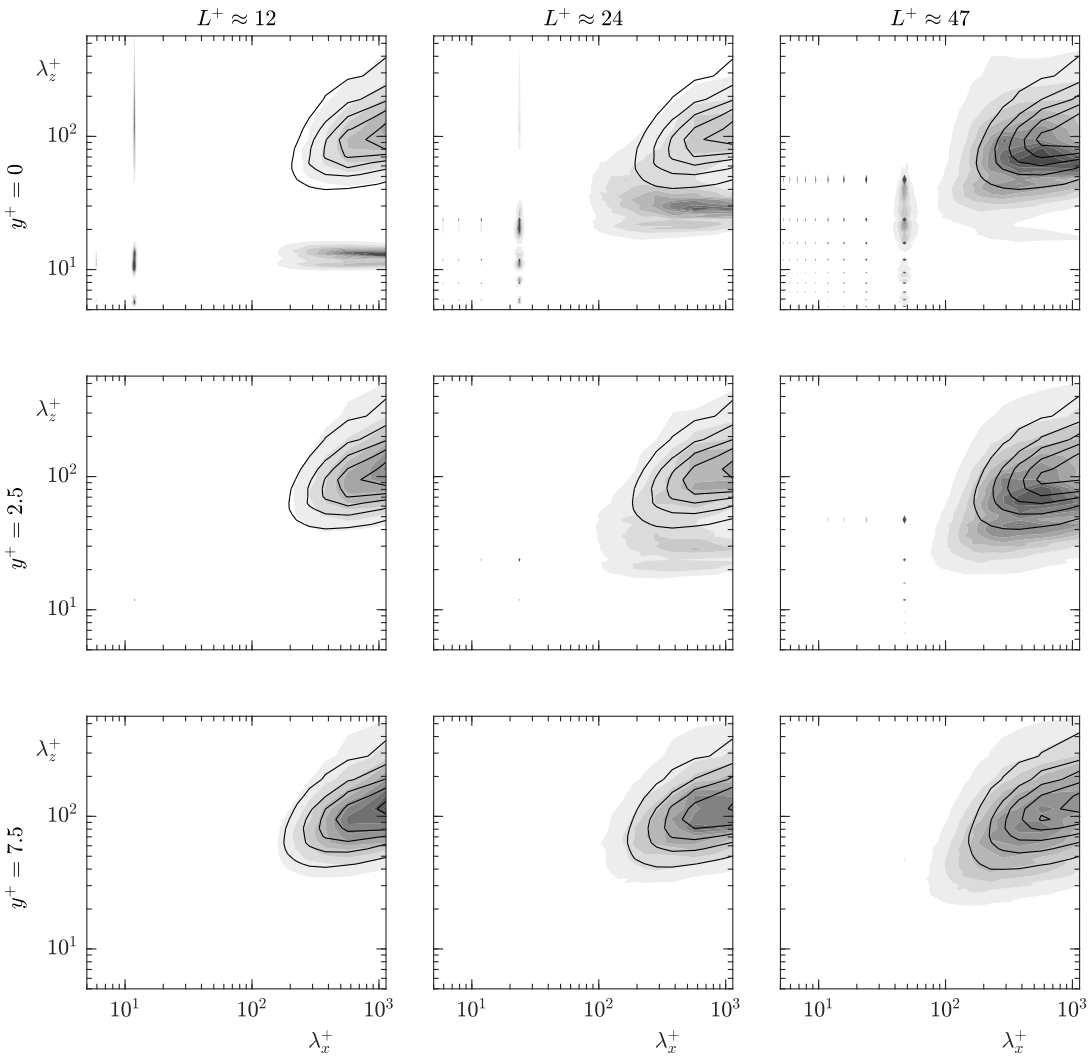

Figure 4.10 – Pre-multiplied energy spectra from the full signal of the streamwise velocity for the cases with $L^+ \approx 12$, 24 and 47 at heights $y^+ = 0$, 2.5, 7.5. Textured case (filled contours), smooth wall case shifted in y^+ by the mean slip length (lined contours).

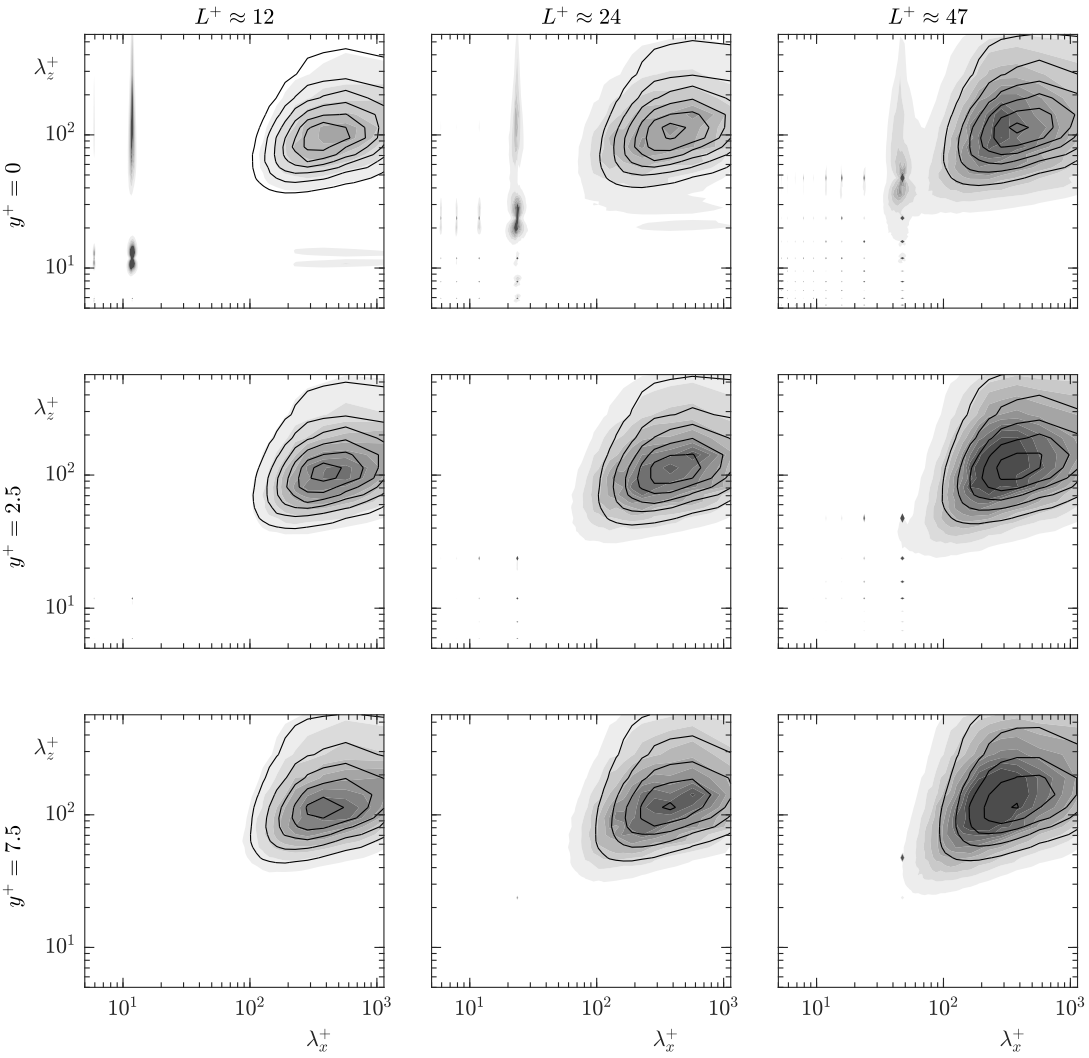

Figure 4.11 – Pre-multiplied energy spectra from the full signal of the spanwise velocity for the cases with $L^+ \approx 12$, 24 and 47 at heights $y^+ = 0$, 2.5, 7.5. Textured case (filled contours), smooth wall case shifted in y^+ by the mean slip length (lined contours).

its subharmonics. The boundary condition is, in Fourier space, a convolution between these texture modes and all the velocity modes. Through this convolution, the texture-induced flow can scramble to all the background turbulent modes. This scattering of the texture-induced flow to the full wavenumber space, evidenced in the pre-multiplied energy spectra in figures 4.10 and 4.11, and in the energy profiles in figure 4.6, results in the measured slip length being contaminated by the texture-induced flow.

To assess the slip length experienced by the overlying flow, this texture-induced flow needs to be filtered out from the velocity fields. The next section, therefore, focuses on how the background turbulent flow can be isolated from the full velocity fields.

4.3 Modified triple decomposition for textured surfaces

Abderrahaman-Elena & García-Mayoral (2016) proposed a modification to the triple decomposition to account for the modulation in intensity of the texture-coherent flow,

$$u(x,y,z,t) \approx U(y) + \widetilde{u}_u(\widetilde{x},y,\widetilde{z})\left(\frac{U(y)+u_T(x,y,z,t)}{U(y)}\right) + u_T(x,y,z,t). \tag{4.2}$$

Here, the terms have the same definitions as in equation (4.1), with an additional multiplier on the texture-coherent flow to account for its modulation. Note that the subscript of the texture-coherent flow denotes the flow direction for which the texture-coherent flow is obtained from. Abderrahaman-Elena & García-Mayoral (2016) showed that this modulated form of the triple decomposition was more effective at removing the footprint of the texture from u_T for their rough surfaces.

The decomposition in equation (4.2) can be used to filter out the texture-induced flow for the streamwise velocity fields. The same principle of modulation of the texture-coherent flow can be applied to the spanwise velocity. In addition to the texture-induced flow generated by the streamwise velocity, the texture-induced flow generated by spanwise velocity also needs to be considered. While the mean spanwise velocity is zero, transverse local flow around texture elements is induced by the fluctuating, background w_T, which generates a texture-coherent flow $\widetilde{w}^*_w(\widetilde{x},y,\widetilde{z}^*)$. To account for the leftwards and rightwards fluctuations, the '$*$' superscript denotes the directional, conditional average of the spanwise velocity (García-Mayoral & Jiménez, 2011). This is obtained by calculating the mean spanwise velocity over a period of texture to determine the local direction of the spanwise flow above the texture element. If the flow is rightwards, the flow around the texture element is added to the ensemble average, $\widetilde{w}^*_w(\widetilde{x},y,\widetilde{z}^*)$, and if the flow is leftwards, a specular image of the flow around

the texture element is added to the ensemble average. The resulting decomposition of the spanwise velocity is then,

$$w(x,y,z,t) \approx \widetilde{w}_u(\widetilde{x},y,\widetilde{z})\left(\frac{U(y)+u_T(x,y,z,t)}{U(y)}\right) + \widetilde{w}^*_w(\widetilde{x},y,\widetilde{z}^*)\left(\frac{w_T(x,y,z,t)}{\overline{w}^*(y)}\right) + w_T(x,y,z,t), \tag{4.3}$$

where $\overline{w}^*(y)$ is the mean of $\widetilde{w}^*_w(\widetilde{x},y,\widetilde{z}^*)$ at a given height. Further details of this decomposition, for all three velocities, are given in Abderrahaman-Elena *et al.* (2019).

The result of the above decomposition minimises the signature of the texture in u_T and w_T. These will be referred to as the 'turbulent' components in the following discussions. Instantaneous flow fields for the full streamwise and spanwise velocities at the surface for the case with $L^+ \approx 12$ are shown in figure 4.12, together with the turbulent velocity fields obtained from both the conventional triple decomposition, equation (4.1), and the modulated triple decompositions of equations (4.2–4.3). The effectiveness of the decompositions at isolating the turbulent components of the velocities beyond any given instant can be better elucidated from two-dimensional premultiplied energy spectra, as shown in figure 4.13 for the streamwise and spanwise velocities at the surface. The relative magnitudes of the energy distribution are clearer after collapsing the data into one-dimensional spectra, as shown in figure 4.14. The turbulent components of the flow fields obtained from the decomposition should contain no energy at the texture lengthscales or the modulated texture-induced flow lengthscales. As discussed in section 4.2, the conventional triple decomposition partially filters out the texture-coherent energy at the wavelengths of the texture, but it has no mechanism to filter out wavelengths larger than the texture size, leaving a footprint of the texture in the velocity snapshots and significant energy in the energy spectra. In physical space, this can be interpreted as the triple decomposition yielding a too intense coherent flow where the overlying, driving flow is weak, and vice versa. In contrast, the modulated triple decomposition is better able to capture and filter out the texture-induced flow.

For the spanwise velocity the turbulent component contains only a small amount of energy of the texture-induced flow around the texture wavelength. The turbulent component of the streamwise velocity shows energy from modulation of the texture-induced flow in large streamwise wavelengths. This energy results from the background spanwise velocity inducing streamwise velocity around texture elements, which is not accounted for in equations (4.2–4.3). This effect can be modelled in the decomposition,

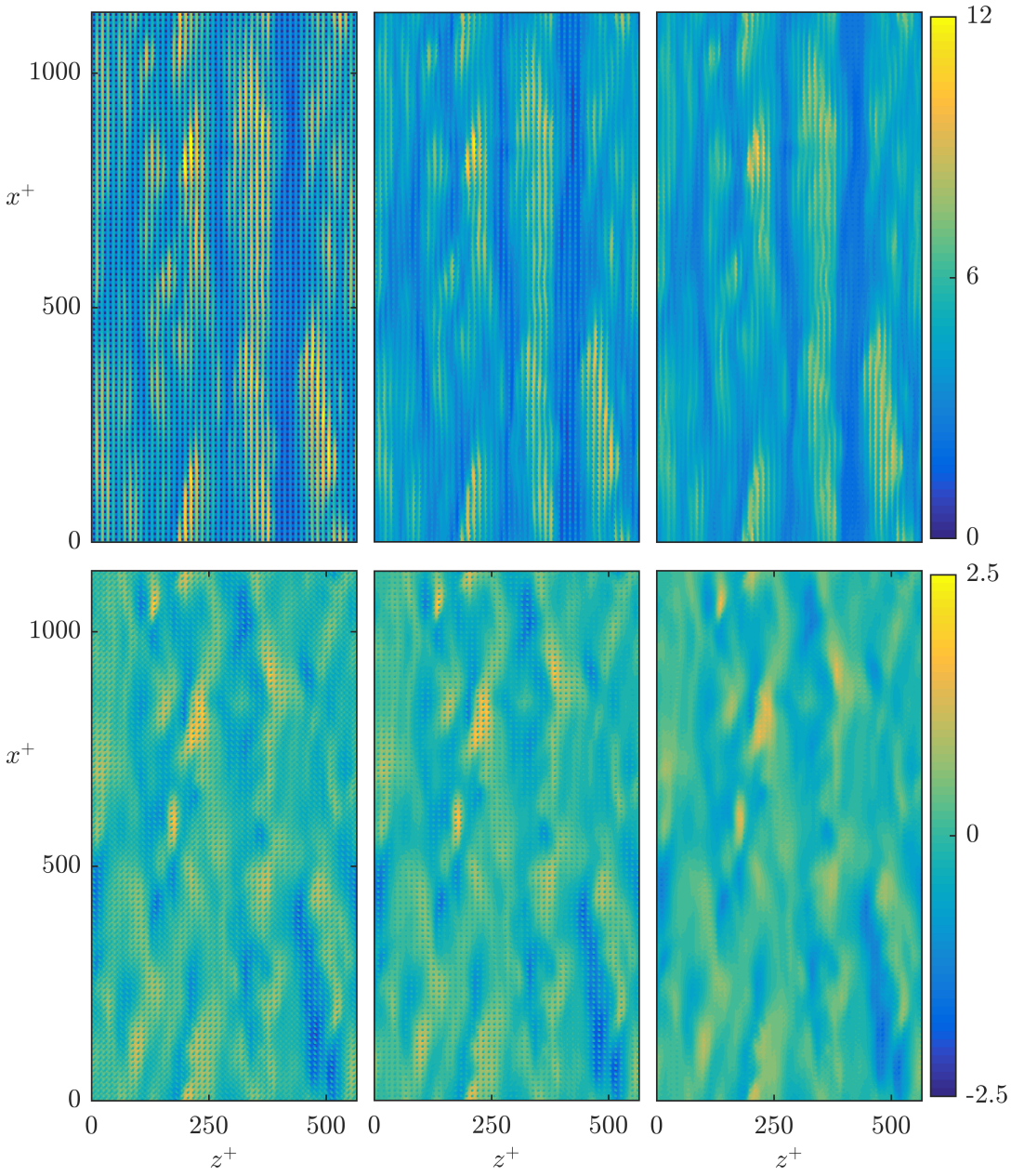

Figure 4.12 – Streamwise (top) and spanwise (bottom) instantaneous velocity snapshots, in wall units, for the full velocity field (left), the turbulent component obtained from the conventional triple decomposition (middle) and the turbulent component obtained from the modulated triple decomposition (right) at the surface for the case with $L^+ \approx 12$.

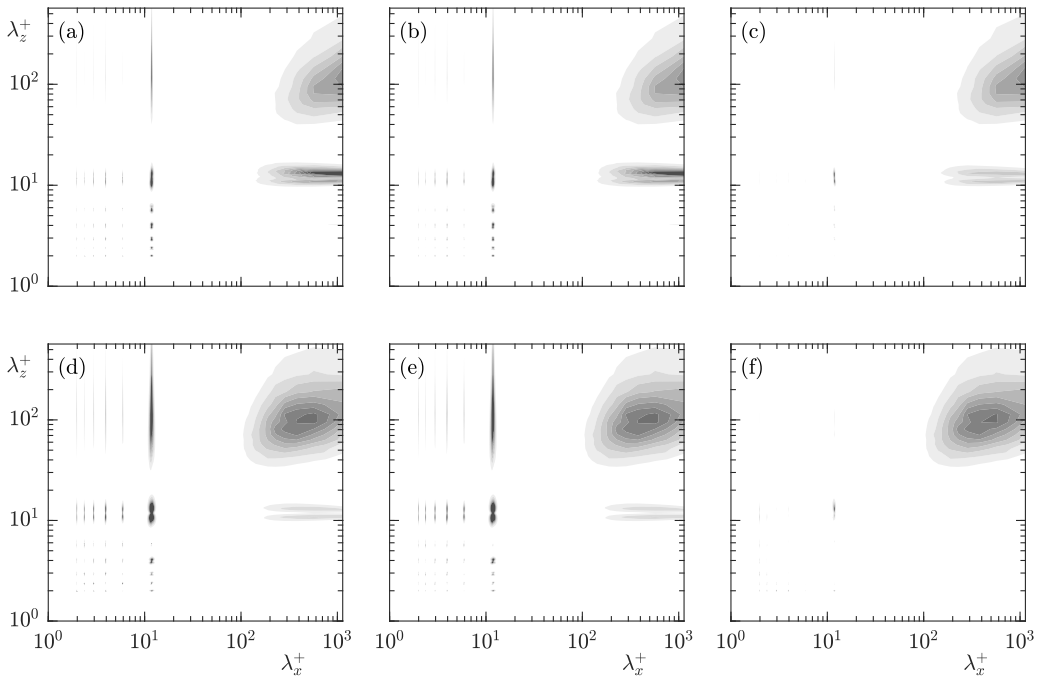

Figure 4.13 – Premultiplied energy spectra at the surface for the streamwise (top) and spanwise (bottom) velocities for the case with $L^+ \approx 12$. (a,d) full velocity fields; (b,e) turbulent components obtained from the conventional triple decomposition; (c,f) turbulent components obtained from the modulated triple decomposition.

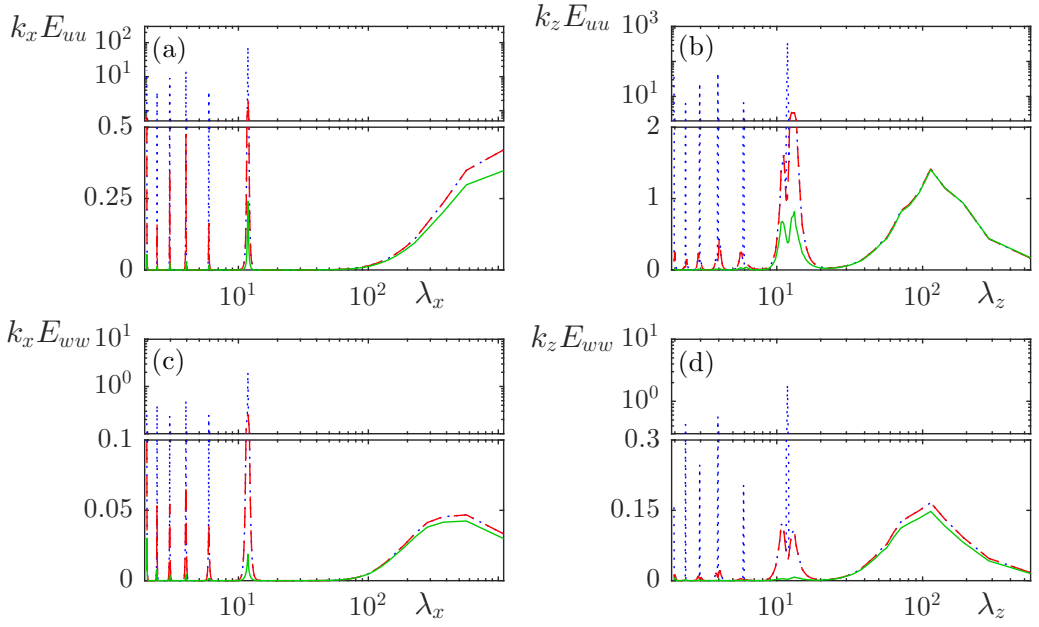

Figure 4.14 – One-dimensional premultiplied energy spectra at the surface of the streamwise (top) and spanwise (bottom) velocities for the case with $L^+ \approx 12$. ·····, full signal; – –, turbulent component obtained from triple decomposition; ——, turbulent component obtained from modulated triple decomposition.

if the texture size is small, by assuming that the local overlying turbulence acts as a homogeneous transverse shear over texture elements, generating a corresponding coherent flow, in a similar manner to the spanwise velocity decomposition in equation (4.3). Additionally, the large variation in intensity of the overlying flow, demonstrated in figure 4.12, modifies the texture-coherent flow field. It is assumed in equation (4.2) that the texture-coherent flow fields are the same for each texture element, just modulated in intensity. However, the variation in local intensity, for this $L^+ \approx 12$ texture, varies the Reynolds number of a texture element, Re_{tx}, by an order of magnitude from $\mathrm{Re}_{tx} \sim \mathcal{O}(10)$ to $\mathrm{Re}_{tx} \sim \mathcal{O}(100)$, which, due to advective effects, modifies the texture-coherent flow-fields between different texture elements. This effect can, however, be modelled in the decomposition by varying the texture-coherent flow field depending on the local intensity.

Including both of these effects, the decomposition for the streamwise and spanwise velocities become

$$\begin{aligned} u(x,y,z,t) \approx U(y) + \widetilde{u}_u(\widetilde{x},y,\widetilde{z},\overline{\widetilde{u}}) \left(\frac{U(y)+u_T(x,y,z,t)}{U(y)}\right) \\ +\widetilde{u}^*_w(\widetilde{x},y,\widetilde{z}^*) \left(\frac{w_T(x,y,z,t)}{\overline{w}^*(y)}\right) + u_T(x,y,z,t), \end{aligned} \tag{4.4}$$

$$\begin{aligned} w(x,y,z,t) \approx \widetilde{w}_u(\widetilde{x},y,\widetilde{z},\overline{\widetilde{u}}) \left(\frac{U(y)+u_T(x,y,z,t)}{U(y)}\right) + \widetilde{w}^*_w(\widetilde{x},y,\widetilde{z}^*) \left(\frac{w_T(x,y,z,t)}{\overline{w}^*(y)}\right) \\ + w_T(x,y,z,t), \end{aligned} \tag{4.5}$$

where $\overline{\widetilde{u}}$ is the local texture-averaged streamwise velocity. For the case with $L^+ \approx 12$, this reduces the remaining energy in the background turbulent component, as can be seen from the velocity fields in figure 4.15 and the energy spectra in figures 4.16 and 4.17. However, for larger texture sizes, $L^+ \gtrsim 18$, the surface texture becomes larger than the near-wall vortices (Blackwelder & Eckelmann, 1979). The assumption that individual texture elements simply perceive an overlying homogeneous spanwise shear starts to fail. In these cases, inclusion of these terms in the decomposition for the streamwise velocity results in spurious noise in the obtained background turbulent fields, u_T. While the modified decomposition is generally effective at filtering out the texture-induced flow from u_T for the case shown with $L^+ \approx 12$, spurious noise is visible in localised regions in the velocity fields in figure 4.15. For consistency, these additional terms are neglected for all cases, but this does not affect the results in the subsequent analysis. The assumption of unidirectional flow over texture elements is

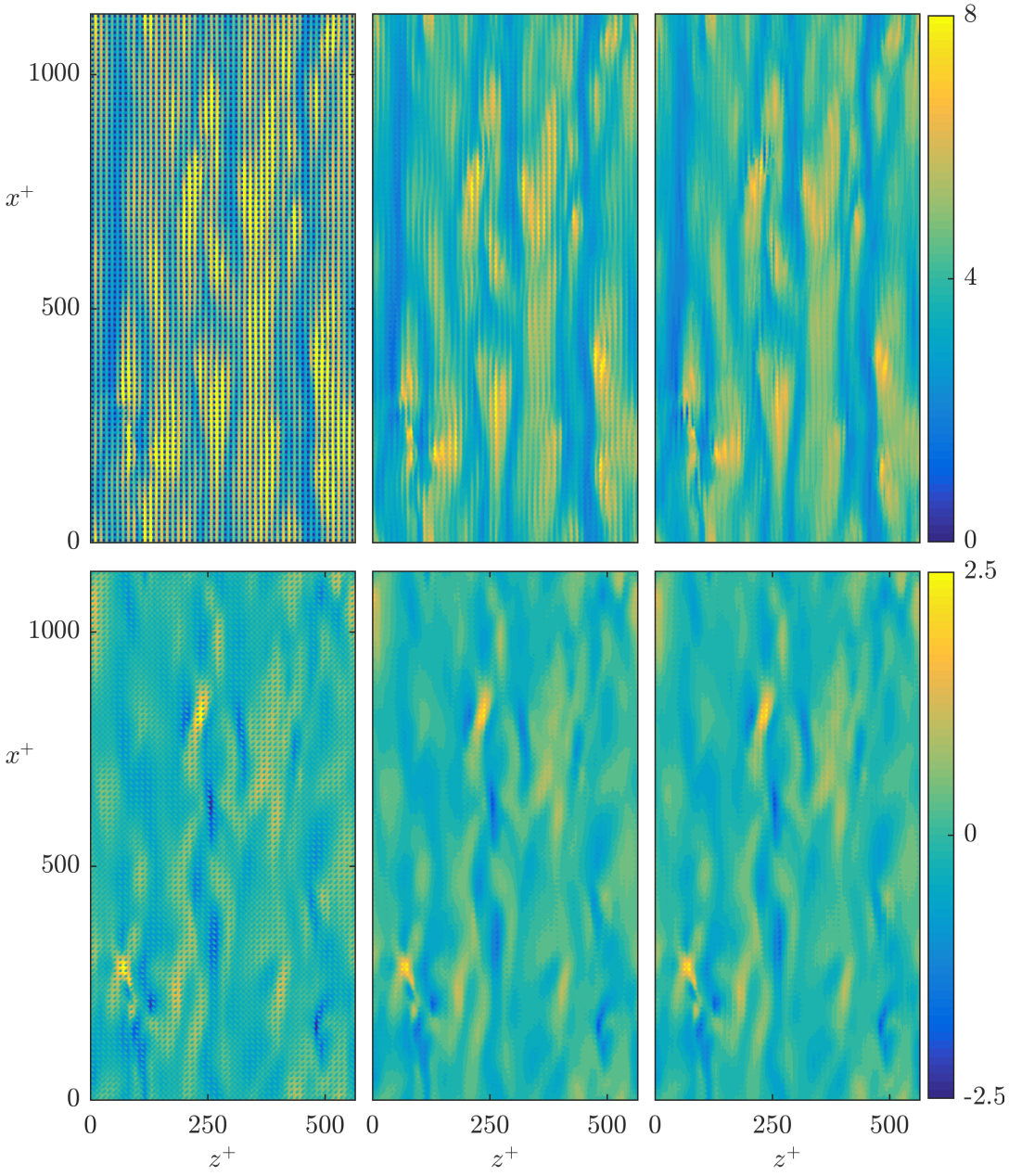

Figure 4.15 – Streamwise and spanwise instantaneous velocity snapshots, in wall units, for the full velocity field (left), the turbulent component obtained from equations (4.2–4.3) (middle) and the turbulent component obtained from equations (4.4–4.5) (right) at the surface for the case with $L^+ \approx 12$.

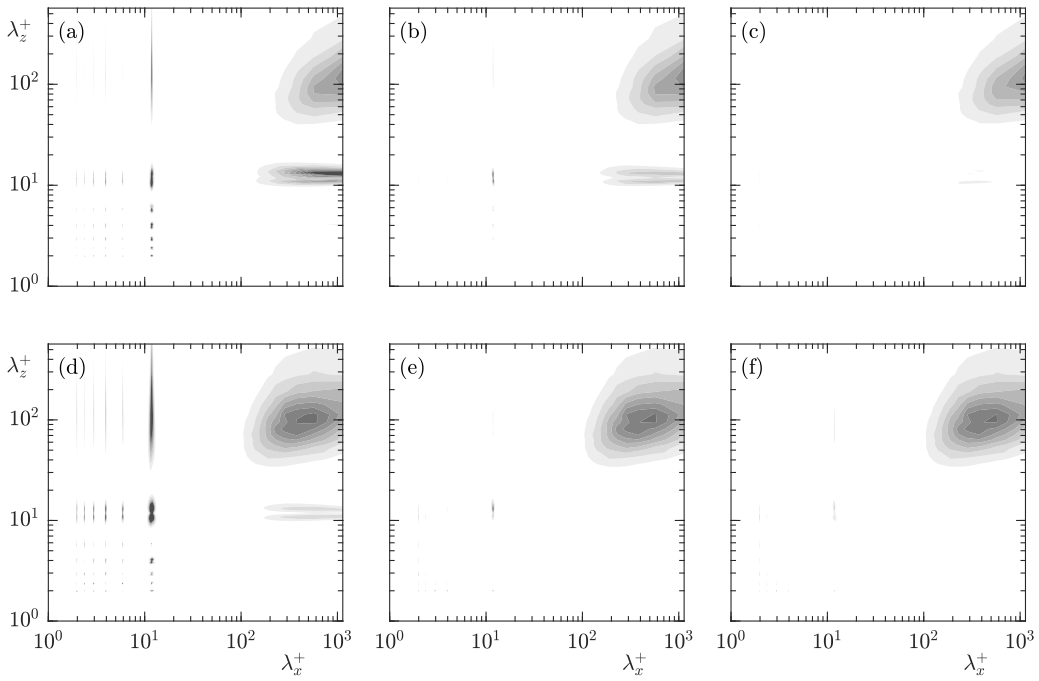

Figure 4.16 – Premultiplied energy spectra at the surface for the streamwise (top) and spanwise (bottom) velocities for the case $L^+ \approx 12$. (a,d) full velocity fields; (b,e) turbulent component obtained from equations (4.2–4.3); (c,f) turbulent component obtained from equations (4.4–4.5).

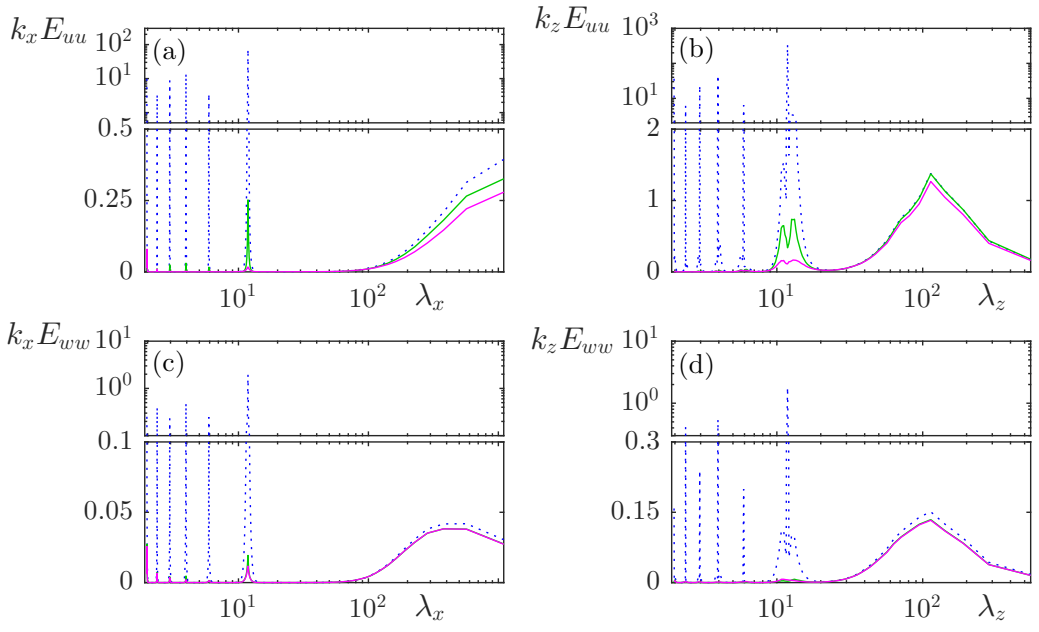

Figure 4.17 – One-dimensional premultiplied energy spectra at the surface of the streamwise (top) and spanwise (bottom) velocities for the case with $L^+ \approx 12$. ·····, full signal; ——, turbulent component obtained from equation (4.2–4.3); ——, turbulent component obtained from equations (4.4–4.5).

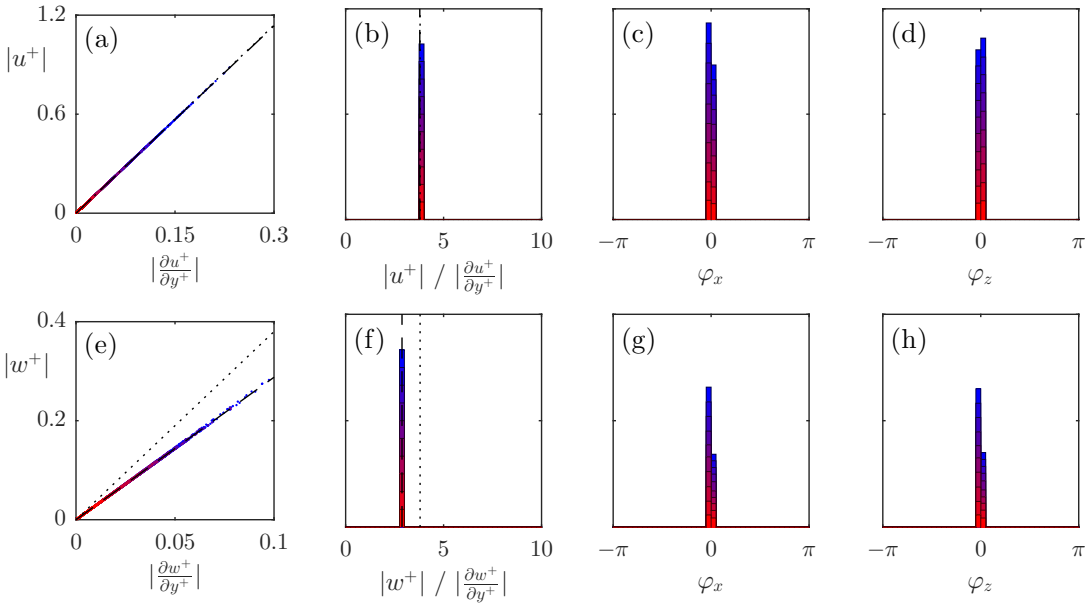

Figure 4.18 – Instantaneous streamwise (top) and spanwise (bottom) slip lengths of wavelengths $\lambda_x^+ \approx 113 - 1131$ and $\lambda_z^+ \approx 113 - 565$ (coloured from red to blue for increasing streamwise wavelength) for the case with $L^+ \approx 12$ obtained from the turbulent components of the velocity fields. (a,e) instantaneous correlation of velocity and shear magnitudes; (b,f) probability density histogram of the slip length; streamwise (c,g) and spanwise (d,h) phase difference between velocity and shear. In (a,b,e,f) the dashed line indicates the fitted dynamic slip length, obtained from a linear regression of the data points, and the dotted line indicates the mean slip length.

also present in the spanwise velocity decomposition. The results in section 4.4 will show that as the texture size is increased, this assumption starts to fail, but in these cases inclusion of this term is still more effective at isolating the background turbulent flow than neglecting it.

4.4 Reassessment of the homogeneity of the slip length

Now that the background, turbulent flow has been isolated from the velocity fields, the apparent slip length experienced by the turbulent lengthscales in the overlying flow can be reassessed.

Figures 4.18 and 4.19 show the slip length correlations using the data obtained from the background, turbulent components for the cases with $L^+ \approx 12$ and 47. These correlations essentially shows a collapse to a line of uniform slip length and zero phase, recovering the correlation between velocity and shear. This confirms that the

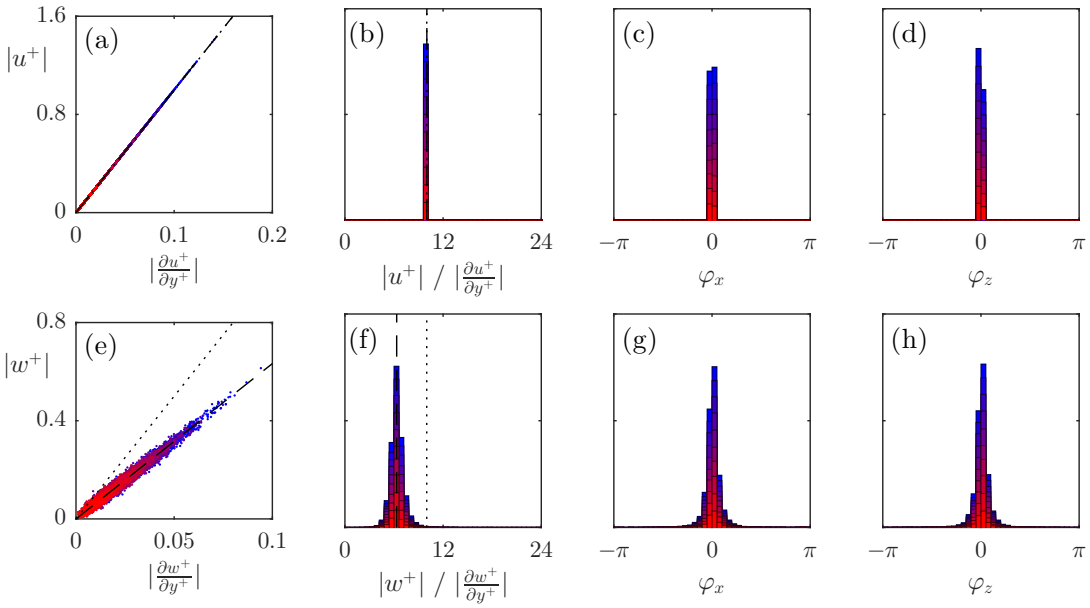

Figure 4.19 – Instantaneous streamwise (top) and spanwise (bottom) slip lengths of wavelengths $\lambda_x^+ \approx 113 - 1131$ and $\lambda_z^+ \approx 113 - 565$ (coloured from red to blue for increasing streamwise wavelength) for the case with $L^+ \approx 47$ obtained from the turbulent components of the velocity fields. (a,e) instantaneous correlation of velocity and shear magnitudes; (b,f) probability density histogram of the slip length; streamwise (c,g) and spanwise (d,h) phase difference between velocity and shear. In (a,b,e,f) the dashed line indicates the fitted dynamic slip length, obtained from a linear regression of the data points, and the dotted line indicates the mean slip length.

loss of correlation of the slip length previously observed is a result of contamination by the texture-induced flow. The recovery of correlation of the slip length can be interpreted as the overlying, background turbulence being subject to a homogeneous boundary condition. Further to this, the streamwise dynamic slip length, i.e., the slip length experienced by the velocity fluctuations, recovers the value of the mean slip length, in contrast to the smaller value obtained from the full velocity fields. The previously observed reduction in value, therefore, also appears to be a result of contamination by the texture-induced flow. The spanwise fluctuations, however, still appear to experience a slip length that is smaller than the mean streamwise slip length, despite the isotropy of the texture.

Figure 4.20 shows spectral maps of the variation of the dynamic slip length for the background, turbulent component. These confirm that a homogeneous slip length is recovered across all energetically relevant lengthscales. The streamwise spectral maps show slip lengths that are homogeneous across all scales, for all texture sizes, with

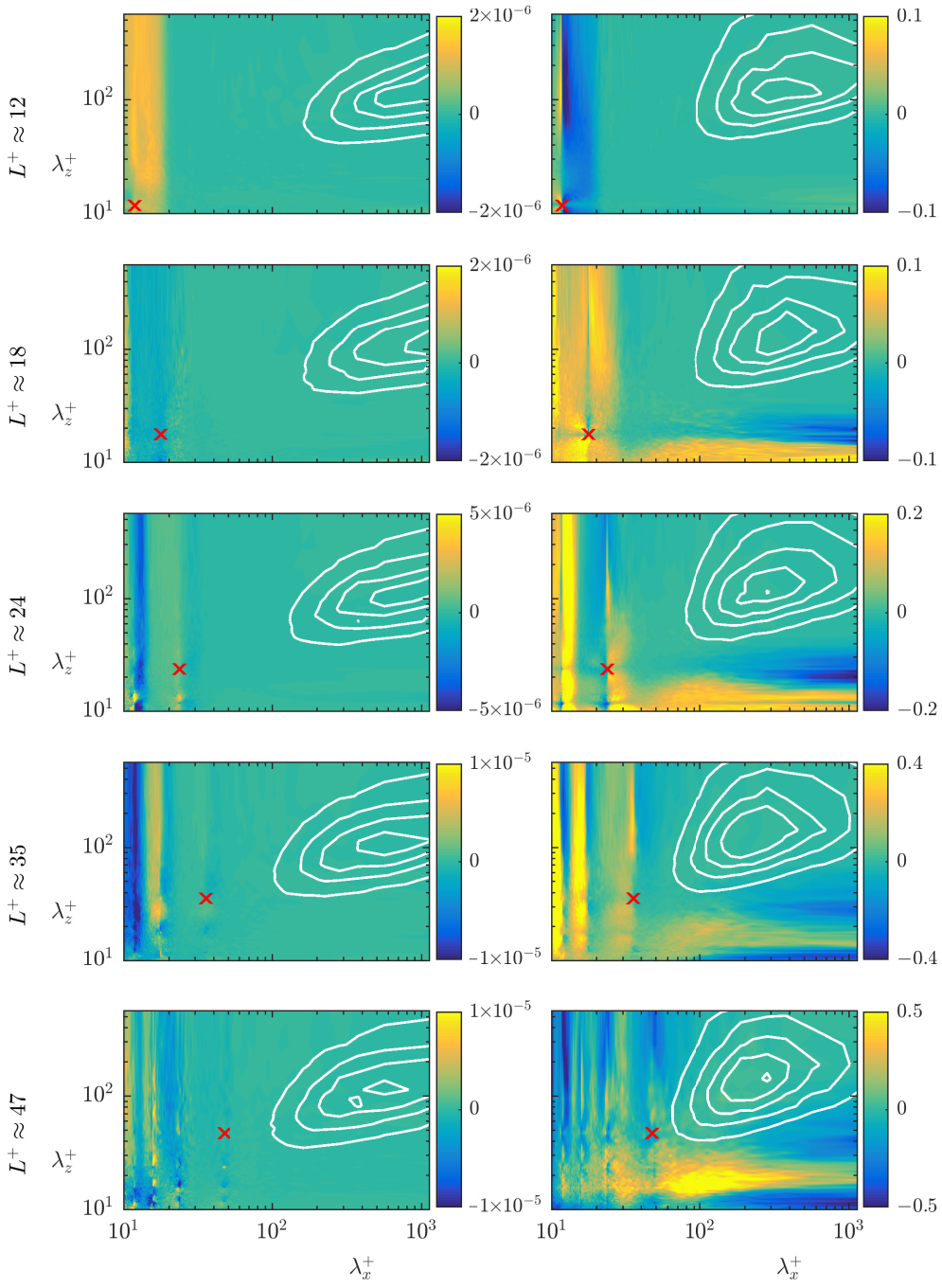

Figure 4.20 – Spectral maps of the variation of the time-averaged slip length, $\left(\ell^+_{x/z} - \left\langle \ell^+_{x/z} \right\rangle\right) / \left\langle \ell^+_{x/z} \right\rangle$, where $\left\langle \ell^+_{x/z} \right\rangle$ is the mean dynamic slip length over the range $\lambda_x^+ \approx 113 - 1131$ and $\lambda_z^+ \approx 113 - 565$, obtained from the turbulent components of the velocity fields (filled contours) for the streamwise (left) and spanwise (right) directions, with cases $L^+ \approx 12$ to 47 shown from top to bottom. Spectral energy density of the corresponding velocity at a height $y^+ = 15$ (lined contours). The red cross indicates the wavelength of the texture.

values matching the slip length experienced by the mean flow. All lengthscales in the flow, therefore, experience the same streamwise slip length as the mean flow. For the spanwise slip length, for all texture sizes, and across all energetically relevant scales, the slip length is also homogeneous. As the texture size is increased, however, scales of the order of the texture size and smaller show a deviation from the slip length experienced by larger wavelengths. This apparent loss of correlation is likely due to the failure of the decomposition to fully filter the texture-induced flow. As discussed in section 4.3, the decomposition assumes that the flow remains unidirectional over individual texture elements. While for small texture sizes, $L^+ \lesssim 18$, this assumption is reasonable, for larger texture sizes, $L^+ \gtrsim 18$, the surface texture becomes larger than the near wall vortices (Blackwelder & Eckelmann, 1979), making this assumption questionable. In any event, all relevant lengthscales in the overlying flow perceive the surface as a homogeneous slip length. Consequently, the mismatch in the measured ΔU^+ between simulations that resolve the surface texture, and simulations where equivalent slip lengths are applied (Seo & Mani, 2016), cannot be attributed to the overlying turbulence not perceiving the surface as producing a homogeneous slip effect. There must be an additional phenomenon present than the sole effect of surface slip.

Chapter 5

The effect of surface slip on overlying turbulence

Chapter 4 showed that with textured surfaces the overlying turbulence experiences the surface as a homogeneous slip length. To assess the effect of such boundary conditions on the overlying turbulence, this chapter considers simulations where homogeneous slip lengths are applied. It will be shown that the effect of slip only acts to change the perceived origins of the mean flow and the overlying turbulence. The dynamics in the overlying turbulence are essentially unmodified compared to turbulence over a smooth wall.

Parts of this chapter have been submitted for publication in Fairhall et al. *(2019) and were presented at the 2017 American Physical Society Division of Fluid Dynamics Meeting (Fairhall & García-Mayoral, 2017*b*).*

To investigate how a homogeneous slip-length boundary condition affects the overlying turbulent flow, this chapter considers simulations where the texture-resolved simulations are replaced by equivalent homogeneous slip length boundary conditions. The values of the applied slip lengths are the dynamic slip lengths obtained for each texture size in chapter 4. The slip lengths are applied as Robin boundary conditions of the form

$$u_s = \ell \frac{\partial u}{\partial y}\Big|_s, \tag{5.1}$$

where u_s is the velocity at the surface, $\frac{\partial u}{\partial y}|_s$ is the wall-normal velocity gradient at the surface and ℓ is the slip length. The values of the slip lengths are different for the streamwise and spanwise velocities and are listed in table 5.1 for each texture size. As with the texture-resolved simulations an impermeability condition is applied at the surface for the wall-normal velocity.

In section 1.4, it was shown that the shift of the mean velocity profile, ΔU^+, in simulations where impermeability and homogeneous slip lengths are applied, is given by,

$$\Delta U^+ \approx \ell_x^+ - \ell_{z,eff}^+, \tag{5.2}$$

i.e., the difference between the streamwise slip length, ℓ_x^+, and the effective spanwise slip length, $\ell_{z,eff}^+$, which is given in equation (1.5). This equation for ΔU^+ can be interpreted such that the effective spanwise slip length, $\ell_{z,eff}^+$, is the distance below the surface where the overlying turbulence perceives a wall. The flow is, therefore, described by two virtual origins as is the case with riblets (Luchini *et al.*, 1991), the virtual origin of the mean-flow, ℓ_x^+, and the virtual origin perceived by the overlying turbulent flow, which will be referred to as ℓ_T^+. For the surfaces considered here, $\ell_T^+ \approx \ell_{z,eff}^+$, the empirical relation in equation (1.5). For the more general case, in which the impermeability condition is relaxed, the turbulent virtual origin deviates from the relation for $\ell_{z,eff}^+$ (Gómez-de-Segura *et al.*, 2018).

As the turbulent flow perceives a wall at a distance ℓ_T^+ below the surface, the scaling for the problem is based from this virtual origin. The effective half-height of the channel, therefore, becomes the distance from the turbulent virtual origin to the channel centre $\delta' = \delta + \ell_T$, and the friction velocity, u_τ, is defined at the turbulent virtual origin, $y^+ = -\ell_T^+$. With the driving pressure gradient kept the same as the reference smooth wall, this results in a small change in the friction Reynolds number, or, equivalently, δ'^+.

Case	L^+_{eqiv}	$\mathrm{Re}_{\tau_\delta}$	N_x	N_z	N_y	ℓ^+_x	ℓ^+_z	ΔU^+
12_{sl}	11.8	180	128	128	153	3.8	2.8	2.1
18_{sl}	17.8	180	128	128	153	5.9	4.0	3.8
24_{sl}	23.7	180	128	128	153	7.0	4.4	4.8
35_{sl}	35.6	180	128	128	153	8.6	5.1	6.2
47_{sl}	47.4	180	128	128	153	10.1	6.3	7.5

Table 5.1 – Parameters for the homogeneous slip-length simulations. L^+_{eqiv} is the texture size for which the applied slip lengths are equivalent to, $\mathrm{Re}_{\tau_\delta}$ is the friction Reynolds number, N_x and N_z are the number of grid points in the streamwise and spanwise directions, N_y is the number of grid points in the wall-normal direction, ℓ^+_x and ℓ^+_z are the applied streamwise and spanwise slip lengths, and ΔU^+ is the measured shift of the logarithmic region of the mean velocity profile.

To compare the result of scaling with this u_τ and the conventional scaling with the origin at $y^+ = 0$, the mean velocity profiles with the slip velocity subtracted and the rms fluctuations of the velocities, the Reynolds stress, $\overline{u'v'}^+$, and the rms of the streamwise vorticity fluctuations are shown in figure 5.1. The rms of streamwise vorticity is an indicator of the strength and y-location of quasi-streamwise vortices. The panels on the left of figure 5.1 normalise these profiles by the friction velocity obtained at $y^+ = 0$. Compared to the smooth wall profiles, these fluctuations show an apparent shift of the location of the peaks closer to the surface, as previously reported (Min & Kim, 2004; Busse & Sandham, 2012), as well as a slight increase in the magnitudes of the peaks for increasing slip. The panels in the middle show these fluctuations after rescaling by the friction velocity at the turbulent virtual origin, $y^+ = -\ell^+_T$, and shifting the profiles in y^+ by ℓ^+_T, so that the origin is at $y^+ = -\ell^+_T$. Defined in this way, the profiles show a close collapse to the smooth wall profiles. This supports the idea that turbulence perceives a virtual origin at $y^+ = -\ell^+_T$, and is otherwise essentially unmodified. There are slight differences to the rms profiles very close to the surface, most noticeably for the streamwise velocity fluctuations. While the overlying turbulence perceives an origin at $y^+ = -\ell^+_T$, the streamwise and spanwise velocities would vanish at $y^+ = -\ell^+_x$ and $y^+ = -\ell^+_z$, which are both deeper into the surface than $y^+ = -\ell^+_T$. This modifies the gradient of the rms fluctuations very close to the surface. The effect is particularly intense for the streamwise velocity, which has the deepest virtual origin, and even results in a small increase in the value of the peak rms.

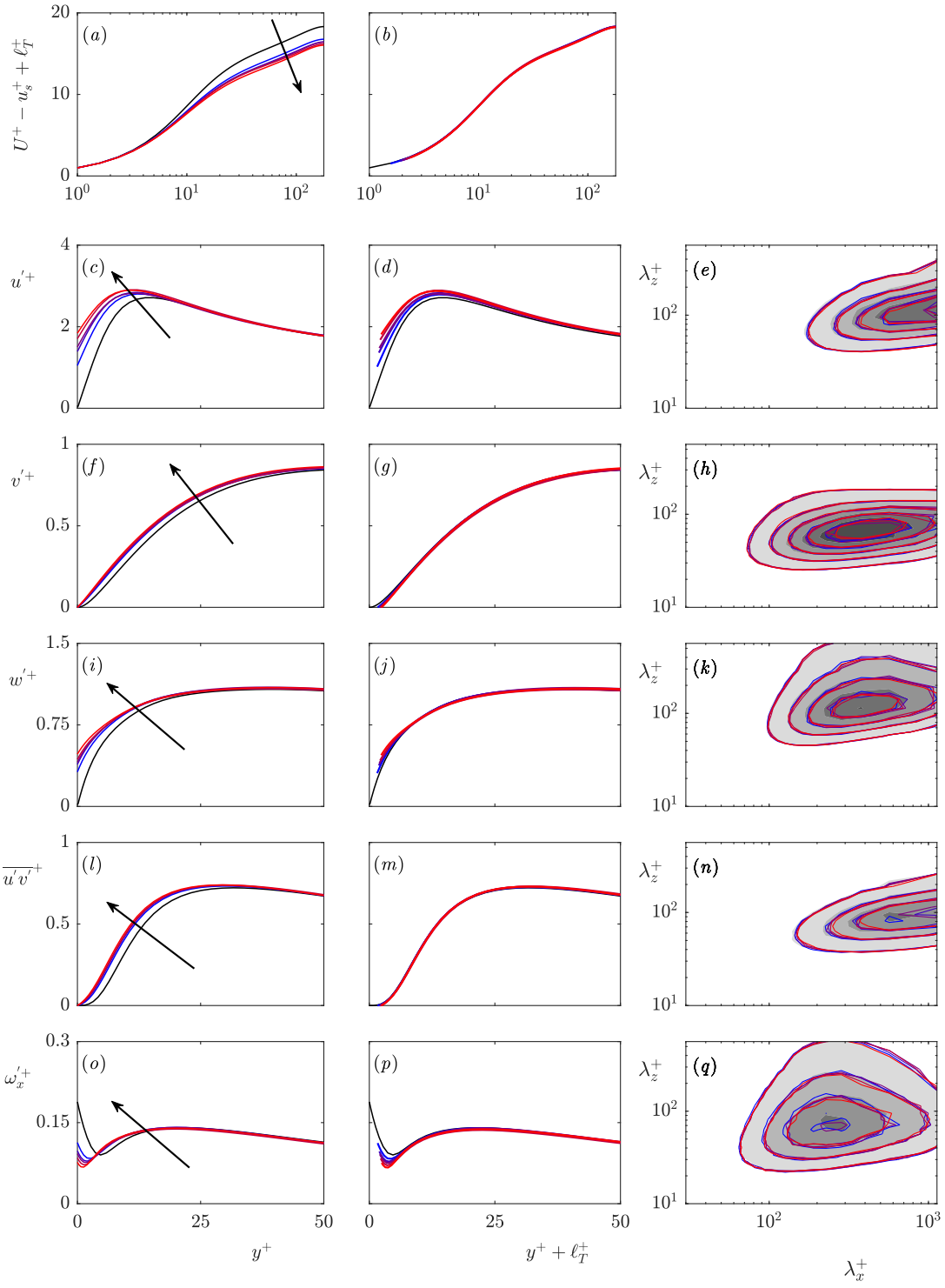

Figure 5.1 – Turbulent statistics for the homogeneous slip-length simulations scaled by the friction velocity at the surface (left), rescaled by the friction velocity based at the turbulent virtual origin and shifted by the turbulent virtual origin, ℓ_T^+ (centre). Smooth wall (——); increasing equivalent texture size $L^+ \approx 12$ to 47 (—— from blue to red). Spectral energy densities at $y^+ + \ell_T^+ = 15$ (right), smooth wall (filled contour); increasing equivalent texture size (—— from blue to red).

Premultiplied energy spectra for the three velocities, Reynolds stress, $\overline{u'v'}^+$, and streamwise vorticity are also shown in figure 5.1, at a height of 15 wall units above the turbulent virtual origin ℓ_T^+. These spectra also show a collapse to the smooth wall data. The slip boundary conditions do not alter the turbulent dynamics in the overlying flow, which remain smooth-wall-like except for the shift of the origin.

Chapter 6

The effect of surface texture on overlying turbulence

It was shown in chapter 4 that the overlying turbulence experiences the surface as a slip-length boundary condition. However, previous research has shown that the ΔU^+, and, therefore, the drag reduction, predicted using homogeneous slip-length models disagrees with that obtained from textured surfaces when the texture size is sufficiently large. This chapter, therefore, focuses on how textured surfaces modify the overlying turbulence beyond the effect of slip at the surface. It will be shown that up to texture sizes $L^+ \lesssim 18$, the predominant effect of the surface is the direct effect of the surface slip. The texturing of the surface has negligible impact on the overlying turbulence, and the surface can, therefore, be modelled using homogeneous slip lengths. However, beyond this size the coherent flow generated by the texture interacts with the overlying turbulence, modifying its dynamics to increase the drag.

Parts of this chapter have been submitted for publication in Fairhall et al. *(2019) and were presented at the 2017 American Physical Society Division of Fluid Dynamics Meeting (Fairhall & García-Mayoral, 2017*b*).*

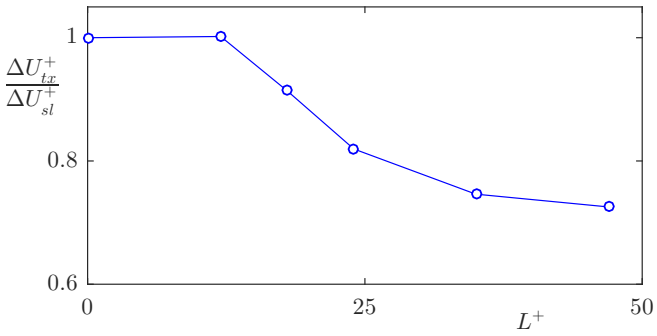

Figure 6.1 – Ratio of the measured ΔU^+ between the texture-resolved simulations and the homogeneous slip-length simulations.

It has previously been observed that the ΔU^+ obtained from texture-resolving simulations differs from that obtained from homogeneous slip-length simulations when the texture size becomes sufficiently large (Seo & Mani, 2016). The ratio of ΔU^+ between the texture-resolving simulations and the equivalent homogeneous slip-length simulations for the cases in this thesis shows this in figure 6.1. The results of chapter 4, however, showed that for texture-resolving simulations, the overlying turbulent flow still experiences a homogeneous slip-length boundary condition. The effect of texture does not modify the boundary condition experienced by the overlying turbulence. This additional downward shift of the mean velocity profile must, therefore, be the result of a further interaction of the texture with the overlying turbulence. To investigate the discrepancy in ΔU^+ for larger texture sizes, in this section, the results of the texture-resolving simulations are now compared to the homogeneous slip-length simulations. It is assumed that the effect of slip in the texture-resolved cases is the same as in the homogeneous slip cases from chapter 5. Consequently, the virtual origin of the turbulent flow, ℓ_T^+, is the same as the virtual origin of the homogeneous slip-length simulations and any further changes to the flow are, therefore, an additional consequence of the texture.

First, the cases where ΔU^+ from the textured simulations is comparable to the slip length simulations will be analysed. The mean velocity profile and rms fluctuations of the velocities and Reynolds stress, $\overline{u'v'}^+$, for the textured case with $L^+ \approx 18$ are shown in figure 6.2. Also included are the rms fluctuations from the background turbulence, and the profiles from the equivalent homogeneous slip-length simulation. For this texture size, the fluctuations and mean velocity profiles from the textured simulations agree well with the homogeneous slip-length simulations. There is a texture-coherent contribution very close to the surface, but this does not significantly contribute to the drag or modify the background turbulence. The predominant effect of the surface,

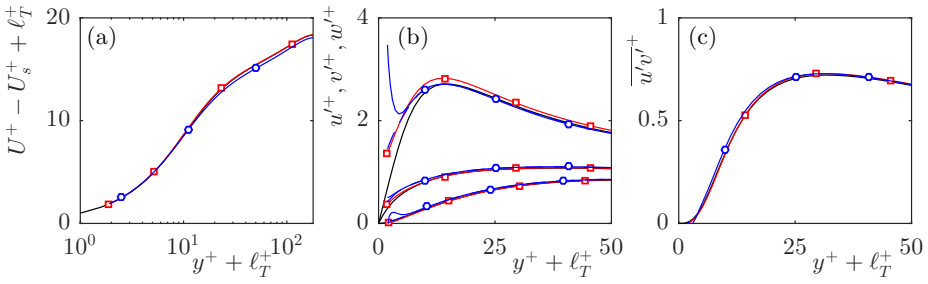

Figure 6.2 – Comparison of mean velocity profiles, velocity fluctuations and Reynolds stress, $\overline{u'v'}^+$, for the texture-resolved and equivalent homogeneous slip-length simulations with smooth channel data for the case with $L^+ \approx 18$. (a) mean velocity profile; (b) rms velocity fluctuations; (c) Reynolds stress, $\overline{u'v'}^+$. ——, smooth channel; –□–, data obtained from the equivalent homogeneous slip-length simulation; –○–, data obtained from the full velocity fields of the textured simulation; – –, data obtained from the turbulent component of the velocity fields of the textured simulation. Note that the origin is located at $y^+ = -\ell_T^+$ with the friction velocity calculated from this origin.

therefore, is the shift due to slip. Premultiplied energy spectra are shown in figure 6.3 at a height 15 wall units above the turbulent virtual origin, where the signature of the texture is already negligible. They show that for $L^+ \lesssim 20$, the spectra of the textured simulations essentially collapse to the spectra from simulations over smooth walls. This further supports the idea that, for textures of this size, the presence of the texture does not modify the dynamics of the overlying flow. The shift ΔU^+ for these texture sizes can, therefore, be predicted using homogeneous slip-length models.

The cause for the discrepancy in ΔU^+ between the homogeneous slip-length and textured simulations for larger texture sizes can be investigated by integrating the streamwise momentum equation (García-Mayoral & Jiménez, 2011; Abderrahaman-Elena *et al.*, 2019). Averaging the streamwise momentum equation in time and in the streamwise and spanwise directions, and integrating in the wall-normal direction gives

$$\nu \frac{\partial U}{\partial y} + \tau_{uv} = u_\tau^2 \frac{\delta' - y}{\delta'}, \tag{6.1}$$

where τ_{uv} is the Reynolds stress, $\overline{u'v'}^+$, U is the mean velocity and $\delta' = \delta + \ell_T$ is the effective channel half-height. Integrating this equation again in the wall-normal direction from the surface to an arbitrary height within the logarithmic region, H^+, gives.

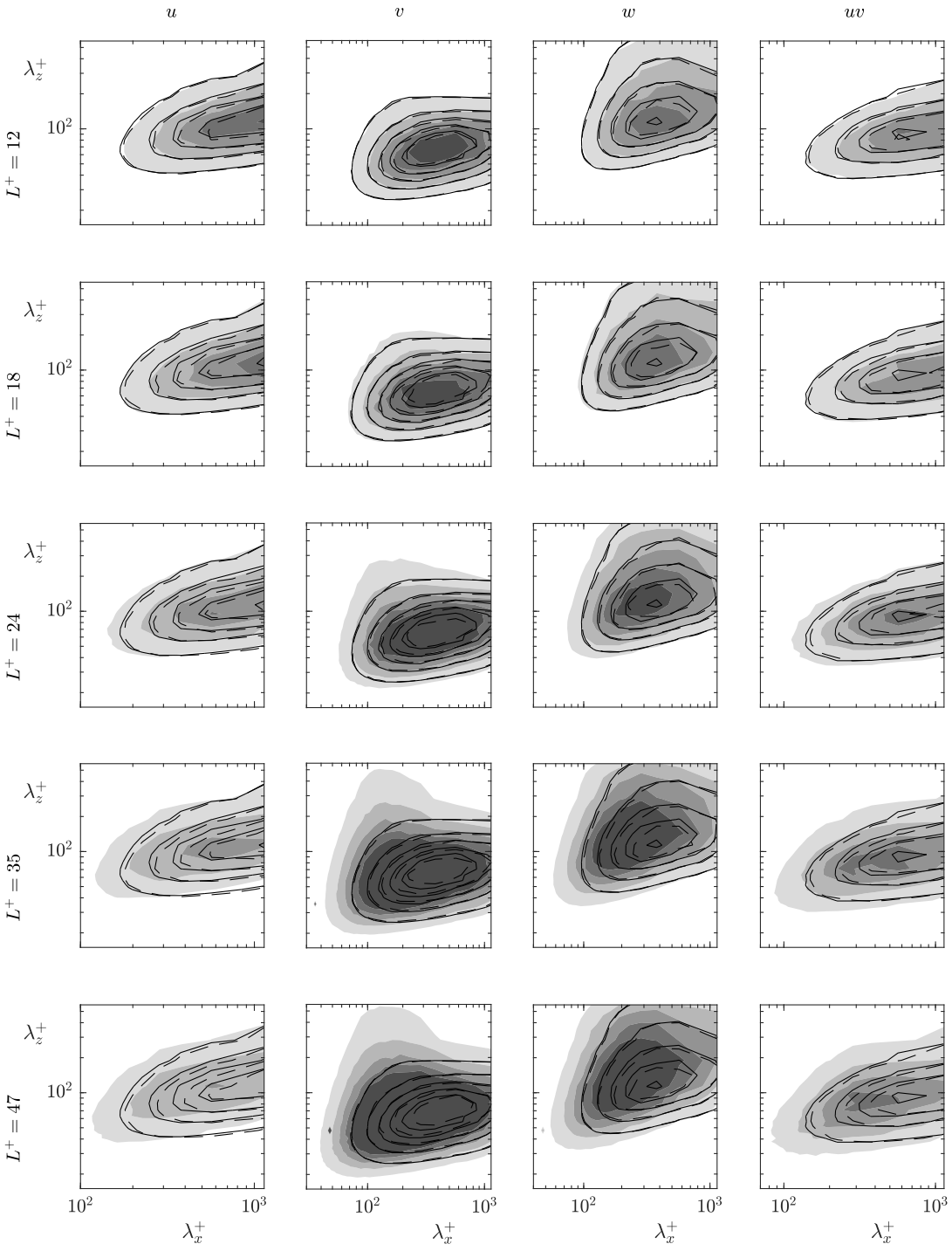

Figure 6.3 – Spectral energy densities of the three velocities and Reynolds stress, $\overline{u'v'}^+$, for the cases with $L^+ \approx 12$ to 47 at a height of 15 wall units above the turbulent virtual origin. Textured simulations (filled contours); smooth wall (solid lines); homogeneous slip-length simulations (dashed lines).

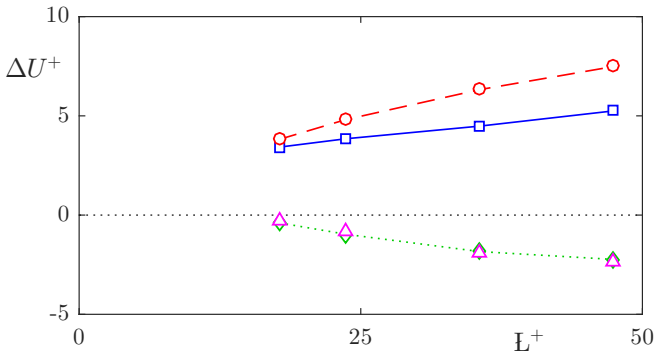

Figure 6.4 – Comparison of the measured ΔU^+ of the texture-resolved simulations with the homogeneous slip-length simulations. –□–, ΔU^+ of texture-resolved simulations; – ○ –, ΔU^+ of homogeneous slip-length simulations; ···◇···, difference in ΔU^+ between texture-resolved and homogeneous slip-length simulations; △, integral of the change in Reynolds stress between channels, T_1, from equation (6.3).

$$\int_{\ell_T^+}^{H^+} \tau_{uv}^+ dy^+ + U^+(H^+) - U^+(\ell_T^+) = H^+ - \ell_T^+ - \frac{1}{2}\frac{(H^+)^2 - {\ell_T^+}^2}{\delta^+ + \ell_T^+}. \tag{6.2}$$

Note that for a channel with slip, H^+ is the height above the turbulent virtual origin. This equation is valid for both a superhydrophobic channel and a smooth channel. An expression for ΔU^+ of a superhydrophobic surface can be obtained subtracting the respective equation (6.1) of the superhydrophobic channel from the smooth channel equation. Assuming that the channels have the same δ'^+ then,

$$\Delta U^+ = U^+_{\mathrm{SHS}}(H^+) - U^+_{\mathrm{SC}}(H^+) = U^+_{\mathrm{SHS}}(\ell_T^+) - U^+_{\mathrm{SC}}(\ell_T^+) \underbrace{- \int_{\ell_T^+}^{H^+} (\tau^+_{uv,\mathrm{SHS}} - \tau^+_{uv,\mathrm{SC}}) dy^+}_{T_1}, \tag{6.3}$$

where ℓ_T^+ is the turbulent virtual origin of the slipping channel and T_1 is the change in Reynolds stress integral between the two channels. Here, $U^+_{SHS}(\ell_T^+) \approx \ell_x^+$ is the slip velocity at the surface of the superhydrophobic channel and $U^+_{SC}(\ell_T^+) \approx \ell_T^+$, assuming that ℓ_T^+ is within the viscous sublayer, i.e. $\ell_T^+ \lesssim 5$.

For cases where the superhydrophobic surface is represented using slip lengths then, as shown in figure 5.1 of chapter 5, the only effect of the slipping surface on the Reynolds stress is a change of perceived origin. It, therefore, follows the term T_1 is zero. This reduces equation (6.3) to,

$$\Delta U^+ \approx \ell_x^+ - \ell_T^+. \tag{6.4}$$

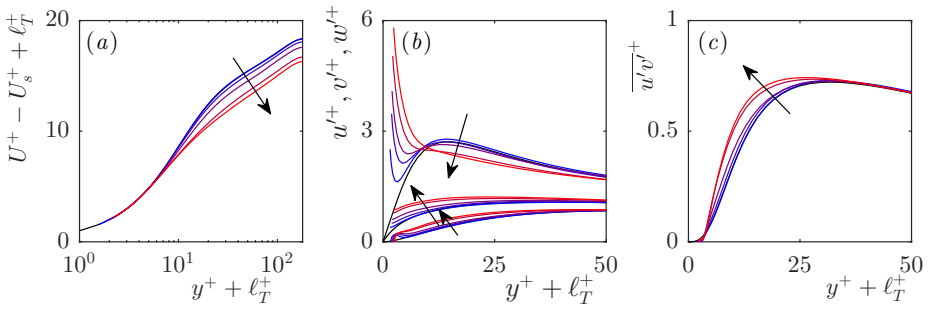

Figure 6.5 – Comparison of the mean velocity profile, rms velocity fluctuations and Reynolds stress, $\overline{u'v'}^+$, for the texture-resolved simulations with $L^+ \approx 12$ to 47 to smooth channel data. (a) mean velocity profile; (b) rms velocity fluctuations; (c) Reynolds stress, $\overline{u'v'}^+$. ——, smooth channel; —— (from blue to red), increasing texture size from $L^+ \approx 12$ to 47. Note that the origin is located at $y^+ = -\ell_T^+$ with the friction velocity calculated from this origin.

The same relation as proposed in equation (1.6).

For textured-resolved channels ΔU^+ is given by the same expression in equation (6.3). As ℓ_x^+ and ℓ_T^+ are the same as the equivalent homogeneous slip length simulation this means that

$$\Delta U^+ \approx \ell_x^+ - \ell_T^+ - \int_{\ell_T^+}^{H^+} (\tau_{uv,\mathrm{SHS}}^+ - \tau_{uv,\mathrm{SC}}^+) dy^+. \tag{6.5}$$

This indicates that it is an increase in Reynolds stress, $\overline{u'v'}^+$, beyond the effect of slip, that causes the additional downward shift of the mean velocity profile in the textured simulations. This is supported by figure 6.4, which shows that the measured difference in ΔU^+ between the texture-resolving and slip-length simulations essentially equals the integral of the change in Reynolds stress between channels. The contribution of the texture-coherent component to the Reynolds stress, $\overline{u'v'}^+$, is negligible, so the observed difference must be essentially caused by modifications in the background turbulence. The Reynolds stress profiles for each textured simulation, shown in figure 6.5(c), support this. With increasing texture size, the Reynolds stress profiles show a modified shape compared to the profile of smooth-wall turbulence, with an increase in Reynolds stress for $5 \lesssim y^+ \lesssim 25$. It should be noted that due to the imposed impermeability, the Reynolds stress must be zero at the surface.

Also shown in figure 6.5 are the mean velocity profiles and rms fluctuations of the velocities. The full rms fluctuations are additionally compared with those from the background turbulence, and with those for the equivalent homogeneous slip simulations for the cases with $L^+ \approx 24$ and 47, in figure 6.6. Beyond $L^+ \gtrsim 24$, the near wall

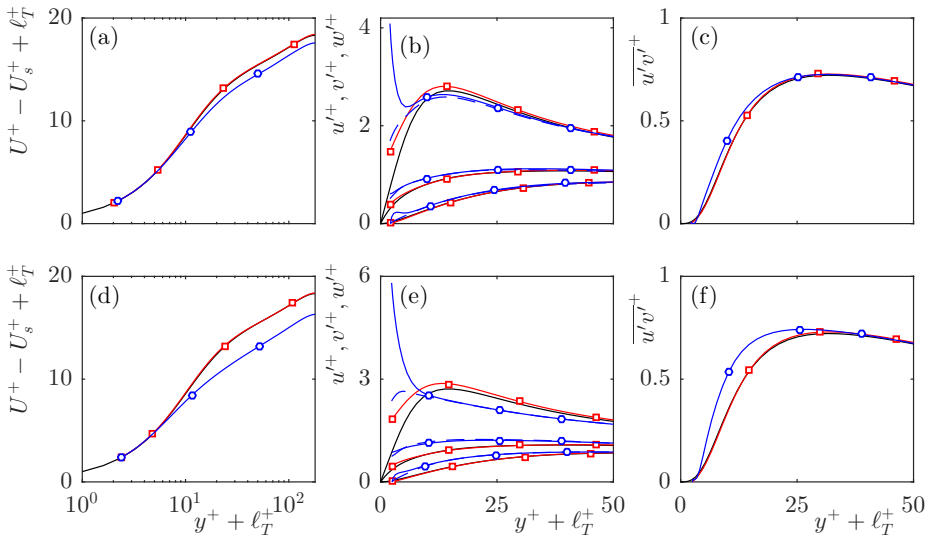

Figure 6.6 – Comparison of mean velocity profiles, velocity fluctuations and Reynolds stress, $\overline{u'v'}^+$, for the texture-resolved and equivalent homogeneous slip-length simulations with smooth channel data for the cases with (a–c) $L^+ \approx 24$ and (d–f) $L^+ \approx 47$. (a,d) mean velocity profile; (b,e) rms velocity fluctuations; (c,f) Reynolds stress, $\overline{u'v'}^+$. ——, smooth channel; –□–, data obtained from the equivalent homogeneous slip-length simulations; –○–, data obtained from the full velocity fields of the textured simulations; – –, data obtained from the turbulent component of the velocity fields of the textured simulations. Note that the origin is located at $y^+ = -\ell_T^+$ with the friction velocity calculated from this origin.

peak of the streamwise fluctuations is reduced compared to the peak observed over smooth walls, with the wall-normal and spanwise fluctuations, by contrast, showing an increase in magnitude. These differences persist up to $y^+ \sim 50$ and have previously been reported in flows over superhydrophobic surfaces (Seo *et al.*, 2015), as well as over rough surfaces (Antonia & Krogstad, 2001; Orlandi & Leonardi, 2006). The premultiplied energy spectra of figure 6.3 show that beyond $L^+ \gtrsim 24$, there is an increase of energy in shorter streamwise lengthscales, and a decrease of energy in longer streamwise lengthscales, compared to smooth-wall turbulence. The wall-normal velocity also shows an increase of energy in larger spanwise wavelengths. This is also seen over surfaces with roughness (Krogstad & Antonia, 1994; Abderrahaman-Elena *et al.*, 2019). Instantaneous realisations of the fluctuating velocity components over a smooth wall and of the background turbulent component of the case with $L^+ \approx 47$ are shown in figure 6.7 at a height $y^+ + \ell_T^+ = 15$. The latter show a reduction in streamwise coherence for scales of order 1000 wall units, as is also indicated by the

energy spectra. At such a large texture size, the lengthscales and magnitude of the texture-coherent flow become comparable to those of the background turbulence. The spectra and instantaneous flow fields suggest a modification of the near-wall dynamics through the disruption of streaks and quasi-streamwise vortices by the texture-induced flow.

These results suggest that, while the overlying turbulent flow still experiences the surface as a homogeneous-slip-length boundary condition, for sufficiently large textures a non-linear interaction of the texture-induced flow with the overlying turbulence modifies its dynamics. This interaction has an extended y-support and does not occur only at $y^+ = 0$. For the surface texture geometry considered in this work, this non-linear interaction begins to appear for $L^+ \simeq 25$ and becomes significant for $L^+ \gtrsim 30$. This is, therefore, the upper limit where homogeneous slip lengths are valid, at least for the geometry studied here. Different texture geometries would cause different texture-induced flows, which could alter the value of L^+ for the onset of the non-linear interaction.

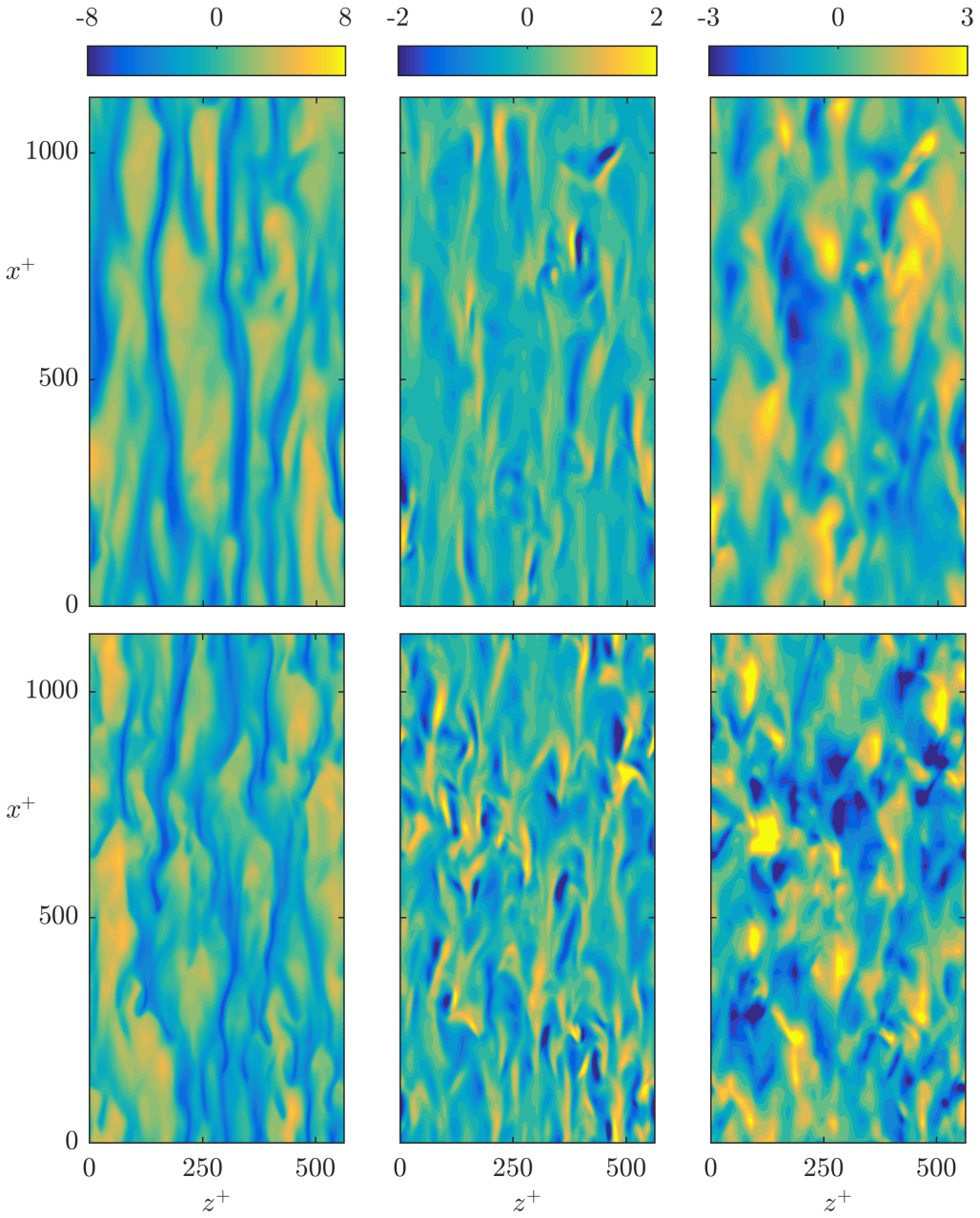

Figure 6.7 – Streamwise (left), wall-normal (middle) and spanwise (right) instantaneous velocity fluctuation flow fields, in wall units, for a smooth wall (top) and the background turbulent components of the velocities for the case with $L^+ \approx 47$ (bottom) at a height $y^+ + \ell_T^+ = 15$.

Chapter 7

Conclusions and outlook

7.1 Conclusions

Superhydrophobic surfaces are able to reduce skin friction drag through the slip they produce at their textured surface. This thesis has analysed the influence that surface slip and surface texture have on overlying turbulent flows, and their respective effects on the surface drag.

The effect that the texture pattern of the surface has on the slip length and the susceptibility of the entrapped gas pockets to deformation was first investigated. It was shown that in the viscous regime, $L^+ \lesssim 1$, surface textures of isolated posts with square, diamond and circular cross-sections, in collocated and staggered arrangements, produced essentially the same slip lengths. However, in the laminar regime the surface texture has a stronger effect on the value of the slip length. Textures of posts in staggered arrangements produced slip lengths smaller than collocated arrangements. This is likely due to the blockage effect of the arrangement, as also seen in randomised surface textures (Seo *et al.*, 2018). The staggered arrangement of posts also resulted in significantly larger texture-coherent deformation of the gas pockets due to the larger stagnation pressures they produce. It was also shown that the results from laminar simulations can predict the slip lengths and the texture-coherent gas pocket deformations of fully turbulent flows for texture sizes $L^+ \lesssim 20$.

In some previous numerical studies, superhydrophobic surfaces have been modelled through the mean effect of the surface, i.e., the slip lengths they produce (Min & Kim, 2004; Busse & Sandham, 2012; Seo & Mani, 2016). While this assumption has been shown to be able to predict the drag in the small-texture limit, $L^+ \lesssim 10$, the results of Seo & Mani (2016) showed that for $L^+ \gtrsim 10$ the velocity and shear at the surface appear to lose correlation, the overlying flow appears to no longer perceive the surface as producing a homogeneous slip effect. In this thesis, however, it was shown that this observed loss of correlation is a consequence of contamination by the texture-induced flow, not a direct effect of the texture size becoming too large. Modulation of the texture-coherent flow with the background turbulence scatters the signal of the former across the entire wavenumber spectrum. The use of a modified form of the triple decomposition (Abderrahaman-Elena & García-Mayoral, 2016) was adapted for application to superhydrophobic surfaces to filter out the texture-induced flow from the flow fields. This decomposition takes into account the modulation of the texture-coherent flow by the background turbulent flow. This allows the texture-induced flow to be filtered from the velocity fields across the full spectrum. Upon filtering the flow fields, the slip length experienced by the background turbulence was shown to be strongly correlated, the overlying flow still experiences the surface as a

homogeneous slip-length boundary condition, at least up to the largest texture size considered, $L^+ \approx 47$. While these results show that the overlying flow perceives the surface as producing a homogeneous slip effect, Seo & Mani (2016) show that ΔU^+ predicted from homogeneous slip models and the measured value from texture-resolved simulations disagree for $L^+ \gtrsim 10$. Therefore, there must be an additional phenomenon present in the texture-resolved simulations.

To discern the separate effects that surface slip and texture have on the overlying turbulence, next, the direct effect of surface slip was investigated through simulations applying the homogeneous slip-length boundary conditions obtained from the textured simulations. It was shown that surfaces modelled by slip-length boundary conditions do not modify the turbulent dynamics in the overlying flow, they remain smooth-wall like. In these cases, the flow can be characterised by two virtual origins, the virtual origin experienced by the mean flow, given by the streamwise slip length, ℓ_x^+, and the virtual origin perceived by the overlying turbulence, ℓ_T^+, with ΔU^+ equal to the difference between these two virtual origins, i.e. $\Delta U^+ \approx \ell_x^+ - \ell_T^+$, an extension of the theory for riblets (Luchini *et al.*, 1991).

Finally, the discrepancy in ΔU^+ between the texture-resolving and slip length simulations was investigated. For the texture-resolved superhydrophobic surfaces it was shown that up to $L^+ \lesssim 20$ these surfaces can be modelled by the homogeneous slip lengths they produce. The overlying turbulence is not significantly modified by the surface texture beyond the effect of surface slip. For larger texture sizes, while the overlying turbulence still experiences the surface as a homogeneous slip-length boundary condition, there appears to be a non-linear interaction between the texture-coherent flow and overlying turbulence, modifying the dynamics of the latter. The Reynolds stress, $\overline{u'v'}^+$, profiles of the background turbulence show a modified shape compared to the homogeneous slip-length profiles. It is shown that this increase in Reynolds stress is the cause for the discrepancy in ΔU^+ between textured and slip length simulations. This increase in Reynolds stress does not occur at the surface but over a range $5 \lesssim y^+ \lesssim 25$, indicating an unfavourable modification to the turbulent dynamics. The rms fluctuations of the velocities show a decrease in streamwise fluctuations and an increase in spanwise and wall-normal fluctuations close to the surface, qualitatively consistent with turbulent flows over rough surfaces (Antonia & Krogstad, 2001; Orlandi & Leonardi, 2006). Premultiplied energy spectra also show a modification in the lengthscale distribution of the turbulent energy, with a reduction in the streamwise coherence for scales of order 1000 wall units, suggesting an alteration to the near-wall turbulent cycle.

7.2 Outlook

This thesis suggests that it is the interaction of the texture-coherent flow with the overlying turbulence that causes the reduction in measured ΔU^+ compared to that predicted using homogeneous slip lengths. With a final aim of modelling the effect of the surface without needing to conduct the full texture-resolved simulations, the next natural question is then whether this effect can be modelled in simulations without needing to fully resolve the texture. This would then allow the drag produced by textured simulations to be estimated beyond the small texture size limit, that is $L^+ \lesssim 25$. This interaction could, perhaps, be thought of as an additional advective-like term in the governing equations resulting from the cross terms of the texture-coherent and background-turbulence. If this texture coherent flow can be predicted *a priori*, i.e. through laminar simulations (Abderrahaman-Elena *et al.*, 2019), this effect could be modelled as an additional forcing term. The ability of such a model to predict the texture-resolved drag would be a natural extension to the present work.

It is hypothesised in this work that it is the intensity, and lengthscales, of the texture-coherent flow that most strongly influences the modifications to the turbulent dynamics. However, only one surface texture was considered in the DNSs. Further analysis is needed to assess how strongly the surface texture affects the overlying flow. For example, the work of Seo *et al.* (2018), who investigated randomised textures, could be expanded upon. The similarities between the turbulent dynamics over superhydrophobic surfaces and roughness is also interesting. While superhydrophobic surfaces typically allow larger surface slip and also impose impermeability at the surface, the net effect on the overlying turbulent flow has many parallels with rough surfaces. It would be interesting to further analyse the similarities, and differences, between turbulent flows over superhydrophobic surfaces and roughness.

Finally, for superhydrophobic surfaces to be used in drag reducing applications, the gas pockets need to remain entrapped. While the dynamics of the liquid-gas interface have started to be investigated in more detail (Seo *et al.*, 2018; García Cartagena *et al.*, 2018), the finer details of why the gas pockets are lost from the surface still remains one of the least well understood aspects of flows over superhydrophobic surfaces. Further work is needed to address the questions of why the gas pockets are lost from the surface, and to what texture size stable gas pockets can remain entrapped on the surface.

Bibliography

Abderrahaman-Elena, N., Fairhall, C. T. & García-Mayoral, R. 2019 Modulation of near-wall turbulence in the transitionally rough regime. *J. Fluid. Mech.* **865**, 1042–1071.

Abderrahaman-Elena, N. & García-Mayoral, R. 2016 Geometry-induced fluctuations in the transitionally rough regime. *J. Phys. Conf. Ser.* **708**, 012009.

Aljallis, E., Sarshar, M. A., Datla, R., Sikka, V., Jones, A. & Choi, C. H. 2013 Experimental study of skin friction drag reduction on superhydrophobic flat plates in high Reynolds number boundary layer flow. *Phys. Fluids* **25**, 025103.

Antonia, R. A. & Krogstad, P.-A. 2001 Turbulence structure in boundary layers over different types of surface roughness. *Fluid Dyn. Res.* **28**, 139–157.

Balasubramanian, A. K., Miller, A. C. & Rediniotis, O. K. 2004 Microstructured hydrophobic skin for hydrodynamic drag reduction. *AIAA Journal* **42**, 411–414.

Bechert, D. W. & Bartenwerfer, M. 1989 The viscous flow on surfaces with longitudinal ribs. *J. Fluid Mech.* **206**, 105–129.

Bechert, D. W., Bruse, M., Hage, W., van der Hoeven, J. G. T. & Hoppe, G. 1997 Experiments on drag-reducing surfaces and their optimization with an adjustable geometry. *J. Fluid Mech.* **338**, 59–87.

Bidkar, R. A., Leblanc, L., Kulkarni, A. J., Bahadur, V., Ceccio, S. L. & Perlin, M. 2014 Skin-friction drag reduction in the turbulent regime using random-textured hydrophobic surfaces. *Phys. Fluids* **26**, 085108.

Blackwelder, R. F. & Eckelmann, H. 1979 Streamwise vortices associated with the bursting phenomenon. *J. Fluid Mech.* **94**, 577–594.

Busse, A. & Sandham, N. D. 2012 Influence of an anisotropic slip-length boundary condition on turbulent channel flow. *Phys. Fluids* **24**, 055111.

Busse, A., Sandham, N. D., McHale, G. & Newton, M. I. 2013 Change in drag, apparent slip and optimum air layer thickness for laminar flow over an idealised superhydrophobic surface. *J. Fluid Mech.* **727**, 488–508.

Canuto, C., Hussaini, M. Y., Quarteroni, A. & Zang, T. A. 2006 *Spectral methods.*, 1st edn. Springer-Verlag Berlin Heidelberg.

Choi, C. H. & Kim, C. J. 2006 Large slip of aqueous liquid flow over a nanoengineered superhydrophobic surface. *Phys. Rev. Lett.* **96**, 066001.

Choi, C. H., Ulmanella, U., Kim, J., Ho, C. M. & Kim, C. J. 2006 Effective slip and friction reduction in nanograted superhydrophobic microchannels. *Phys. Fluids* **18**, 087105.

Choi, C. H., Westin, K. J. A. & Breuer, K. S. 2003 Apparent slip flows in hydrophilic and hydrophobic microchannels. *Phys. Fluids* **15**, 2897.

Choi, H., Moin, P. & Kim, J. 1994 Active turbulence control for drag reduction in wall-bounded flows. *J. Fluid Mech.* **262**, 75–110.

Churaev, N. V., Sobolev, V. D. & Somov, A. N. 1984 Slippage of liquids over lyophobic solid surfaces. *J. Colloid Interface Sci.* **97**, 574–581.

Clauser, F. H. 1956 The turbulent boundary layer. *Adv. in App. Mech.* **4**, 1–51.

Cooley, J. W. & Tukey, J. W. 1965 An algorithm for the machine calculation of complex Fourier series. *Math. Comput.* **19**, 297–301.

Cottin-Bizonne, C., Cross, B., Steinberger, A. & Charlaix, E. 2005 Boundary slip on smooth hydrophobic surfaces: intrinsic effects and possible artifacts. *Phys. Rev. Lett.* **94**, 056102.

Daniello, R. J., Waterhouse, N. E. & Rothstein, J. P. 2009 Drag reduction in turbulent flows over superhydrophobic surfaces. *Phys. Fluids* **21**, 085103.

Davies, J., Maynes, D., Webb, B. W. & Woolford, B. 2006 Laminar flow in a microchannel with superhydrophobic walls exhibiting transverse ribs. *Phys. Fluids* **18**, 087110.

Davis, A. M. J. & Lauga, E. 2009 Geometric transition in friction for flow over a bubble mattress. *Phys. Fluids* **21**, 011701.

Du, P., Wen, J., Luo, Z., Zhang, Z., Song, D. & Hu, H. 2017 Maintenance of air layer and drag reduction on superhydrophobic surface. *Ocean Engineering* **130**, 328335.

European Environment Agency 2017 Greenhouse gas emissions from transport. https://www.eea.europa.eu/data-and-maps/indicators/transport-emissions-of-greenhouse-gases/transport-emissions-of-greenhouse-gases-10.

Fairhall, C. T., Abderrahaman-Elena, N. & García-Mayoral, R. 2019 The effect of slip and surface texture on turbulence over superhydrophobic surfaces. *J. Fluid. Mech.* **861**, 88–118.

Fairhall, C. T. & García-Mayoral, R. 2015 Influence of surface texture on drag reduction of superhydrophobic surfaces. In *European Drag Reduction and Flow Control Meeting 2015*, pp. 75–76.

Fairhall, C. T. & García-Mayoral, R. 2017*a* Inhomogeneity of the slip-length for simulations over superhydrophobic surfaces. In *European Drag Reduction and Flow Control Meeting 2017*.

Fairhall, C. T. & García-Mayoral, R. 2017*b* The application of slip length models to larger textures in turbulent flows over superhydrophobic surfaces. In *APS Division of Fluid Dynamics (Fall) 2017*.

Fairhall, C. T. & García-Mayoral, R. 2018 Spectral analysis of the slip-length model for turbulence over textured superhydrophobic surfaces. *Flow Turbul. Combust.* **100**, 961–978.

Ferziger, J. H. & Peric, M. 2002 *Computational methods for fluid dynamics.*, 3rd edn. Springer-Verlag Berlin Heidelberg.

Flack, K. A., Schultz, M. P. & Connelly, J. S. 2007 Examination of a critical roughness height for outer layer similarity. *Phys. Fluids* **19**, 095104.

Fukagata, K., Kasagi, N. & Koumoutsakos, P. 2006 A theoretical prediction of friction drag reduction in turbulent flow by superhydrophobic surfaces. *Phys. Fluids* **18**, 051703.

García Cartagena, E. J., Arenas, I., Bernardini, M. & Leonardi, S. 2018 Dependence of the drag over super hydrophobic and liquid infused surfaces on the textured surface and Weber number. *Flow Turbul. Combust.* **100**, 945–960.

García-Mayoral, R. 2011 The interaction of riblets with wall-bounded turbulence. PhD thesis, Universidad Politecnica de Madrid.

García-Mayoral, R., Gómez-de-Segura, G. & Fairhall, C. T. 2018 The control of near-wall turbulence through surface texturing. *Fluid Dyn. Res.* **51**, 011410.

García-Mayoral, R. & Jiménez, J. 2011 Hydrodynamic stability and breakdown of the viscous regime over riblets. *J. Fluid Mech.* **678**, 317–347.

Gatti, D. & Quadrio, M. 2016 Reynolds-number dependence of turbulent skin-friction drag reduction induced by spanwise forcing. *J. Fluid Mech.* **802**, 553–582.

Gogte, S., Vorobieff, P., Truesdell, R., Mammoli, A., van Swol, F., Shah, P. & Brinker, C. J. 2005 Effective slip on textured superhydrophobic surfaces. *Phys. Fluids* **17**, 051701.

Gómez-de-Segura, G., Fairhall, C. T., MacDonald, M., Chung, D. & García-Mayoral, R. 2018 Manipulation of near-wall turbulence by surface slip and permeability. *J. Phys. Conf. Ser.* **1001**, 012011.

Gose, J. W., Golovin, K., Boban, M., Mabry, J. M., Tuteja, A., Perlin, M. & Ceccio, S. L. 2018 Characterization of superhydrophobic surfaces for drag reduction in turbulent flow. *J. Fluid Mech.* **845**, 560–580.

Govardhan, R. N., Srinivas, G. S., Asthana, A. & Bobji, M. S. 2009 Time dependence of effective slip on textured hydrophobic surfaces. *Phys. Fluids* **21**, 052001.

Hahn, S., Je, J. & Choi, H. 2002 Direct numerical simulation of turbulent channel flow with permeable walls. *J. Fluid Mech.* **450**, 259–285.

Hamilton, J. M., Kim, J. & Waleffe, F. 1995 Regeneration mechanisms of near-wall turbulence structures. *J. Fluid Mech.* **287**, 317–348.

Henoch, C., Krupenkin, T. N., Kolodner, P., Taylor, J. A., Hodes, M. S., Lyons, A., Peguero, C. & Breuer, K. 2006 Turbulent drag reduction using superhydrophobic surfaces. *3rd AIAA Flow Control Conf.* pp. 840–844.

Hokmabad, B. V. & Ghaemi, S. 2016 Turbulent flow over wetted and non-wetted superhydrophobic counterparts with random structure. *Phys. Fluids* **28**, 015112.

Hutchins, N. & Marusic, I. 2007 Large-scale influences in near-wall turbulence. *Philos. Trans. Royal Soc. A* **365**, 647–664.

Hyväluoma, J. & Harting, J. 2008 Slip flow over structured surfaces with entrapped microbubbles. *Phys. Rev. Lett.* **100**, 246001.

Jelly, T. O., Jung, S. Y. & Zaki, T. A. 2014 Turbulence and skin friction modification in channel flow with streamwise-aligned superhydrophobic surface texture. *Phys. Fluids* **26**, 095102.

Jeong, J., Hussain, F., Schoppa, W. & Kim, J. 1997 Coherent structures near the wall in a turbulent channel flow. *J. Fluid Mech.* **332**, 185–214.

Jiménez, J. 1994 On the structure and control of near wall turbulence. *Phys. Fluids* **6**, 944–953.

Jiménez, J. & Moin, P. 1991 The minimal flow unit in near-wall turbulence. *J. Fluid Mech.* **225**, 213–240.

Jiménez, J. & Pinelli, A. 1999 The autonomous cycle of near-wall turbulence. *J. Fluid Mech.* **389**, 335–359.

Jung, T., Choi, H. & Kim, J. 2016 Effects of the air layer of an idealized superhydrophobic surface on the slip length and skin-friction drag. *J. Fluid Mech.* **790**, R1.

Jung, W. J., Mangiavacchi, N. & Akhavan, R. 1992 Suppression of turbulence in wall-bounded flows by high-frequency spanwise oscillations. *Phys. Fluids* **4**, 1605–1607.

Khosh Aghdam, S. & Ricco, P. 2016 Laminar and turbulent flows over hydrophobic surfaces with shear-dependent slip length. *Phys. Fluids* **28**, 035109.

Kim, H. T., Kline, S. J. & Reynolds, W. C. 1971 The production of turbulence near a smooth wall in a turbulent boundary layer. *J. Fluid Mech.* **50**, 133–160.

Kim, J. & Moin, P. 1985 Application of a fractional-step method to incompressible Navier-Stokes equations. *J. Comp. Phys.* **59**, 308–323.

Kim, J., Moin, P. & Moser, R. 1987 Turbulence statistics in fully developed channel flow at low Reynolds number. *J. Fluid Mech.* **177**, 133–166.

Kline, S. J., Reynolds, W. C., Schraub, F. A. & Runstadler, P. W. 1967 The structure of turbulent boundary layers. *J. Fluid Mech.* **30**, 741–773.

Kreplin, H. P. & Eckelmann, H. 1979 Propagation of perturbations in the viscous sublayer and adjacent wall region. *J. Fluid Mech.* **95**, 305–322.

Krogstad, P.-A. & Antonia, R. A. 1994 Structure of turbulent boundary layers on smooth and rough walls. *J. Fluid Mech.* **277**, 1–21.

Lafuma, A. & Quere, D. 2011 Slippery pre-suffused surfaces. *Europhys. Lett.* **96**, 56001.

Lauga, E. & Stone, H. A. 2003 Effective slip in pressure-driven Stokes flow. *J. Fluid Mech.* **489**, 55–77.

Le, H. & Moin, P. 1991 An improvement of fractional step methods for the incompressible Navier-Stokes equations. *J. Comp. Phys.* **92**, 369–379.

Lee, C., Choi, C. H. & Kim, C. J. 2008 Structured surfaces for a giant liquid slip. *Phys. Rev. Lett.* **101**, 064501.

Lee, C. & Kim, C. J. 2011 Underwater restoration and retention of gases on superhydrophobic surfaces for drag reduction. *Phys. Rev. Lett.* **106**, 014502.

Lee, J., Jelly, T. O. & Zaki, T. A. 2015 Effect of Reynolds number on turbulent drag reduction by superhydrophobic surface textures. *Flow Turbul. Combust.* **95**, 277–300.

Lele, S. K. 1992 Compact finite difference schemes with spectral-like resolution. *J. Comp. Phys.* **103**, 16–42.

Ling, H., Srinivasan, S., Golovin, K., McKinley, G. H., Tuteja, A. & Katz, J. 2016 High-resolution velocity measurements in the inner part of turbulent boundary layers over super-hydrophobic surfaces. *J. Fluid Mech.* **801**, 670–703.

Luchini, P. 1996 Reducing the turbulent skin friction. In *Computational Methods in Applied Sciences – Proc. 3rd ECCOMAS CFD Conference*, pp. 466–470.

Luchini, P. 2015 The relevance of longitudinal and transverse protrusion heights for drag reduction by a superhydrophobic surface. In *European Drag Reduction and Flow Control Meeting 2015*, pp. 81–82.

Luchini, P., Manzo, F. & Pozzi, A. 1991 Resistance of a grooved surface to parallel flow and cross-flow. *J. Fluid Mech.* **228**, 87–109.

MacDonald, M., Ooi, A., García-Mayoral, R., Hutchins, N. & Chung, D. 2018 Direct numerical simulation of high aspect ratio spanwise-aligned bars. *J. Fluid Mech.* **843**, 126–155.

Mahadevan, L. & Pomeau, Y. 1999 Rolling droplets. *Phys. Fluids* **11** (9), 2449–2453.

Martell, M. B., Perot, J. B. & Rothstein, J. P. 2009 Direct numerical simulations of turbulent flows over superhydrophobic surfaces. *J. Fluid Mech.* **620**, 31–41.

Martell, M. B., Perot, J. B. & Rothstein, J. P. 2010 An analysis of superhydrophobic turbulent drag reduction mechanisms using direct numerical simulation. *Phys. Fluids* **22**, 065102.

Maynes, D., Jeffs, K., Woolford, B. & Webb, B. W. 2007 Laminar flow in a microchannel with hydrophobic surface patterned microribs oriented parallel to the flow direction. *Phys. Fluids* **19**, 093603.

Min, T. & Kim, J. 2004 Effects of hydrophobic surface on skin-friction drag. *Phys. Fluids* **16**, L55–L58.

Min, T. & Kim, J. 2005 Effects of hydrophobic surface on stability and transition. *Phys. Fluids* **17**, 108106.

Moser, R. D., Kim, J. & Mansour, N. N. 1999 Direct numerical simulation of turbulent channel flow up to $\mathrm{Re}_\tau = 590$. *Phys. Fluids* **11** (4), 943–945.

Navier, C. L. M. H. 1823 Memoire sur les lois du mouvement des fluide. *Mem. Acad. R. Sci. Inst. France* **6**, 389–440.

Nordström, J., Mattsson, K. & Swanson, C. 2007 Boundary conditions for a divergence free velocity pressure formulation of the Navier Stokes equations. *J. Comp. Phys.* **225**, 874–890.

Orlandi, P. & Leonardi, S. 2006 DNS of turbulent channel flows with two- and three-dimensional roughness. *J. Turbul.* **7**, N73.

Ou, J., Perot, B. & Rothstein, J. P. 2004 Laminar drag reduction in microchannels using ultrahydrophobic surfaces. *Phys. Fluids* **16**, 4635–4643.

Ou, J. & Rothstein, J. P. 2005 Direct velocity measurements of the flow past drag-reducing ultrahydrophobic surfaces. *Phys. Fluids* **17**, 103606.

Park, H., Park, H. & kim, J. 2013 A numerical study of the effects of superhydrophobic surface on skin-friction drag in turbulent channel flow. *Phys. Fluids* **25**, 110815.

Park, H., Sun, G. & Kim, C. J. 2014 Superhydrophobic turbulent drag reduction as a function of surface grating parameters. *J. Fluid Mech.* **747**, 722–734.

Perot, J. B. 1993 An analysis of the fractional step method. *J. Comp. Phys.* **108**, 51–584.

Philip, J. R. 1972 Flows satisfying mixed no-slip and no-shear conditions. *Z. Angew. Math. Phys.* **23**, 353–372.

Quadrio, M., Frohnapfel, B. & Hasegawa, Y. 2016 Does the choice of the forcing term affect flow statistics in DNS of turbulent channel flow? *Euro. J. Mech. B/Fluids.* **55, Part 2**, 286–293.

Rastegari, A. & Akhavan, R. 2015 On the mechanism of turbulent drag reduction with super-hydrophobic surfaces. *J. Fluid Mech.* **773**, R4.

Reynolds, W. C. & Hussain, A. K. M. F. 1972 The mechanics of an organized wave in turbulent shear flow. Part 3. Theoretical models and comparisons with experiments. *J. Fluid Mech.* **54**, 263–288.

Rosenberg, B. J., Buren, T. V., Fu, M. K. & Smits, A. J. 2016 Turbulent drag reduction over air- and liquid- impregnated surfaces. *Phys. Fluids* **28**, 015103.

Rothstein, J. P. 2010 Slip on superhydrophobic surfaces. *Annu. Rev. Fluid Mech.* **42**, 89–109.

Sbragaglia, M. & Prosperetti, A. 2007 Effective velocity boundary condition at a mixed slip surface. *J. Fluid Mech.* **578**, 435–451.

Schönecker, C., Baier, T. & Hardt, S. 2014 Influence of the enclosed fluid on the flow over a microstructured surface in the Cassie state. *J. Fluid Mech.* **740**, 168–195.

Seo, J., García-Mayoral, R. & Mani, A. 2015 Pressure fluctuations and interfacial robustness in turbulent flows over superhydrophobic surfaces. *J. Fluid Mech.* **783**, 448–473.

Seo, J., García-Mayoral, R. & Mani, A. 2018 Turbulent flows over superhydrophobic surfaces: flow-induced capillary waves, and robustness of air-water interfaces. *J. Fluid Mech.* **835**, 45–85.

Seo, J. & Mani, A. 2016 On the scaling of the slip velocity in turbulent flows over superhydrophobic surfaces. *Phys. Fluids* **28**, 025110.

Seo, J. & Mani, A. 2018 Effect of texture randomization on the slip and interfacial robustness in turbulent flows over superhydrophobic surfaces. *Phys. Rev. Fluids* **3**, 044601.

Simens, RM. 2008 The study and control of wall bounded flows. PhD thesis, Universidad Politecnica de Madrid.

Smith, C. R. & Metzler, P. 1983 The characteristics of low-speed streaks in the near-wall region of a turbulent boundary layer. *J. Fluid Mech.* **129**, 27–54.

Spalart, P. R. 1988 Direct simulation of a turbulent boundary layer up to $\mathrm{Re}_\theta = 1410$. *J. Fluid Mech.* **187**, 61–98.

Spalart, P. R. & McLean, J. D. 2011 Drag reduction: enticing turbulence, and then an industry. *Philos. Trans. Royal Soc. A* **369**, 1556–1569.

Srinivasan, S., Kleingartner, J. A., Gilbert, J. B., Cohen, R. E., Milne, A. J. B. & Mckinley, G. H. 2015 Sustainable drag reduction in turbulent Taylor-Couette flows by depositing sprayable superhydrophobic surfaces. *Phys. Rev. Lett.* **114**, 014501.

Steinberger, A., Cottin-Bizonne, C., Kleimann, P. & Charlaix, E. 2007 High friction on a bubble mattress. *Nat. Mater.* **6**, 665–668.

Teo, C. J. & Khoo, B. C. 2010 Flow past superhydrophobic surfaces containing longitudinal grooves: effects of interface curvature. *Microfluid. Nanofluid.* **9**, 499–511.

Thomas, L. H. 1949 Elliptic problems in linear difference equations over a network. *Watson Sci. Comput. Lab. Rept., Columbia University, New York* **1**.

Tian, H., Zhang, J., Wang, E., Yao, Z. & Jiang, N. 2015 Experimental investigation on drag reduction in turbulent boundary layer over superhydrophobic surface by TRPIV. *Theor. Appl. Mech. Lett.* **5**, 45–49.

Truesdell, R., Mammoli, A., Vorobieff, P., van Swol, F. & Brinker, C. J. 2006 Drag reduction on a patterned superhydrophobic surface. *Phys. Rev. Lett.* **97**, 044504.

Türk, S., Daschiel, G., Stroh, A., Hasegawa, Y. & Frohnapfel, B. 2014 Turbulent flow over superhydrophobic surfaces with streamwise grooves. *J. Fluid Mech.* **747**, 186–217.

Virk, P. S. 1975 Drag reduction fundamentals. *AIChE Journal* **21** (4), 625–656.

Walsh, M. J. 1983 Riblets as a viscous drag reduction technique. *AIAA journal* **21**, 485–486.

Wang, L. P., Teo, C. J. & Khoo, B. C. 2014 Effects of interface deformation on flow through microtubes containing superhydrophobic surfaces with longitudinal ribs and grooves. *Microfluid. Nanofluid.* **16**, 225–236.

Watanabe, K., Yanuar & Udagawa, H. 1999 Drag reduction of Newtonian fluid in a circular pipe with a highly water-repellent wall. *J. Fluid Mech.* **381**, 225–238.

Wexler, J. S., Grosskopf, A., Chow, M., Fan, Y., Jacobi, I. & Stone, H. A. 2015*a* Robust liquid-infused surfaces through patterned wettability. *Soft Matter* **11**, 5023–5029.

Wexler, J. S., Jacobi, I. & Stone, H. A. 2015*b* Shear-driven failure of liquid-infused surfaces. *Phys. Rev. Let.* **114**, 168301.

Wong, T.-S., Kang, S. H., Tang, S. K. Y., Smythe, E. J., Hatton, B. D., Grinthal, A. & Aizenberg, J. 2011 Bioinspired self-repairing slippery surfaces with pressure-stable omniphobicity. *Nature* **477**, 443–447.

Woolford, B., Prince, J., Maynes, D. & Webb, B. W. 2009 Particle image velocimetry characterization of turbulent channel flow with rib patterned superhydrophobic walls. *Phys. Fluids* **21**, 085106.

Ybert, C., Barentin, C. & Cottin-Bizonne, C. 2007 Achieving large slip with superhydrophobic surfaces: scaling laws for generic geometries. *Phys. Fluids* **19**, 123601.

Zhang, J., Tian, H., Yao, Z., Hao, P. & Jiang, N. 2015 Mechanisms of drag reduction of superhydrophobic surfaces in a turbulent boundary layer flow. *Exp. Fluids* **56**, 179.

Zhao, J. P., Du, X. D. & Shi, X. H. 2007 Experimental research on friction-reduction with super-hydrophobic surfaces. *J. Mar. Sci. Appl.* **6**, 58–61.